UNIVERSITA' CAMPUS BIO-MEDICO DI ROMA

School of Engineering
PhD Course in Bioengineering and Bioscience
XXX cycle – A.A. 2014-2015

**Feasibility of temperature monitoring based on
radiological imaging during thermal ablation
procedures on biological tissues**

Supervisor   *PhD Candidate*
Prof. Sergio Silvestri   Dott. Francesco Giurazza

Co-tutors
Prof. Emiliano Schena
Prof. Bruno Beomonte Zobel

A Giulia e Barbara,
la mia mandria

Table of Contents

List of abbreviations

ARFI: Acoustic Radiation Force Imaging

AT: Acquisition Time

AVGL: Average Grey Level

CrA: Cryoablation

CSI: Chemical Shift Imaging

CT: Computed Tomography

D: Diffusion

EMF: ElectroMotive Force

EPI: Echo-Planar Imaging

EPSI: Echo Planar Spectroscopic Imaging

FBG: Fiber Bragg grating

GLCM: Gray-Level Co-occurrence Matrix

GRE: Gradient-Recalled Echo

HIFU: High intensity focused ultrasound

IR: Interventional Radiology

LSPESI: Line Scan Echo Planar Spectroscopic Imaging

LOA: Limits of Agrrement

LTA: Laser-Therapy Ablation

MOD: Mean of Difference

MR: Magnetic Resonance

MRSI: Magnetic Resonance Spectroscopic Imaging

MWA: Microwaves Ablation

PMMA: Polymethylmethacrylate

PRF: Proton Resonance Frequency

RFA: Radiofrequency Ablation

ROE: Region Of Excitation

ROI: Region Of Interest

SNR: Signal to Noise Ratio

SOS: Speed Of Sound

T: Tesla

TE: Echo Time

TI: Inversion Time

TR: Relaxation Time

US: Ultrasound

Abstract

Minimally invasive ablation techniques are nowadays part of the clinical practice in the field of oncological treatments. Thanks to the technological improvements, thermal energy delivered through a needle allows to destroy malignancies without requiring a traditional open surgical approach.

However, to safely perform these procedures it is crucial to monitor the temperature distribution into the treated tissues, in order to reach the target temperature able to destroy malignant cells and to preserve healthy surrounding structures.

Real time tissue temperature monitoring can be obtained with invasive techniques (i.e. thermocouples and fiber optic sensors directly inserted close to the ablation area) and non-invasive techniques (i.e. imaging scans based on radiological techniques as Computed Tomography, Magnetic Resonance and Ultrasound).

In this research project, first of all it has been investigated the role of Fiber Bragg grating sensors for temperature monitoring in *ex vivo* and *in vivo* biological tissues and then it has been assessed the feasibility of imaging based thermometry on *ex vivo* biological tissues (i.e. swine pancreas and livers) during ablation procedures performed with different forms of energy sources routinary applied in the clinical practice (i.e. Laser, Radiofrequency, Microwaves). The variations of Hounsfield Units on Computed Tomography, signal-to-noise ratios on Magnetic Resonance and shear wave velocities on Ultrasound have prooven to be reliable with tissue temperature changes occurring during thermal ablations (>60°C); mathematical equations to obtain tissue

temperature values based on radiological imaging parameters have been so developed.

According to the results provided, specially from experimental sessions on Computed Tomography and Magnetic Resonance, real time imaging based thermometry seems to be a safe and feasible biomedical methodology which could significantly improve the actual ablation settings and furthermore could lead the operators to treat a wider spectrum of malignant lesions sparing healthy tissues. Further studies on Ultrasound are necessary to make this technique applicable in clinical settings.

Chapter I

Thermal-ablation treatments in interventional radiology for oncological pathologies: ablation techniques and fields of application

- I.1 Introduction and rationale of minimally invasive ablation treatments

Interventional radiology (IR) was born in late 60s when Charles Dotter percutaneously dilated a stenosis of the superficial femoral artery causing painful leg ischemia [1]. Oncological IR started in the 1970s with infusion chemotherapy to various tumors by pioneers such as Sidney Wallace.

Tumor ablation began with ethanol injection, followed by thermal ablation that entered clinical practice for the treatment of liver tumors in 1997. Thermal ablation expanded to other organs with the first radiofrequency ablation of lung tumors reported in 2000, and a series of hundreds of patients with lung metastases treated with thermal ablation are now available [2].

Oncological IR has evolved rapidly in the last decades to become one of the fastest growing, minimally invasive, and the most exciting pillars of cancer treatment.

Through the years, interventional radiologists alone or partnering with industry, improved existing and developed new, alternative, technologies to radiofrequency ablation (RFA), such as microwave ablation (MWA) and

cryoablation (CrA) or laser-therapy ablation (LTA) [2].

Many of the modern tools and treatments developed and pioneered by interventional radiologists were spread within, and accepted by the oncology practice as valuable treatment options in various cancer diseases.

Oncological IR is different from surgery: it is a disruptive force in medicine because of oncological IR ability to reliably achieve the same results as others using entirely different, less invasive approaches [3]. From a marketing perspective, disruptive innovation usually saves time or money, is as, or more effective, more encompassing, and more productive.

Disruptive innovation initially satisfies the least demanding customers and then more demanding customers drop established, higher performance option based on cost, convenience of the disruptive innovation (Fig. 1.1). As a disruptive innovation, oncological IR offers exceptional weapons against cancer, because oncology IR is able to access the tumor in many major organs with low invasiveness. This low invasiveness allows treating patients where surgery is irrelevant.
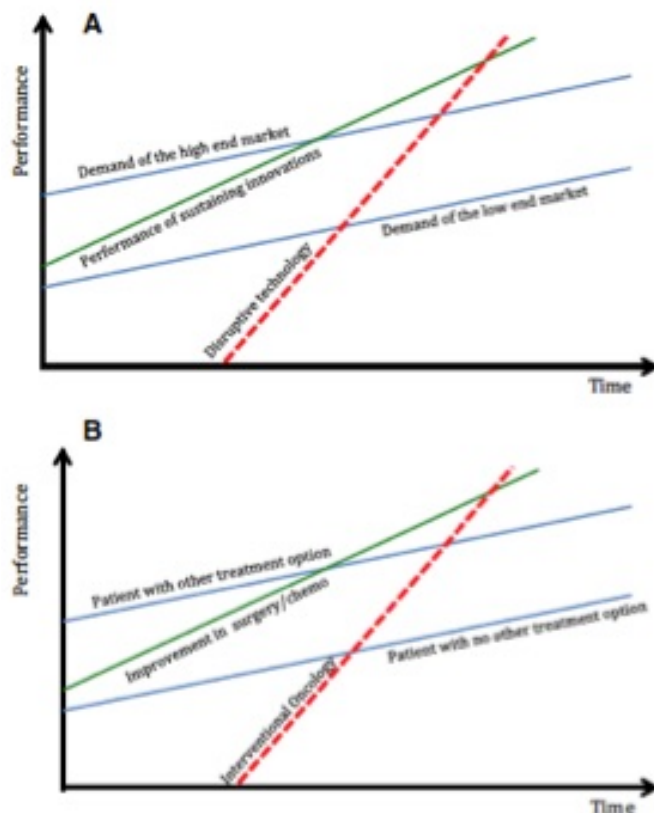
Fig. 1.1 Schematic representation of disruptive technology in relation to sustaining innovation and market demand according to Clayon Christensen's Theory (A) and schematic representation of oncological IR in relation to improvement in other oncologic specialities and patient treatment options (B) [2].

RFA, MWA, CrA and LTA are minimally invasive percutaneous techniques producing hyperthermal ablations and employed for focal treatment of malignancies. They require positioning of a needle-like applicator through the skin up to the target (tumoral lesions located into the liver, pancreas, lung, bone, kidney etc.); the trajectory of the needle, as well as the target, are controlled with radiological imaging as Computed Tomography (CT), Magnetic Resonance (MR) and Ultrasound (US). The tip

of the needle releases energy that interacting with the tissue is converted into heat. The final effect is a temperature increase or decrease that causes tissue thermal damage.

The aim of all the ablation procedures is twofold: to destroy the target lesion and to preserve healthy surrounding tissues; in order to achieve this goal, monitoring temperature distribution may be beneficial for improving the treatment outcomes, because temperature can be used as a clear end point to completly remove the tumor minimizing the damage of surrouning anatomical structures. This solution allows percutaneous ablative therapies to gain a substantial advantage over conventional surgical resection: the potential to remove or destroy only a minimal amount of normal tissue; for example, in primary liver tumors, where functional hepatic reserve is a primary predictive factor for long-term patient survival outcome, ablation therapies can minimize iatrogenic damage to surrounding cirrothic parenchima [4].

- I.2 Thermal ablation therapies

Thermal ablation techniques attempt to destroy tumor tissue by increasing or decreasing temperatures in order to induce irreversible cellular injury. These strategies can be broadly divided into CrA and hyperthermic ablation, in which heat may be generated by electromagnetic (ie, RFA, MWA, LTA) energy. Complete and adequate destruction by thermal ablation requires that the entire tumor and an ablative margin be subjected to cytotoxic temperatures.

The ability to heat or cool large volumes of tissue in

different environments is dependent on several factors as follows: "the extent of coagulation necrosis induced in a given lesion is equal to the energy deposited, modified by local tissue interactions, minus the heat lost before inducing thermal damage" [5].

On the basis of this relationship, several strategies have been developed to increase the amount of coagulation necrosis (ultimate histological result of thermal ablation procedures), including increasing energy deposition, modulating tissue characteristics, and modifying tissue blood flow. Although this is a useful framework, the absolute temperature achieved at any point within a tumor does not mean definitively that ablation has occurred, and heterogeneity of heating throughout the target volume is more often the rule than the exception.

Thermal ablation of focal tumors uses high-temperature tissue heating (>50°C) surrounding applicators placed at the center of a tumor (Fig. 1.2). Immediate cellular damage centers on protein coagulation of cytosolic and mitochondrial enzymes and nucleic acid–histone protein complexes [6]. This damage triggers cellular death over the course of several days. The term "coagulation necrosis" is used to describe this thermal damage.

The threshold target temperature of 50°C should be used only as a general guideline. Indeed, the exact temperature at which cell death occurs is multifactorial and tissue specific. On the basis of results of a study [7] that demonstrates that tissue coagulation can be induced by focal tissue heating to approximately 50°C for less than 5 minutes, this has become the standard surrogate endpoint for thermal ablation therapies in both experimental studies and current clinical paradigms.
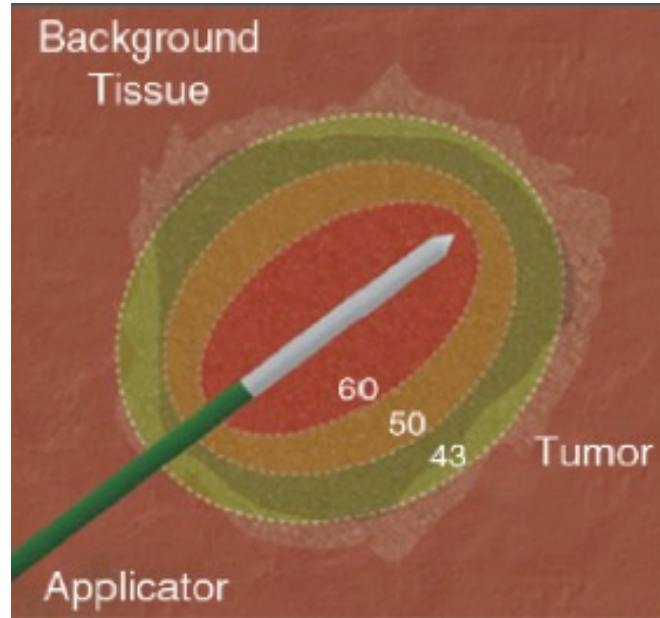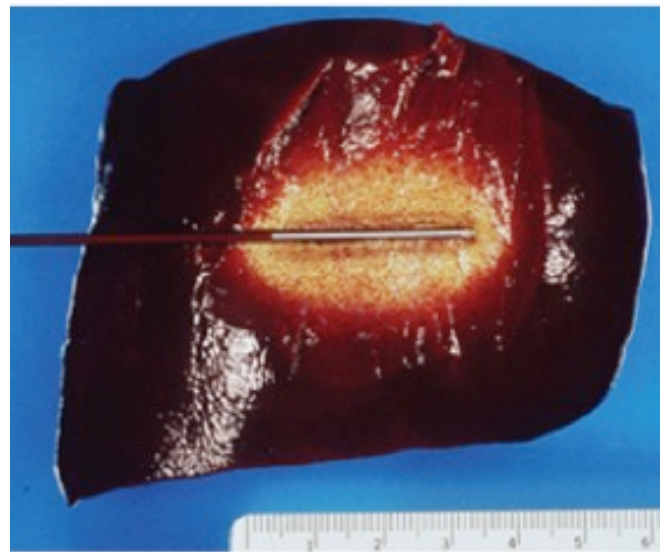
Fig. 1.2 (a) Schematic and (b) gross specimen show focal thermal ablation. A central zone of high temperatures (greater than 60°C, can exceed 100°C) is created in tissue immediately around the electrode, and it is surrounded by more peripheral zones of sublethal tissue heating (43°–50°C) and background liver parenchyma [6].

I.2.1 Radiofrequency ablation

RF energy is the most well-studied and clinically relevant percutaneous ablation source.

During RFA, electrical current from the generator oscillates between electrodes through ion channels present in most biologic tissues.

The RFA setup can be considered as a simple electrical circuit wherein the current loop comprises a generator, cabling, electrodes, and tissue as the resistive element. Tissues are imperfect conductors of electricity (they have electrical impedance), so current flow leads to frictional agitation at the ionic level and heat generation, known as the Joule effect.

Heating occurs most rapidly in areas of high current density: tissues nearest to an electrode are heated most effectively, while more peripheral areas receive heat by thermal conduction [8].

Ablative heating leads to tissue dehydration and water vaporization, which cause dramatic increases in circuit impedance [9]. These rapid and often sudden increases in impedance can be used as a feedback signal in RF generators.

Most RFA systems today operate in a monopolar mode by using two different types of electrodes: interstitial electrodes (hereafter, electrode) and dispersive electrodes on the skin surface (also known as ground pads). The electrode delivers energy to the tumor, creating a volume of high current density and localized heating. The ground pad closes the electrical current path but is designed to disperse energy over a large surface area to reduce the likelihood of thermal injury to the skin.

Internally cooled electrodes use a single needle, in which fluid is circulated inside the electrode's active tip, and temperatures at the electrode-tissue interface are reduced. Lower temperatures inhibit charring, which, in turn, allows increased power deposition. In effect, internal cooling drives RF heating from the electrode-tissue interface deeper into the tissue to create more clinically relevant ablations (approximately 2 cm in diameter in normal liver) [10, 11].

The RFA generator provides three essential functions: power generation, control and user interface. It is important to remember that an RFA system can be approximated as a basic resistor circuit and that current is governed by Ohm's law: $I = V / Z$, where I is the current [A], V is the voltage [V], and Z is the impedance [Ω]. Power, P [W], is defined using the following three relationships: $P = VI = V^2/Z = I^2Z$. P is controlled by V and Z, which includes all possible factors, such as electrode design, target tissue environment, background tissue properties, and ground pad connectivity.

The ground pad used with monopolar electrodes is intended to provide a large dissipative surface for electrical current flow through the skin.

I.2.2 Microwaves ablation

The term microwave describes electromagnetic energy in the 300 MHz to 300 GHz range; however, for practical and regulatory reasons, microwave ablation devices are typically operated at either 915 MHz or 2.45 GHz.

Microwave heating is produced as a result of dielectric hysteresis (rotating dipoles), which differs from the Joule heating mechanism of RFA. When electromagnetic energy

is applied to tissue, some of the energy is used to force molecules with an intrinsic dipole moment (e.g., water) to continuously realign with the applied field. This rotation of molecules represents an increase in kinetic energy and, hence, an elevation in local tissue temperatures.

Microwave energy has demonstrated several advantages for tissue ablation [12]. Microwaves readily penetrate through biologic materials, including those with low electrical conductivity, such as lung, bone, and dehydrated or charred tissue. Consequently, microwave power can be continually applied to produce extremely high (>150°C) temperatures, which improves ablation efficacy by increasing thermal conduction into the surrounding tissue. Microwaves also heat tissue more efficiently than does RF energy, do not require ground pads, and multiple antennas can be operated simultaneously [13].

On the other hand, microwave energy is inherently more difficult to distribute than RF energy. Microwaves must be carried in waveguides, such as coaxial cable, which are typically more cumbersome than the small wires used to feed energy to RF electrodes and are prone to heating when carrying large amounts of power. It is well known that higher microwave powers increase ablation zone size, but excessive power in the antenna shaft can lead to unintended injuries to other tissues, such as the skin [14].

The purpose of the antenna is to couple energy from the feeding cable into the tissue. Antenna designs vary, and trade-offs between antenna efficiency, size, and heating pattern are often required (Fig. 1.3). Antenna properties, such as efficiency and heating pattern, are primarily controlled by the surrounding tissue properties and antenna geometry. Common designs include monopole,

dipole, triaxial, choked, and slotted antennas. Mainly, antennas use a straight needlelike design.

Most of these systems operate at 2.45 GHz and use monopole, dipole, or slotted coaxial antennas to deliver up to 60 W.
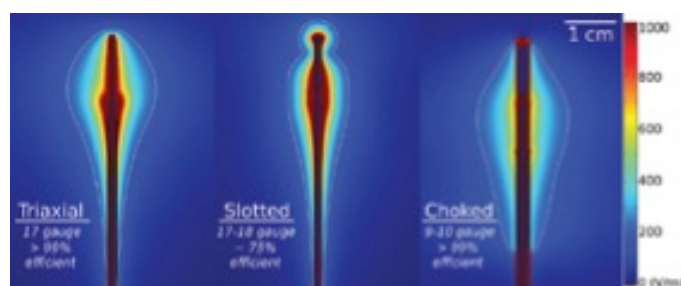
Fig. 1.3 Electric field patterns surrounding three microwave antenna designs with associated antenna size and power application efficiency: triaxial, single slot (Slotted) and choked dipole (Choked). Electrical field [V/m] is color coded for simulations at 2.45 GHz and 50 W input power in normal liver tissue. Images show the balance between antenna size, efficiency and heating pattern [14].

I.2.3 Laser-therapy ablation

Like radiofrequency and microwaves energy, lasers induce electromagnetic heating to elevate tissue temperatures to lethal levels.

Laser sources, including pumped neodymium-doped, yttrium aluminum garnet and semiconductor diodes, emit approximately 600–1000-nm wavelength light energy.

The primary advantage of using laser energy is that it may be coupled through optical fibers, which are inherently MR compatible.

In addition, the lack of metal in the power distribution chain and relatively small diameter of most applicators effectively eliminate image artifacts on CT and MR

images. So, it is more reasonable to perform MR temperature mapping during LTA [15].

Laser light is an efficient and precise energy source for tissue heating. However, because light is scattered and absorbed rapidly by most body tissues, lasers have limited energy penetration and create smaller ablation zones (1–2 cm diameter) than many other devices currently in use. Light does not penetrate through charred or desiccated tissues.

Diffuser tips are used to improve applicator heating profiles, and higher powers can offset the reduced penetration depth by increasing local temperatures, but when higher powers are used, fibers must be cooled to avoid skin burns or probe failure. Cooling increases the diameter of each applicator. Larger ablation volumes are typically realized by using multiple applicators, which can be operated independently and simultaneously [16].

I.2.4 Cryoablation

Cryoablation systems use the Joule-Thomson effect to create unique freeze and thaw cycles. The Joule-Thomson effect describes the change in temperature of a gas resulting from expansion or compression of that gas. Argon is an example of a gas that cools during expansion; helium warms. Gas expansion occurs in a small chamber inside the distal end of the cryoprobe to create the necessary heat sink during freeze cycles and heat source during thaw cycles; ice formation within the extracellular space causes an osmotic gradient, responsible for tissue dehydration. The procedure is performed by means of a cryoprobe and a cryogenic freezing unit: the unit allows a high-pressure gas (e.g., argon) to circulate within the

lumen of the cryoprobe. The low pressure within the lumen causes rapid expansion of gas, which results in a temperature decrease and in the formation of an iceball around the probe tip (Fig. 1.4). CT and MR images are particularly recommended for the monitoring of cryoablation [17].

The size of the ablation zone correlates to probe diameter in these systems; cryoprobes with a smaller diameter typically create smaller zones of complete ablation. For this reason, many users choose to use two or more cryoprobes in proximity to ensure complete coverage of the tumor within the lethal isotherm. Thermal synergy between cryoprobes has been shown to improve efficacy in both numeric and experimental tissue models.

Common clinically treated tumors include focal primary renal tumors and palliative treatment of osseous metastases.
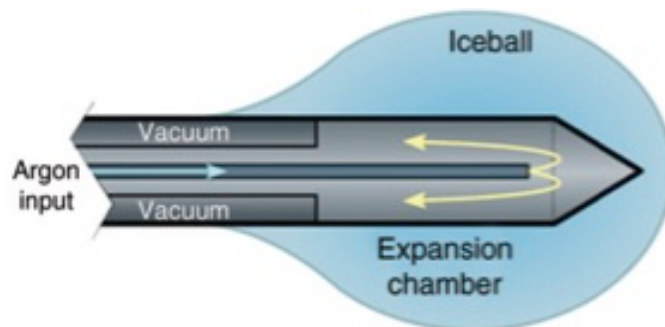
Fig. 1.4 Schematic illustration of a cryoprobe tip with surrounding iceball formation [17].

I.2.5 High intensity focused ultrasound

The principle of action of HIFU is an ultrasound wave produced by an oscillating piezoelectric crystal (frequencies ranging from 0.2 MHz to 3.5 MHz) in the

generator outside the body that is focused on the target region. HIFU transducers deliver ultrasound with intensities (power densities) in the range of 100–10000 $W \cdot cm^{-2}$ to the focal region, with peak compression pressures up to 70 MPa, and peak rarefaction pressures up to 20 MPa (these values depend on the target tissue). The predominant mechanisms involved in the tissue damage are thermal (conversion of mechanical energy into heat) and purely mechanical. Concerning the latter, stable cavitation, inertial cavitation, and micro-streaming are responsible for the oscillation of the size of the bubble when exposed to a low-pressure acoustic field (stable cavitation) and violent oscillations of the bubble and its consecutive rapid growth during the rarefaction phase, when they reach their size of resonance (inertial cavitation). The oscillating motion of stable cavitation causes rapid movement of fluid near the bubble (micro-streaming) and induces cell apoptosis. Currently, HIFU is used for the ablation of tumors in the liver, prostate, breast, and kidney, and benign thyroid nodules [18].

- I.3 Bibliography

1. Keller FS. Scrubbing with Charles Dotter on an angioplasty. J Vasc Interv Radiol. 2015 Mar;26(3):355-6. doi: 10.1016/j.jvir.2014.11.015.

2. de Baere T. The IR Evolution in Oncology: Tools, Treatments, and Guidelines. Cardiovasc Intervent Radiol. 2017 Jan;40(1):3-8. doi: 10.1007/s00270-016-1503-2. Epub 2016 Nov 21.

3. Christensen CM. The innovator's dilemma. Brighton: Harvard Business School Press; 1997.

4. Lencioni R , Cioni D , Crocetti L , et al. Early stage hepatocellular carcinoma in patients with cirrhosis: long-term results of percutaneous image-guided radiofrequency ablation. Radiology 2005; 234 (3):961–967.

5. Ahmed M, Brace CL, Lee FT, Goldberg SN. Principles of and advances in percutaneous ablation. 2011;258(2) 351-69.

7. Goldberg SN, Gazelle GS, Halpern EF, Rittman WJ, Mueller PR, Rosenthal DI. Radiofrequency tissue ablation: importance of local temperature along the electrode tip exposure in determining lesion shape and size. Acad Radiol 1996;3(3): 212–218.

8. Haemmerich D, Pilcher TA. Convective cooling affects cardiac catheter cryoablation and radiofrequency ablation in opposite directions. Conf Proc IEEE Eng Med Biol Soc 2007;2007:1499–1502.

9. Ring ME , Huang SK , Gorman G , Graham AR. Determinants of impedance rise during catheter ablation of bovine myocardium with radiofrequency energy. Pacing Clin Electrophysiol 1989;12(9):1502–1513.

10. Lorentzen T. The loop electrode: in vitro evaluation of a device for ultrasound-guided interstitial tissue ablation using radiofrequency electrosurgery. Acad Radiol 1996;3(3): 219–224.

11. Lencioni R, Goletti O, Armillotta N, et al. Radio-frequency thermal ablation of liver metastases with a cooled-tip electrode needle: results of a pilot clinical trial. Eur Radiol 1998;8(7):1205–1211.

12. Wright AS, Sampson LA, Warner TF, Mahvi DM, Lee FT Jr. Radiofrequency versus microwave ablation in a hepatic porcine model. Radiology 2005;236(1):132–139.

13. Brace CL, Laeseke PF, Sampson LA, Frey TM, van der Weide DW, Lee FT Jr .Microwave ablation with a single small-gauge triaxial antenna: in vivo porcine liver model. Radiology 2007;242(2):435–440.

14. Strickland AD, Clegg PJ, Cronin NJ, et al. Experimental study of large-volume microwave ablation in the liver. Br J Surg 2002;89(8):1003–1007.

15. Stollberger R, Ascher PW, Huber D, Renhart W, Radner H, Ebner F. Temperature monitoring of interstitial thermal tissue coagulation using MR phase images. J Magn Reson Imaging 1998;8(1):188–196.

16. Veenendaal LM, de Jager A, Stapper G, Borel Rinkes IH, van Hillegersberg R. Multiple fiber laser-induced thermotherapy for ablation of large intrahepatic tumors. Photomed Laser Surg 2006;24(1):3–9.

17. Tatli S, Acar M, Tuncali K, Morrison PR, Silverman S. Percutaneous cryoablation techniques and clinical applications. Diagn. Interv. Radiol. 2010,16, 90–95.

18. Kennedy JE. High-intensity focused ultrasound in the treatment of solid tumours. Nat. Rev. Cancer 2005, 5, 321–327.

Chapter II

Invasive and non-invasive approaches for biological tissues temperature monitoring

- II.1 Invasive techniques

II.1.1 Thermocouples

A thermocouple consists of two dissimilar metal wires joined in two different junctions. The principle of operation is based on the Seeback effect, i.e., when two different or unlike metals are joined together at two junctions, an electromotive force (EMF) is generated at the two junctions, as shown in Fig. 2.1 [1].
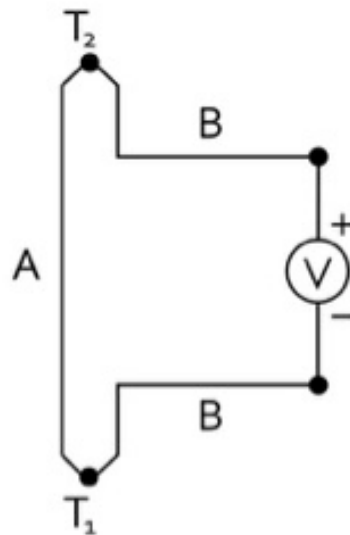
Fig. 2.1: Seeback Effect circuit. V is the electromotive force, A and B represent the two metallic wires, T1 and T2 the temperatures at the two junctions [1].

The amount of EMF generated changes for different combinations of the metals. In addition to this effect, there is the Thompson effect, which states that the EMF at the two junctions depends on the temperature difference between the junctions. EMF is a non-linear function, which can be approximated by a polynomial:

$$\Delta T = \sum_{n=0}^{N} a_n e^n$$

(1)

where polynomial coefficients a_n depend on materials and e^n is the EMF generated at the junctions. Thermocouples have a wide operative range, they are quite accurate for the specific application (average ±1 °C, up to ±2 °C) and their small size results in a rapid response time, varying from tens of microseconds to tens of milliseconds. Moreover, thermocouples are mostly cost-effective which make them one of the most used temperature sensors. Upon all the type of thermocouples, based on the couple of metal used, the most common is the K-type, whose conductors are Nickel-Chrome and Nickel-Aluminium, which have been used for this thesis' work. The operation range varies from producers but generally is from -100°C up to 300°C. The sensitivity of this sensor is about 41µV/°C so amplification and noise filtering are required [2].

During laser irradiation the conductor of the thermocouples strongly absorbs radiations causing a local increase of temperature, and, as consequence, an overestimation of tissue temperature. Investigations of this issue have been carried out during hyperthermia treatment since seventies [3] and, afterwards, during LTA.

First studies have shown that the increase of temperature due to direct laser absorption is almost instantaneous [4]. The magnitude of the artifact was considered to be the rise, or drop, of the temperature when the laser was turned on, or off. In order to better evaluate the artifact amplitude the laser was continually turned on and off and then performing an average on its value on several trials (Fig. 2.2).
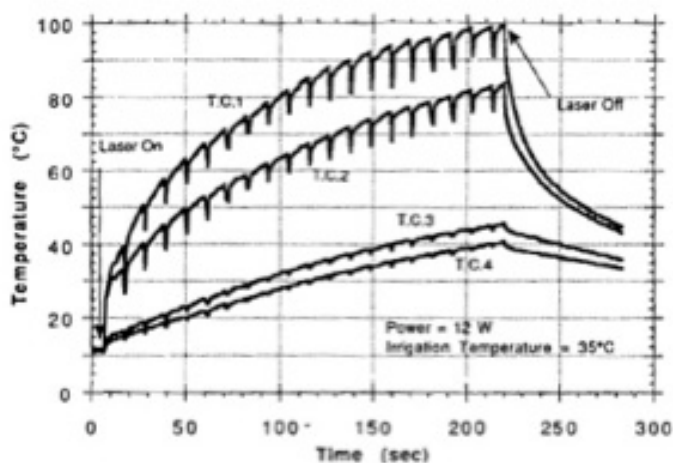
Fig. 2.2: Temperature increase measured by thermocouple at different distances from the laser: T.C.1 at 2 mm, T.C.2 at 4 mm, T.C.3 at 6 mm and T.C.4 at 10 mm [4].

As it can be seen from the picture above, the higher the distance between sensor and laser applicator tip, the lower is the overestimation of the temperature.

A later study performed another technique to quantify and correct the artifact. The temperature rise has been split in two different phenomena: one due to light absorption by the thermocouple and the other one caused by the light absorption of the tissue. The resulting equation for temperature rise assumed the form:

$$T_m(t) = A \cdot (1 - e^{-\frac{t}{\tau}}) + B \cdot t$$

(2)

Where T_m is the temperature measured and A, B and τ are constants, which assume a different value for each thermocouple. The exponential term represents light absorption by thermocouple and the linear term represents light absorption by the tissue. From this study, it emerges that the thermocouple artifact can reach value up to 18°C, so its correction is crucial [4].

Later, another study was performed using thermocouples as temperature sensors focused on the effect on LTA on the canine prostate [5]. Authors assumed that, at a constant laser power and the laser applicator not being in contact with the tissue, the temperature rises linearly with time. In order to have an accurate measurement they applied a correction for the thermocouple artifact. The correction they made, applied only on the tissue cooling curve, was based on the fact that the response time for laser-induced temperature change is much faster for the small thermocouple probes compared to the one affecting the tissue. They separated the thermocouple response from the tissue response and the resulting temperature has been assumed to be an exponential function:

$$T(t) = A + B \cdot e^{-Ct} + D \cdot e^{-Et}$$

(3)

being A, B, C, D, E constant parameters. The corrected tissue cooling curve was obtained by removing the exponential referred to the thermocouple (Fig. 2.3).
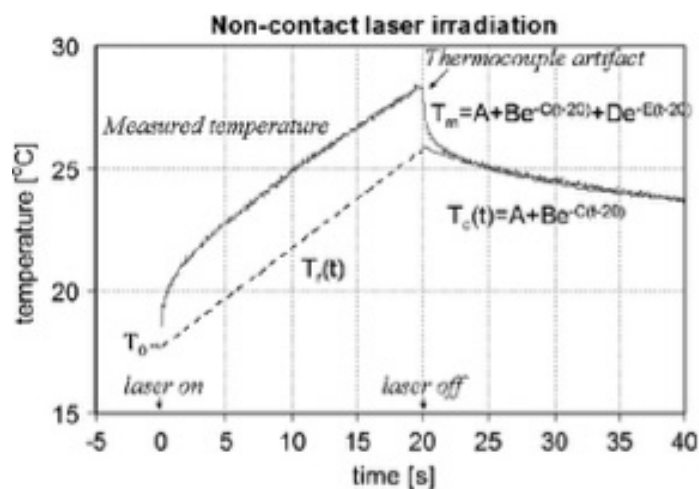
Fig. 2.3: Temperature recorded at 6 mm from the laser applicator and the artifact correction [5].

II.1.2 Fiber optic sensors

Among several fiber optic sensors, FBGs have gained large interest for monitoring temperature during hyperthermal treatments. FBGs are optical element photo-inscribed within the core of an optical fiber. Fiber optic is a thin, transparent and flexible filament whose purpose is to transport light. Optic fibers are considered as dielectric waveguides as they manage to transport an electromagnetic field, of relatively high frequency, without significant losses. Inside the optic fiber is possible to recognize (Fig. 2.4) three concentric regions: the core and the cladding, which are responsible for light transport and the buffer coating, whose purpose is to shield the whole fiber.
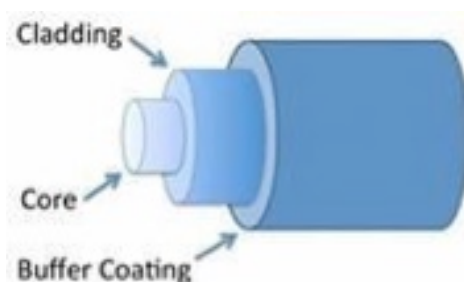
Fig. 2.4: Internal structure of the optic fiber

The operating principle of optic fiber is based on the total reflection of the electromagnetic wave. A luminous beam enter the core with a certain angle and propagates within the core because of reflection due to the separation surfaces between core and cladding. Due to the core refraction index (n_1) being higher than the one of the cladding (n_2), the wave travels without any substantial loss via multiple reflections (Fig. 2.5).
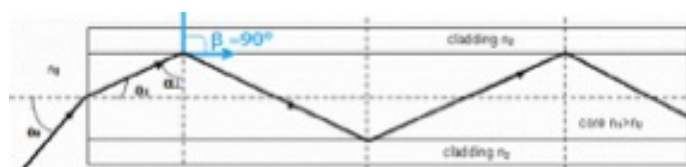
Fig. 2.5: Electromagnetic wave propagation.

FBGs are a particular type of optic fiber whose core's refraction index changes periodically. The gratings are realized by a process of photo-incision. During this process the core is exposed periodically to an ultraviolet light which produces a permanent increase of the refraction index with a constant step.

The grating is composed of stripes, with a different refraction index, at a known distance called gratings characteristic period. When a polychromatic radiation is sent trough the fiber, only a narrow range of wavelengths is reflected, whereas the others are transmitted, as shown in Fig. 2.6.
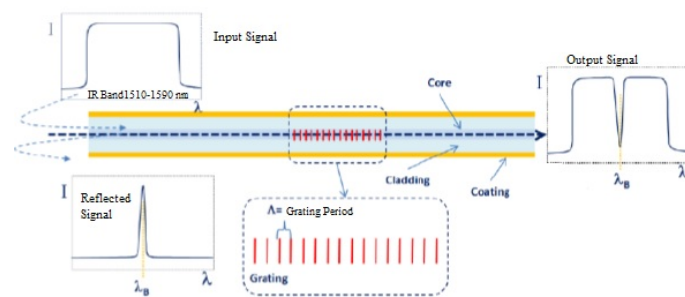
Fig. 2.6: Working principle of FBGs.

FBGs work as selective filters with the respect to one wavelength called Bragg wavelength (λ_B), which is a function of the gratings period (Λ) and the effective refraction index (n_{eff}) as reported in the following equation [6]:

$$\lambda_B = 2 \cdot \Lambda \cdot n_{eff}$$

(4)

A change of Λ or n_{eff} causes a variation in λ_B of the reflected electromagnetic wave. The working principle of the FBGs is based on the detection of the wavelength shift ($\Delta\lambda_B$) due to temperature change or strain. Fig. 7 shows the effect of the strain on the Bragg wavelength.
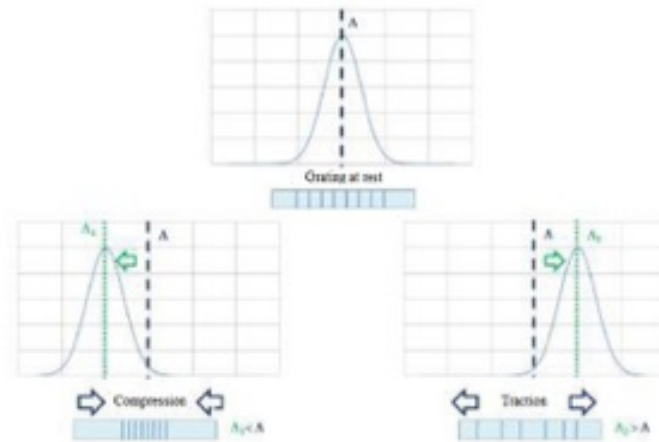
Fig. 2.7: Effect of compression on the right and of traction on the left.

The reflected wavelength variation caused by a relative variation of the grating period and of the effective refraction index is describe by the following equation:

$$\frac{\Delta \lambda_B}{\lambda_B} = \frac{\Delta \Lambda}{\Lambda} + \frac{\Delta n_{eff}}{n_{eff}}$$

(5)

The wavelength variation can be express in an explicit way in order to show the influence of temperature and strain:

$$\frac{\Delta \lambda_B}{\lambda_B} = P_e \cdot \varepsilon + \left[P_e \cdot (\alpha_s - \alpha_f) + \zeta \right] \cdot \Delta T$$

(6)

where P_e is the optic deformation coefficient, α_s [K^{-1}] and α_f [K^{-1}] are the thermal dilatation coefficient and ζ [K^{-1}] is the thermo-optic coefficient [7]. When FBGs are employed as temperature sensor the contribution of ε on wavelength variation can be neglected with the respect of ΔT, which is responsible for about the 95% of the shift.

In spite of the presence on the market of FBGs since the seventies, the technologies to mass-production and

systems that permit their application are quite recent. These reasons made the equipments cost quite high and caused a delay of their widespread use by the medical community. However, during the last decades, the interest on these sensors has grown due to the decrease of the cost of optical components and the increase of the product quality. Using FBGs sensors during LTA has some great advantages compared to the thermocouple. Firstly, they are electromagnetically inert, so they do no not have the above mentioned artifact. Secondly, they can be used either as reference during MR-based thermometry or as measuring systems during MR-guided procedures. They also present some other advantages, like biocompatibility, non-toxicity and chemical inertness.

The main drawback for the FBGs, apart that they require invasive approaches to monitor temperature, is the high equipment cost (i.e., the spectrum analyzer).

Finally, another strong disadvantage for invasive techniques is the need to have contact between the organ and the sensing element. Another drawback of using these invasive approaches is that several sensors are required to evaluate the temperature distribution inside the tissue.

- II.2 Non-invasive techniques

Non-invasive technology to measure tissue temperature in course of ablation procedure is based on radiological imaging. CT, MR and US have been described in this scenario, each with peculiar aspects in terms of spatial and temporal resolution. CT and MR are adopted more than US which presents some aspects still to investigate

concerning temperature >45°C. Great advantage among all is the avoidance of inserting any other device into the human body.

II.2.1 Computed Tomography

Images obtained by CT scan consist of a matrix of pixels, representing the average X-ray attenuation profile of the tissue in the corresponding voxels, three-dimensional elements whose dimensions depend on pixels size and on slice thickness (Fig. 2.8).
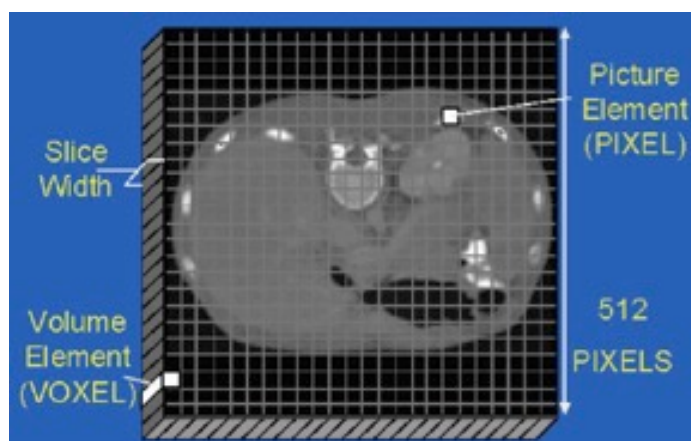
Fig. 2.8 Reconstructed CT slice according to pixels and voxels.

Voxels raw data are processed to obtain an attenuation value for each pixel of the final reconstructed image: the CT number, expressed in dimensionless Hounsfield Units:

$$CT(x,y) = \frac{1000 \cdot [\mu(x,y) - \mu_{H2O}]}{\mu_{H2O}}$$

(1)

where μ_{H2O} is the linear attenuation coefficient of water, and $\mu(x,y)$ is the average linear attenuation coefficient in the (x,y) voxel. X-ray attenuation at high energy levels used in CT scans (about 75 keV) is largely a result of

Compton scattering interaction with small contribution from Rayleigh scattering and the photoelectric effect. In this photon energy range, the energy loss due to these elementary processes is proportional to electronic tissue density, $\rho\varepsilon=NZ/A$, where A and Z are the atomic mass and atomic number respectively, and N is Avogadro's number. $\rho\varepsilon$ varies with physical density for a given material, ρ, whose dependence on linear attenuation coefficient μ can be written as follows:

$$\mu(T) = \mu_m \cdot \rho(T)$$

(2)

Where μ_m is the mass attenuation coefficient of the material.

It is well known that when a substance becomes warmer, its density is commonly reduced and the amount of density reduction is determined by its thermal expansion coefficient:

$$\rho(T) = \frac{\rho(T_0)}{1 + \alpha \cdot \Delta T}$$

(3)

Where T_0 is CT calibration temperature (about 20 °C) and $\Delta T = T - T_0$ is the temperature variation.

Hence, a change in density will result in a change in the observed CT number:

$$CT(T) \approx CT(T_0) - \frac{1000 \cdot \mu(T_0)\alpha\Delta T}{\mu_{H2O}(T_0)}$$

(4)

and the CT variation can be expressed as follows:

$$\Delta CT \approx -[1000 + CT(T_0)]\alpha\Delta T$$

(5)

This equation shows that changes in tissue temperature can be indirectly measured by monitoring the CT numbers of the tissue. The minus sign suggests that during

hyperthermia treatments the temperature increase causes a decrease of the CT numbers. To experimentally obtain the relationship [5], which correlates HU values and temperature samples extracted from CT scan and from common thermal sensors respectively, a calibration process is required. Before heating, little temperature probes, such as thermocouples or fiber optic sensors, are inserted through the tissue or phantom under examination. During hyperthermal procedure, the sample is scanned following a specific protocol (mAs, kVp, slice thickness etc.). Subsequently, in the reconstructed CT images regions of interest (ROIs), centered where the reference temperature sensors are placed, are chosen to calculate the mean CT number and the standard deviation. In order to investigate the relationship between local temperatures and area-averaged CT number, the calculated values are synchronized with the measured temperatures and a regression analysis is performed with the least-square fit method. For the most part of literature a linear model is confirmed, as proved by a high value of the Pearson's correlation coefficient (R^2). On the other hand, some isolated studies have shown that a quadratic or cubic fitting better agrees with experimental data than the linear model. The slope of the best fitting curve represents the thermal sensitivity of the tissue: a higher value of the slope is mainly due to a larger thermal expansion coefficient, leading to a greater variation in CT numbers with temperature and, thus, to a better resolution. The thermal sensitivity of the specific tissue allows estimating temperature distribution during the ablation process.

II.2.2 Magnetic Resonance

Minimally invasive thermal therapy of benign and malignant diseases benefits from near real-time MR image guidance. This is due to the attractive properties of MR imaging, such as its non-invasiveness, lack of ionizing radiation, and the ability to image in any scan orientation with good spatial and temporal resolution. MR allows building maps of *in vivo* body temperature that make it particularly well suited for guiding and monitoring minimally invasive thermal therapy [8].

The goal of MR image-guided thermal therapy is to use real-time temperature mapping to provide more control over the treatment outcome. Therefore, it is not only necessary to accurately measure the temperature during treatment, but also to be able to relate treatment temperature to actual thermal tissue damage.

A number of MR parameters show a sensitivity to temperature: the proton density, the T1 and T2 relaxation times, the diffusion coefficient and the proton resonance frequency (PRF).

Proton density

The proton density depends linearly on the equilibrium magnetization, M_0, which is determined by the Boltzmann distribution [9]:

$$PD \propto M_0 = \frac{N\gamma^2 h^2 I(I + 1)B_0}{3\mu_0 kT} = \chi_0 B_0$$

(1)

where N is the number of spins per volume, γ is the gyromagnetic ratio, h_{bar} is Planck's constant, I is the quantum number of the spin system (1/2 for protons), B_0 is the magnetic flux density, μ_0 is the permeability of free

space, k is the Boltzmann constant, T is the absolute temperature of the sample, and χ_0 is the magnetic susceptibility.

The relationship of χ_0 (susceptibility) and temperature is known as the Curie law:

$$\chi_0 \propto \frac{1}{T}$$

(2)

Because M_0 depends on the Boltzmann thermal equilibrium, it is possible to evaluate temperature changes based on proton density-weighted images. Please note that the proton density in the tissue itself does not change with temperature but rather the susceptibility which reflects the ratio of parallel and antiparallel spin populations. The temperature sensitivity of M_0 is inversely proportional to temperature and changes by -0.30 +/- 0.01%/°C [10] between 37°C and 80°C. From the change in proton density a relative temperature is calculated. However, the temperature dependency -0.3%/°C is small, requiring high signal-to-noise ratio (SNR), eg, an SNR of 100 is required for a temperature uncertainty of 3°C [11]. To eliminate effects from changes in T1 relaxation time, long repetition times close to 10 seconds are required, making the method less useful for real-time *in vivo* applications.

T1 Relaxation Time of Water Protons

The temperature dependence of the T1 relaxation time was first shown by Bloembergen *et al* and subsequently investigated by Parker [12] for non-invasive thermometry in MR imaging. Spin-lattice relaxation in biologic tissues results from dipolar interactions of macromolecules and water molecules, which arise from their translational and rotational motion.

The temperature dependence of this motion is reflected in changes to the spin-lattice relaxation time T1 [9], which increases with temperature. One model that describes the variation of the T1 relaxation time of water protons is [13]:

$$T_1 \propto e^{-E_\alpha(T_1)/kT}$$

(3)

where Ea(T1) is the activation energy of the relaxation process, k is the Boltzmann constant, and T is the absolute temperature.

Within a small temperature range T1 depends linearly on temperature, but both T1 and its temperature dependence are different for different tissues. The temperature dependence of the longitudinal relaxation times can be described as:

$$T_1(T) = T_1(T_{ref}) + m \cdot (T - T_{ref})$$

(4)

where m=dT1/dT is determined empirically for each tissue, and T_{ref} is the reference temperature. Temperature dependence was found to be in the order of 1%/°C, with values of 1.4%/°C in bovine muscle, 1–2%/°C in liver, and 0.97%/°C in fat [8].

The signal for both spin echo or gradient echo images can be expressed in terms of M_0, the flip angle α, the relaxation time T1, and the repetition time TR as:

$$S = M_0 sin\alpha \frac{1 - E_1}{1 - cos\alpha E_1}$$

(5)

where:

$$E_1 = \exp\left[-\frac{TR}{T_1(T_{ref}) + m(T - T_{ref})}\right]$$

(6)

The relative temperature sensitivity of the magnitude image dS/SdT is related to the rate of signal change with relaxation dS/dT1:

$$\frac{dS}{dT} = m \cdot \frac{dS}{dT_1}$$

(7)

Note that both M_0 and T1 change with temperature.

The signal decreases with increasing temperature both because the relaxation time increases and the magnetization decreases. The small non-linear temperature dependence on the equilibrium magnetization is often neglected or, alternatively, Eq. 7 is modified to [14]:

$$\frac{dS}{dT} = m \cdot \frac{dS}{dT_1} - \frac{S}{T^0}$$

(8)

where the second term on the right-hand side represents the decrease in the equilibrium magnetization with increasing absolute temperature, as given by Eq. 1. The spin–spin relaxation time T2 is also a function of temperature. The temperature dependence, however, is relatively small [15] and usually neglected. Using Eqs. 5 and 8, the temperature sensitivity dS/SdT is then given by:

$$\frac{dS}{SdT} = -\frac{mTR(1 - cos\alpha)E_1}{T_1(T_{ref})^2(1 - E_1)(1 - cos\alpha E_1)} - \frac{1}{T_{ref}}$$

(9)

The quality of T1-based thermal mapping depends on the accuracy of measuring and extracting T1. Many accurate T1 mapping methods such as inversion recovery and saturation recovery are time-consuming and not useful for monitoring thermal therapy, although single-shot methods partially alleviate the problem.

The quantification of temperature changes using T1 effect

is difficult because the temperature coefficient of the individual tissues is usually not known and the physiologic response of the living tissue to heat can seriously affect the quantification [16]. Non-linear effects can also occur if the tissue properties change, eg, due to coagulation, which has been found in *ex vivo* tissue to occur at temperatures as low as 43°C [17].

Because of these problems, T1 changes are often only used to get a qualitative measure of the temperature distribution. If only a qualitative temperature measurement is needed, T1-weighted images can be acquired rapidly and compared to or subtracted from baseline images acquired before heating. Fig. 2.9 gives an example of the signal decrease during RF-heating in a T1-weighted gradient echo image.
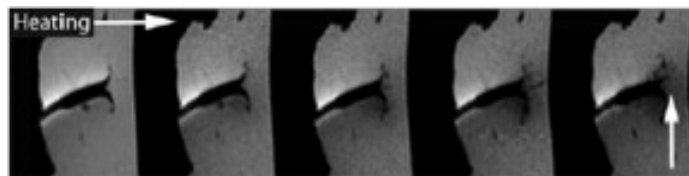
Fig. 2.9. T1-weighted gradient echo images acquired during RF-ablation of an ex vivo tissue sample, showing signal decrease in the heated region [18].

T1-change per °C increases with increasing field strength, but T1 contrast diminishes [18].

Thus, apart from SNR advantages at higher field, T1-based temperature mapping using T1-weighted images appears more sensitive at low field. T1-weighted images can be acquired with relatively motion-insensitive pulse sequences, but image registration between successive images has to be ensured. Fig. 2.10 shows an example of a T1-weighted thermosensitive gradient echo images to

monitor LTA [19].
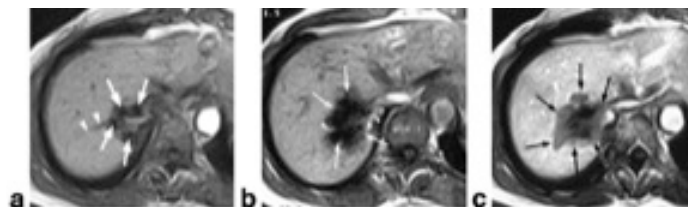
Fig. 2.10. MR images of a 50-year-old woman with liver metastases from breast cancer. The T1-weighted thermosensitive gradient echo sequence (TR/TE/flip angle: 140/12 msec/80°) shows the metastasis before starting the laser ablation. The arrows show the locations of the laser fibers (a). The same imaging sequence in an advanced phase (after 3 minutes) of the intervention shows a clear drop in signal intensity (arrows) in the heated area (b). Lesion temperature is approximately 110°C in the center and 60–70°C in the peripheral zone. A contrast enhanced image obtained immediately after laser treatment shows the coagulated area and documents the ablation of the tumor tissue (c) [19].

T2 Relaxation Time of Water Protons

A similar increase in T2 relaxation time with increasing temperature has been observed in aqueous solutions.

In tissue, however, water T2 is reduced by a significant factor compared to pure water and the temperature dependence of T2 can be masked by other factors. Observing a T2-weighted MR signal in tissue over temperature, the signal undergoes a pronounced decrease at higher temperatures and remains at the lower signal level during cooling to room temperature. This change in T2 relaxation could be a defining characteristic of irreversible tissue damage due to thermal coagulation.

The measured T2-change with temperature is therefore non-linear and shows a sigmoidal increase [20].

Diffusion – Brownian Molecular Motion

This method is based on the temperature dependence of the diffusion coefficient, D, which describes the thermal Brownian motion of an ensemble of molecules in a medium. The relationship between temperature and diffusion coefficient can be written as:

$$D \approx e^{-E_a(D)/kT}$$

(10)

where $E_a(D)$ is the activation energy of the molecular diffusion of water, k is the Boltzmann constant, and T is absolute temperature. The temperature dependence is described by:

$$\frac{dD}{DdT} = \frac{E_a(D)}{kT^2}$$

(11)

with a temperature sensitivity of about 2%/°C.

Random Brownian motion of molecules results in a Gaussian distribution of displacements. In the presence of strong magnetic field gradients the diffusion of the water molecules in the tissue causes a signal phase dispersion and subsequent signal attenuation in the direction of the diffusion gradients that is proportional to the distribution of water molecules. From diffusion coefficients D and D_{ref}, acquired at two different temperatures T and T_{ref}, respectively, the temperature change ΔT can be obtained:

$$\Delta T = T - T_{ref} = \frac{kT_{ref}^2}{E_a(D)} \frac{(D - D_{ref})}{D_{ref}}$$

(12)

It is assumed that the temperature change is small (ΔT << T_{ref}) and that E_a is independent of temperature. The diffusion method has been used to non-invasively measure temperature *in vivo* [21]. Its temperature sensitivity is high, but acquisition times are relatively long and *in vivo*

implementation suffer from an extremely high sensitivity to motion. Single-shot echo planar imaging and line-scanning techniques [22] have also been used to reduce the acquisition time and motion sensitivity of this method. An additional complication *in vivo* is that the temperature dependence of diffusion becomes non-linear when tissue conditions change. The motility of water in tissue depends on barriers such as cellular structures, proteins, and membranes. Heat induced changes like protein coagulation, therefore, can lead to large changes in the diffusion coefficient. In tissues with anisotropic diffusion, eg, muscle fibers, the mobility of water protons is dependent on direction. For accurate temperature measurements, calculations of the full diffusion tensor, which describes the anisotropy, or the trace, which is rotationally invariant, might be necessary, but these methods require more acquisition time than a diffusion measurement in a single direction. Lipid suppression is necessary in tissues containing fat, because fat has a different change in diffusion coefficient with temperature.

PRF Shift of Water Protons

The resonance frequency of a nucleus in a molecule is determined by the local magnetic field it experiences. The field at the nucleus can be written as:

$$B_{loc} = B_0 - B_{0s} = (1 - s)B_0$$

(13)

where s is called the shielding constant or screening constant and is dependent on the chemical environment. As a result of the nuclear shielding, the resonance frequency becomes:

$$\omega = \gamma B_0 (1 - s)$$

(14)

In water molecules the hydrogen nuclei ^{1}H are screened from the macroscopic field by the electrons of the molecule. A ^{1}H nucleus in a free H_2O molecule is screened more efficiently by the electron cloud than a nucleus in an H_2O molecule, which is hydrogen bonded to another molecule. Hydrogen bonds between neighboring molecules distort the electronic configuration of the molecules, which reduces the electronic screening.

The fraction and the nature of the hydrogen bonds in water vary with temperature. As the temperature increases, the hydrogen bonds stretch, bend, and break [23], ie, on average the H_2O molecules spend less time in a hydrogen-bonded state. Consequently, there is more electron screening of the ^{1}H nucleus, and thus a lower local magnetic field block and a lower proton resonance frequency. Because of its physical origins on hydrogen bonding among water molecules, electron screening is considered a microscopic effect.

The temperature-dependent component varies linearly with temperature in the temperature range of interest for thermal ablation and can be described as:

$$S_t(T) = \alpha T$$

(15)

The average electron-screening constant of pure H_2O varies approximately linearly with temperature by about -1.03 +/- 0.02 * 10^{-8}/°C over a wide range in temperatures from -15°C to 100°C, including the temperature range of interest for interventional procedures.

Temperature imaging based on the PRF shift has evolved into two techniques, spectroscopic imaging and phase mapping methods.

Spectroscopic imaging using the PRF Shift

Proton spectroscopic imaging, like PRF shift thermometry using phase mapping, utilizes the temperature-induced water proton chemical shift. The shift is measured between the water peak and a reference peak that remains constant with temperature, such as lipids or N-acetyl-aspartate in the brain [24].

Proton chemical shift imaging (CSI) sequences have been shown to measure absolute temperature distributions within 1 minute or less and a spatial resolution of 3–4 mm. Different acquisition methods have been proposed for spectroscopic temperature measurements, such as single voxel spectroscopy, magnetic resonance spectroscopic imaging (MRSI), echo planar spectroscopic imaging (EPSI), and line scan echo planar spectroscopic imaging (LSPESI).

The ability of spectroscopic imaging to determine absolute temperatures makes it a unique tool for noninvasive temperature measurements, but has currently limited applicability for real-time temperature monitoring due to its low temporal and spatial resolution.

Phase Mapping Using the PRF Shift

MRI-derived temperature maps can be constructed using a gradient-recalled echo (GRE) imaging sequence by measuring the phase change resulting from the temperature-dependent change in resonance frequency (Fig. 2.11).
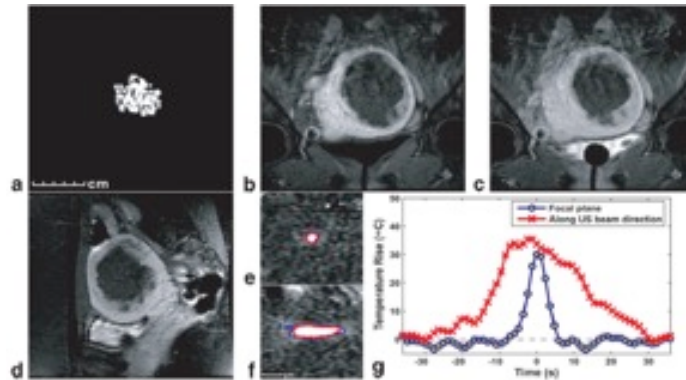
Fig. 2.11 Images and temperature measurement during MRI-guided focused ultrasound thermal ablation of a uterine fibroid. a: Thermal dose maps estimated from the MR thermometry acquired during treatment. Thresholds of 18 and 240 equivalent min at 43°C are shown. b,c: Coronal posttreatment contrast-enhanced T1-weighted MR images in the focal plane acquired immediately after contrast injection (b) and 5 minutes later (c). The affected fibroid tissue and nonperfused volume are larger than would be expected from the thermal measurements, presumably due to vessel occlusion during the treatment. d: Sagittal contrast-enhanced T1-weighted image (along the direction of the ultrasound beam). e,f: Thermal images acquired during two sonications in this fibroid with imaging oriented in the focal plane (e) and along the ultrasound beam direction (f). Based on the thermal dose, the lesion volume for these 20s sonications was 0.7 cm^3 (g) Temperature distribution through the focus at peak temperature rise for the two sonications in e,f [24].

In order to eliminate temperature-independent contributions, eg, due to B_0 field inhomogeneities, one or more images are usually acquired before heating and subtracted from images during heating. The phase difference images are proportional to the temperature-dependent PRF change and the echo time TE and can be converted to a temperature change by:

$$\Delta T = \frac{\phi(T) - \phi(T_0)}{\gamma \alpha B_0 TE}$$

(16)

where $\phi(T)$ is the phase in the current image, $\phi(T_0)$ is the phase of a reference (baseline) image at a known temperature, γ is the gyromagnetic ratio, α is the PRF change coefficient, B_0 is the magnetic field strength, and TE is the echo time.

The echo time TE can be optimized to increase the phase contrast-to-noise ratio and thereby the temperature accuracy, which is identical to the standard deviation in the temperature image σ_T. In a GRE sequence, the temperature-dependent phase difference signal-to-noise ratio, $SNR_{\Delta\phi}$, is estimated as follows:

$$SNR_{\Delta\phi} = \left| \frac{\Delta\phi(\Delta T)}{\sigma_{\Delta\phi}} \right|$$

(17)

where $\Delta\phi/(\Delta T)$ is the phase difference and $\sigma_{\Delta\phi}$ is the standard deviation of the phase difference image. With $\sigma_{\Delta\phi} = \sigma/A$, where A is the signal amplitude, the phase difference SNR is directly proportional to the signal intensity:

$$SNR_{\Delta\phi} \propto |\Delta\phi(\Delta T)| \cdot A$$

(18)

The GRE signal intensity, A, is dependent on tissue parameters, ρ, T1 and T2*, as well as on the imaging parameters of the GRE sequence, TE, TR, and flip angle. Assuming the tissue parameters are relatively constant, the signal intensity only depends on the imaging parameters. Except for adipose tissue, the PRF thermal coefficient is tissue type-independent and exhibits only a small dependence on thermal history even when tissue has been coagulated [25].

The tissue type-independence of the PRF shift is only true for aqueous tissues. In water, the dependence of the PRF

on temperature is attributed to changes in the hydrogen bonds, which are absent in fat. Therefore, the temperature dependence in adipose tissue is almost completely determined by susceptibility effects. The resulting temperature sensitivity of fat is some orders of magnitude smaller [26], indicating that thermometry inside fatty tissue is difficult.

The fact that the lipid resonance frequency is almost temperature-independent poses an important problem for temperature measurements using PRF. Many biological tissues are composed of both water and fat.

The presence of lipids modifies the phase difference obtained in the thermometry experiment and thus leads to temperature errors. Lipid suppression and/or selective excitation are therefore commonly used on high-field scanners.

PRF-based temperature mapping has found by far the greatest acceptance. For many applications at mid-field (0.5–1.5 T), MR thermometry provides high temporal and spatial resolution to precisely monitor the temperature distribution within the targeted tissue and predicts the outcome of the thermal treatment. For thermal therapies, real-time can be defined as an update time that is small compared to a significant change in temperature during treatment. In thermal ablation an update time of 1 second or less can be necessary. For slow update rates, imaging times are not an issue, but for long exposure times effects such as tissue motion can become a problem. As acceleration in many cases comes at the cost of SNR reduction and increased temperature uncertainty, acquisition parameters for a given fast-imaging sequence

should be chosen carefully to achieve the optimal compromise for a specific situation.

Fast temperature mapping can be achieved with gradient-echo echoplanar imaging (EPI) or segmented-EPI acquisitions [27].

Motion artifacts

Motion is the most prevalent problem for temperature monitoring with PRF phase mapping and the main reason that has impeded its acceptance for clinical application in areas that are subject to motion.

For temperature monitoring during thermal treatment, motion artifacts can be divided into two categories, intrascan motion and interscan motion, based on the time scale of the motion with respect to the image acquisition time. Intrascan motion is caused by movement of an object during MR image acquisition, resulting in a poor quality image with typical blurring and ghosting artifacts. These motion artifacts are not specific to PRF temperature imaging and can be reduced by accelerating the image acquisition. Interscan motion occurs due to motion or displacement of an object between the acquisition of consecutive images. Temperature images obtained using the PRF method are usually reconstructed by calculating the phase difference between a baseline image acquired prior to heating and the current heating image. If motion is present between the acquisition of the images the images are not registered to the baseline and artifacts in the temperature maps occur. New baseline images cannot be acquired once the thermal procedure has started until the heated region has returned to baseline temperature. Unfortunately, many of the target areas for thermotherapy

are in the abdomen, where motion is ubiquitous.

A major source of motion, especially in the upper abdominal organs, is respiration. Respiration not only displaces the organs but also changes the susceptibility field. But even without respiratory motion, displacement between images can occur. Thermal coagulation leads to structural changes and deformation of the treated tissue, which can be observed *ex vivo* without any other source of motion present. This heating-induced tissue motion is often not a simple global displacement; the tissue swells in three dimensions, causing a local warping of the field distribution at the position of the swelling. In vivo, swelling during the treatment and changes in muscle tension, or peristalsis, can also cause tissue displacement. Different strategies to overcome the problem with motion have been proposed. Some methods are specifically designed for repetitive motion due to respiration and others use a more general approach to deal with nonrepetitive motion as well.

In the case of respiration the motion can be monitored with external methods and synchronized with MR imaging such that image acquisition occurs during a stable period of the breathing cycle. Respiratory gating during free breathing has been used [28], but gating can fail when the respiratory cycle is irregular, leading to motion artifacts and errors in the temperature maps.

A method becomes non-sensitive both to repetitive and non-repetitive interscan motion if the need of baseline image subtraction is eliminated. One approach, called referenceless thermometry or self-referenced thermometry, tries to estimate the heating from every individual image itself, without a preheating reference

scan. The background phase inside the heating region is estimated by fitting a polynomial function to the unwrapped background phase or a complex valued polynomial [29] to the complex image outside the heating region using a weighted least-squares fit. The extrapolation of the polynomial to the heated region serves as the background phase estimate, which is then subtracted from the actual phase. These methods require a heating area that is at least partially surrounded by a non-heated region with sufficient SNR; this is often the case for thermal ablation procedures. Because of echo time-dependent phase discontinuities between water and fat regions, which would inhibit polynomial fitting, fat needs to be suppressed or the reconstruction algorithm should be modified to be able to handle both tissue types.

MR thermometry has been shown to be an excellent modality to noninvasively monitor thermal therapy to ensure efficacy and safety of the treatment.
Temperature monitoring has been successfully demonstrated in vivo and is regularly used in a number of clinical applications, mainly in combination with HIFU heating. However, a number of challenges remain for MR thermometry to be widely accepted for monitoring thermal procedures. Because the target of many ablation procedures lies in the abdomen, reliable and robust motion-insensitive acquisition techniques and reconstruction algorithms are indispensable.
Finally, to date, only T1, Diffusion, and PRF have been used for *in vivo* temperature monitoring during thermal therapy.

II.2.3 Ultrasound

The ideal ultrasound ablation monitoring system would provide accurate, precise and quick measurements of tissue temperature in the range from 37 °C to boiling. Unlike MR thermometry, however, "nature is not kind" and conspires against the use of ultrasound thermometry above 50 °C through a variety of physical and acoustic complexities, including non-linear temperature dependencies of contrast parameters, tissue phase transitions, and the stochastic generation of cavitation bubbles. In general, ultrasound thermometry is only applicable for tissue hyperthermia but not for tissue ablation, where nonthermometric ultrasound methods are required for therapy monitoring.

B-mode imaging

The correlation between increased echogenicity and temperature in tissue is slight. In one study, a correlation coefficient of r. 0.455 was reported [30]. It is assumed by many groups that the relationship between B-mode echogenicity and temperature is complicated by the fact that the structures that result in increased echogenicity (and in some cases post-lesion shadowing) also severely modulate the ablation energy and the subsequent temperature distribution, potentially leading to over-treatment; the feedback from the imaging modality is often qualitative [31].

Alvarenga, Teixeira and collaborators [32] have studied the possibility of using the Gray-level co-occurrence matrix (GLCM), the GLCM-derived entropy, and the average greylevel content (AVGL) to estimate temperature *in vivo*. Since there is excellent correlation

between temperature and these B-mode image-derived indices up to 44 °C, these easy to implement methods could be utilised for quantitative monitoring of hyperthermia. Unfortunately, proof-of-principle studies have been limited to only phantoms and tissue samples.

Speckle tracking and thermal strain imaging

In an imaging scenario with no motion, the apparent displacements of the ultrasound speckle due to localised heating is correlated with both changes in the speed of sound (SOS) and thermal expansion of the tissue. Local displacements can be estimated from the time shifts Δt in the RF data, and given a known SOS c_0 at baseline temperature T_0, the temperature change can be related to the rate of change of time shifts with depth z:

$$\Delta T \approx \frac{c_0}{2} \frac{1}{\alpha - \frac{1}{c_0}\frac{\partial c}{\partial T}} \frac{\partial}{\partial z}(\Delta t)$$

where α (°C^{-1}) is the thermal expansion coefficient and the SOS sensitivity to temperature is known:

$$\left(\frac{\partial c}{\partial T} \approx -5 \frac{m}{s(^0)c} \right)$$

This linear relationship is most often assumed to be valid for hyperthermia below 50 °C. In the range above 50 °C up to phase transitions such as coagulation, the relationship is non-linear and may be difficult to calibrate. Since both the thermal expansion and the change in ultrasound velocity lead to shifts, it is important to understand the relative contribution of these two competing processes. In general, the change in SOS dominates thermal expansion by an order of magnitude [33]. Souchon and colleagues modelled the contributions of thermal expansion and SOS change in a one-

dimensional model [34]. As shown in Fig. 2.12, the largest echo strain is shifted to lower temperatures compared to the temperature of maximum speed of sound. Thus, there is the potential for quantitative temperature measurements above 60 °C provided that the speckle pattern is not destroyed by coagulation or other destructive phenomena.
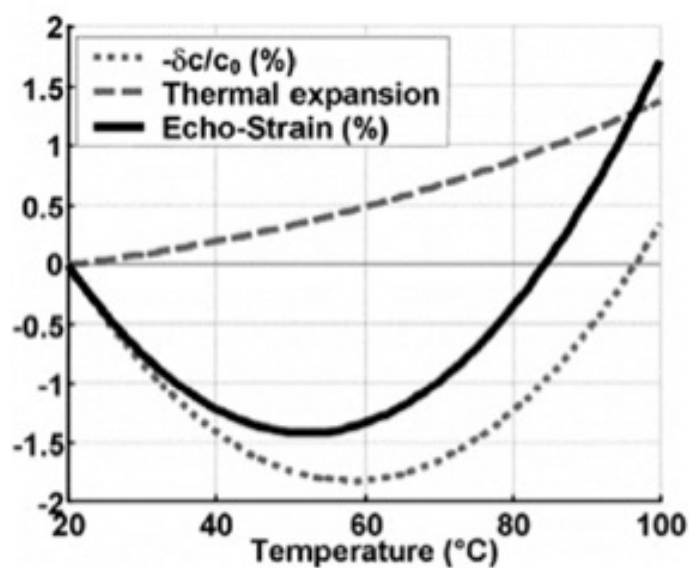
Fig. 2.12. 1D simulation of relative contributions of speed-of-sound change and thermal expansion to observed strain [34].

Thermal strain imaging has been one of the most prolifically studied methods for estimating temperature with ultrasound [35]. The achievable spatial resolution of thermal strain imaging is limited by the size of the spatial kernel utilised in speckle tracking which directly influences both the SNR and the spatial resolution of the strain image, but with opposite effects. The optimal kernel may be tissue and depth dependent.

Tissue stiffness monitoring and elastography

The mechanical properties of soft tissue are temperature dependent, and both bulk and shear elastic properties exhibit changes with temperature [36]. The temperature dependence is non-linear, with a large transition occurring when tissues undergo thermal coagulation [37]. A number of groups have investigated the possibility of exploiting this physical property of tissue to monitor or control a thermal ablation therapy with both ultrasound and MRI. Most efforts have focused on utilising this effect for mapping or visualising the region of thermal coagulation in tissue after treatment is completed due to the large change in mechanical properties that occur after reaching this end point in tissue.

Shear wave thermometry

Imaging of shear wave propagation in tissues is possible with both MRI and ultrasound [38]. In the case of ultrasound this can be accomplished by generating tissue displacements remotely in tissue through the radiation force principle or low frequency mechanical stimulation. The displacement of tissues results in shear waves propagating from the location of the displacement, at a speed of approximately 2–8 m/s. Ultra-fast ultrasound imaging can be used to track the propagation of these shear waves, which is related to the underlying shear elastic properties of the tissue. One method developed for this type of imaging is referred to as supersonic shear wave imaging [39] in which a series of localised focal regions are generated in a linear fashion with depth in tissue, generating a cylindrical shear wave around these points. This serves to cover an entire imaging field of view with shear waves, enabling mapping of the elastic

properties throughout a region of interest. One of the first applications investigated with this technique was the visualisation of thermally induced lesions in tissue due to the inherent change in elastic properties upon undergoing thermal coagulation [40]. A factor of three-fold increase in shear modulus was measured in coagulated chicken breast using this technique in this preliminary study. Subsequent to this work, the same group demonstrated the abilit to visualise thermal lesions after RF ablation *in vivo* in a pig model using shear wave imaging. In this study, the mean elasticity of lesions was 38.1±2.5 kPa vs. 6.4± 0.3 kPa in normal liver. The authors concluded that by using a threshold of 20 kPa, the presence of coagulation could be detected with a sensitivity of 0.8 and a positive predictive value of 0.83 *in vivo*, which represents some of the best data to date reported for ultrasound imaging of coagulated tissue. In addition to visualisation of thermal coagulation in tissues, Arnal *et al.* [41] investigated the temperature dependence of the shear modulus using shear wave imaging, to evaluate the potential to use this imaging method for thermometry. The changes in shear modulus with temperature were compared to the temperature also measured with ultrasound imaging and a strong correlation was observed for heating below 40 °C. These measurements in *ex vivo* tissue samples indicated a change of approximately 1 kPa/°C in muscle and the authors suggested this may have application for monitoring temperature changes below 45 °C. They also claimed that this method was very robust to motion, which overcomes one of the limitations of traditional echo-shift approaches for ultrasound thermometry. Similar trends in the shear modulus with temperature and coagulation have been

observed in other studies using 1D transient elastography [42]. Sapin-de Brosses *et al.* performed a series of studies investigating the relationship between shear modulus as measured with shear wave imaging and thermal dose in excised tissues and in vivo [36]. As highlighted in Fig. 2.13, these studies identified a strong dependence of shear modulus with temperature and thermal dose, with different trends observed across tissue types and in the case of muscle depending on the orientation of the measurement with respect to fibre orientation. So changes in stiffness observed with shear wave imaging were indicative of cellular necrosis.
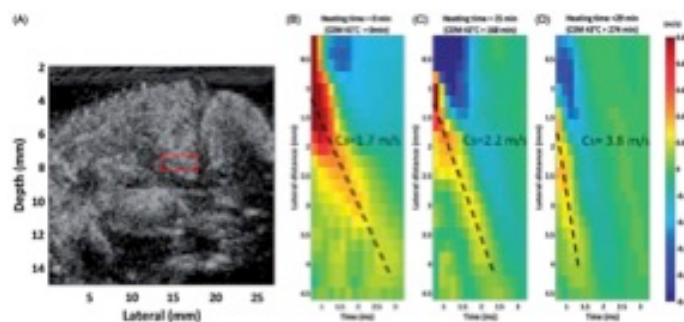
Fig. 2.13. Variation of shear wave velocity as a function of temperature, as assessed using shear wave elastography [36].

As summarized in Table 1, US methods have made significant progress in the area of thermometry for hyperthermia below 50 °C and in qualitative ablation monitoring which targets tissue coagulation and bubble formation. There is, however, a dearth of evidence that robust ultrasound thermometry exists for temperatures above 50 °C. This shortcoming is at present adequately filled by the availability of mature MR thermometry techniques. While axial shear strain elastograms have

shown promise for improved performance at high temperatures, it is unknown whether this new technique has the quantitative precision required for real-time control.

One possible route for improvement is the combination of two or more techniques into a multi-parametric analysis; however it is unknown at this time whether any combination of the methods described can expand the quantitative thermometry regime to treatment temperatures above 50 °C. With elastography modes now routinely available on clinical scanners, ultrasound thermometry based on thermal strain imaging may be the most appropriate technique for future clinical evaluation for thermal therapies above 50 °C.

Table 1.1 Summary of various methods for ultrasound thermometry and ablation monitoring.

Methods	Relative thermometry	Absolute thermometry	Quantitative. 37–50 °C	Quantitative. >50 °C	Ablation monitoring	Detects cavitation and boiling	Implementable using current clinical equipment
PRF MR thermometry	✓		✓	✓			✓
Spectroscopic MR thermometry	✓	✓	✓	✓			✓
CT thermometry	✓			✓			✓
B-mode imaging					✓	✓	✓
Nakagami imaging					✓		✓
Thermal strain imaging	✓		✓				✓
Shear wave thermometry	✓		✓		✓		
Local harmonic motion					✓		
Stimulated acoustic emissions	✓		✓				
Backscattered energy and QUS	✓		✓				✓
Transmission imaging and ultrasound tomography	✓	✓	✓		✓		
Passive monitoring					✓	✓	✓
Photoacoustics	✓		✓				

II.3 Bibliography

1. Rossi G. Misure Meccaniche e Termiche, Carocci Editore

2 . http://www.thermometricscorp.com/index.html

3. Christensen DA. Thermal Dosimetry and Temperature meaurements, Cancer Res.1979

4. Anvari B, Motamedi M, Torres JH et al. Effects of surface irrigation on thermal response of tissue during laser irrdiation, Laser in Surgery and Medicine 1994

5. Manns F. et al. In situ temperature measurements with thermocouple probes during laser interstitial thermotherapy (LITT): quantification and carrection of a measurement artifact, Laser in Surgery and Medicine 1998.

6. van Nimwegen SA, L'Eplattenier HFL, Rem AI et al. Nd:YAG surgical laser effects in canine prostate tissue: temperature and damage distribution, Physics in medicine and biology 2009

7. Lee B. Review of the present status of optical fiber sensors. Optical Fiber Technology 2003

8. Rieke V, Butts Pauly K. MR Thermometry. Journal of Magnetic Resonance Imaging 27:376-390 (2008).

9. Abragam A. The principles of nuclear magnetism. Oxford: Clarendon Press; 1983.

10. Johnson F, Eyring H, Stover B. Theory of rate processes in biology and medicine. New York: John Wiley & Sons; 1974.

11. Chen J, Daniel BL, Pauly KB. Investigation of proton density for measuring tissue temperature. J Magn Reson Imaging 2006;23:430–434.

12. Parker DL. Applications of NMR imaging in hyperthermia: an evaluation of the potential for localized tissue heating and noninvasive temperature monitoring. IEEE Trans Biomed Eng 1984;31:161–167.

13. Parker DL, Smith V, Sheldon P, Crooks LE, Fussell L. Temperature distribution measurements in two-dimensional NMR imaging. Med Phys 1983;10:321–325.

14. Cline HE, Hynynen K, Schneider E, et al. Simultaneous magnetic resonance phase and magnitude temperature maps in muscle. Magn Reson Med 1996;35:309–315.

15. Nelson TR, Tung SM. Temperature dependence of proton relaxation times in vitro. Magn Reson Imaging 1987;5:189–199.

16. Young IR, Hand JW, Oatridge A, Prior MV. Modeling and

observation of temperature changes in vivo using MRI. Magn Reson Med 1994;32:358-369.

17. Peller M, Reinl HM, Weigel A, Meininger M, Issels RD, Reiser M. T1 relaxation time at 0.2 Tesla for monitoring regional hyperthermia: feasibility study in muscle and adipose tissue. Magn Reson Med 2002;47:1194–1201.

18. Fung BM, Durham DL, Wassil DA. The state of water in biological systems as studied by proton and deuterium relaxation. Biochim Biophys Acta 1975;399:191–202.

19. Mack MG, Straub R, Eichler K, Sollner O, Lehnert T, Vogl TJ. Breast cancer metastases in liver: laser-induced interstitial thermotherapy—local tumor control rate and survival data. Radiology 2004;233(2):400–409.

20. Graham SJ, Bronskill MJ, Henkelman RM. Time and temperature dependence of MR parameters during thermal coagulation of ex vivo rabbit muscle. Magn Reson Med 1998;39:198–203.

21. Bleier AR, Jolesz FA, Cohen MS, et al. Real-time magnetic resonance imaging of laser heat deposition in tissue. Magn Reson Med 1991;21:132–137.

22. Schneider WG, Bernstein HJ, Pople JA. Proton magnetic resonance chemical shift of free (gaseous) and associated (liquid) hydride molecules. J Chem Phys 1958;28:601–607.

23. Cady EB, D'Souza PC, Penrice J, Lorek A. The estimation of local brain temperature by in vivo 1H magnetic resonance spectroscopy. Magn Reson Med 1995;33:862–867.

24. Peters RD, Hinks RS, Henkelman RM. Ex vivo tissue-type independence in proton-resonance frequency shift MR thermometry. Magn Reson Med 1998;40:454–459.

25. Kuroda K, Oshio K, Mulkern RV, Jolesz FA. Optimization of chemical shift selective suppression of fat. Magn Reson Med 1998;40:505–510.

26. Weidensteiner C, Quesson B, Caire-Gana B, et al. Real-time MR temperature mapping of rabbit liver in vivo during thermal ablation. Magn Reson Med 2003;50:322–330.

27. Lepetit-Coiffe M, Quesson B, Seror O, et al. Real-time monitoring of radiofrequency ablation of rabbit liver by respiratory-gated quantitative temperature MRI. J Magn Reson Imaging 2006;24:152–159.

28. Kuroda K, Kokuryo D, Kumamoto E, Suzuki K, Matsuoka Y,

Keserci B. Optimization of self-reference thermometry using complex field estimation. Magn Reson Med 2006;56:835–843.

29. Rieke V, Kinsey AM, Ross AB, et al. Referenceless MR thermometry for monitoring thermal ablation in the prostate. IEEE Trans Med Imaging 2007;26:813–821.

30. Mast TD, Salgaonkar VA, Karunakaran C, Besse JA, Datta S, Holland CK. Acoustic emissions during 3.1 MHz ultrasound bulk ablation in vitro. Ultrasound Med Biol 2008;34:1434–48.

31. Ge HY, Miao LY, Wang JR, Xiong LL, Yan F, Zheng CS, et al. Correlation between ultrasound reflection intensity and tumor ablation ratio of late-stage pancreatic carcinoma in HIFU therapy: Dynamic observation on ultrasound reflection intensity. Sci World J 2013;852874:1–10.

32. Alvarenga AV, Teixeira CA, Ruano MG, PereiraWCA. Influence of temperature variations on the entropy and correlation of the Grey-Level Co-occurrence Matrix from B-mode images. Ultrasonics 2010;50:290–3.

33. Maass-Moreno R, Damianou CA. Noninvasive temperature estimation in tissue via ultrasound echo-shifts. Part I. Analytical model. J Acoust Soc Am 1996;100:2514–21.

34. Souchon R, Bouchoux G, Maciejko E, Lafon C, Cathignol D, Bertrand M, et al. Monitoring the formation of thermal lesions with heat-induced echo-strain imaging: A feasibility study. Ultrasound Med Biol 2005;31:251–9.

35. Varghese T, Zagzebski JA, Chen Q, Techavipoo U, Frank G, Johnson C, et al. Ultrasound monitoring of temperature change during radiofrequency ablation: Preliminary in-vivo results. Ultrasound Med Biol 2002;28:321–9.

36. Sapin-de Brosses E, Gennisson JL, Pernot M, Fink M, Tanter M. Temperature dependence of the shear modulus of soft tissues assessed by ultrasound. Phys Med Biol 2010;55:1701–18.

37. Shahmirzadi D, Hou GY, Chen J, Konofagou EE. Ex vivo characterization of canine liver tissue viscoelasticity after highintensity focused ultrasound ablation. Ultrasound Med Biol 2014; 40:341–50.

38. Glaser KJ, Manduca A, Ehman RL. Review of MR elastography applications and recent developments. J Magn Reson Imaging 2012;36:757–74. 39. Bercoff J, Tanter M, Fink M. Supersonic shear imaging: A new technique for soft tissue elasticity mapping. IEEE

Trans ultrason Ferroelectr freq control 2004;51:396–409.

39. Bercoff J, Pernot M, Tanter M, Fink M. Monitoring thermally induced lesions with supersonic shear imaging. Ultrason Imaging 2004;26:71–84.

40. Mariani A, Kwiecinski W, Pernot M, Balvay D, Tanter M, Clement O, et al. Real time shear waves elastography monitoring of thermal ablation: In vivo evaluation in pig livers. J Surg Res 2014;188:37–43.

41. Arnal B, Pernot M, Tanter M. Monitoring of thermal therapy based on shear modulus changes: I. Shear wave thermometry. IEEE Trans Ultrason Ferroelectr Freq Control 2011;58:369–78.

42. Benech N, Negreira CA. Monitoring heat-induced changes in soft tissues with 1D transient elastography. Phys Med Biol 2010;55: 1753–65.

Chapter III

Fiber Bragg grating sensors for temperature monitoring

- III.1 Introduction to Fiber Bragg grating sensors

Fiber Bragg grating (FBG) sensors present relevant advantages compared to other invasive sensors for temperature monitoring (e.g., thermocouples): they are not metallic and so do not highly absorb laser light (not causing overestimation of tissue temperature), being MR compatible; in addition, they have a small size and are able to monitor temperature with fast response, so they provide an accurate temperature measurements even in case of abrupt temperature changes; finally, more than one FBG can be embedded within a single fiber optic, this feature allows performing multiple-point measurements. The main drawback is their sensitivity to strain, which could entail measurement error during *in vivo* application, where patient movements, also due to respiration, may strain the FBG.

The experimental sessions have produced the development of a sensorized needle with FBG for monitoring temperature distribution; my personal contribution has provided the experimental validation during LTA and MWA on *ex vivo* swine liver. Furthermore I have conducted an experimental session *in vivo* on an animal model in order to validate the sensorized needle during

RFA on a swine healthy liver (anatomical features similar to human).

- III.2 Working principle of fiber Bragg gratings

FBGs are elements embedded in a short segment of optical fiber [1]. They consist of a periodic variation in the reflective index of the fiber core. The grating is characterized by its spatial period, Λ [m], and the effective reflective index, n_{eff}. When interrogated with a polychromatic radiation, a narrow range of wavelengths is reflected, the other wavelengths are transmitted. The reflected spectrum is centered around a specific value, i.e., Bragg wavelength (λ_B), expressed as follows:

$$\lambda_B = 2 \cdot \Lambda \cdot n_{eff}$$

(1)

The variation of λ_B ($\Delta \lambda_B$) depends on the variation of temperature, ΔT, and on mechanical strain, ε, as reported in

(2):

$$\frac{\Delta \lambda B}{\lambda B} = P_e \cdot \varepsilon + [P_e \cdot (\alpha_s - \alpha_f) + \zeta] \cdot \Delta T$$

(2)

being P_e the strain-optic coefficient, α_s and α_f [K^{-1}] the thermal expansion coefficient of the fiber bonding material and of fiber respectively, and ζ the thermal-optic coefficient [K^{-1}]. When the contribution of ε can be considered negligible, (2) can be reduced and simplified as follows:

$$\Delta \lambda_B = \alpha_T \cdot \Delta T$$

(3)

where α_T [nm·K^{-1}] is a global thermal coefficient that can

be assumed as the thermal sensitivity of the FBG.

- III.3 Development of a sensorized needle with FBG for monitoring temperature distribution and experimental validation during LTA on *ex vivo* swine liver

III.3.1 Theoretical background

In this experimental session [2], an FBG sensor was housed within a metallic needle to prevent the gratings from undesirable strains and to facilitate its insertion within the organ. Since the metallic needle increases the thermal inertia of the sensor, the influence of the presence of the needle on the response time of the probe has been experimentally assessed and compared to the transient response of a bare FBG sensor. Moreover, the eventual presence of measurement artifacts due to the direct absorption of laser light has been analyzed by measuring tissue temperature during laser treatment on porcine *ex vivo* livers by FBG sensors with and without needle cover.

III.3.2 Artifact amplitude and response time

In order to neglect strain due to respiratory movements, we housed the FBG in a metallic needle. On the other hand this solution may induce an overestimation of the temperature measurement, since metal absorbs laser radiation much more than the surrounding biological tissue. This phenomenon has been previously investigated on the use of thermocouple (which consists of two metallic wires) was carried out by several research groups

[2]. They showed that the temperature increase due to the direct absorption of laser light by the metallic wires of the thermocouple is almost instantaneous whereas a longer response time describes the increment actually caused by the surrounding tissue temperature increase. The marked difference between the response time allows estimating and correcting the artifact by subtracting the sudden temperature increase or decrease which happens when the laser is turned on or turned off, respectively. The correction is based on the model in (4), describing the trend of the measured temperature, T, during the tissue-cooling after the laser is turned off [2]:

$$T_{(t)} = A \cdot (1 - e^{-Bt}) + C \cdot t$$

(4)

where A, B and C are experimentally determined constants.

A technique to perform a more accurate correction of the artifact is based on the repetition of laser switching on and off in order to measure the amplitude of the artifact by averaging its value on several trials. A typical trend of the temperature measured during this kind of experiments is shown in figure 3.1.
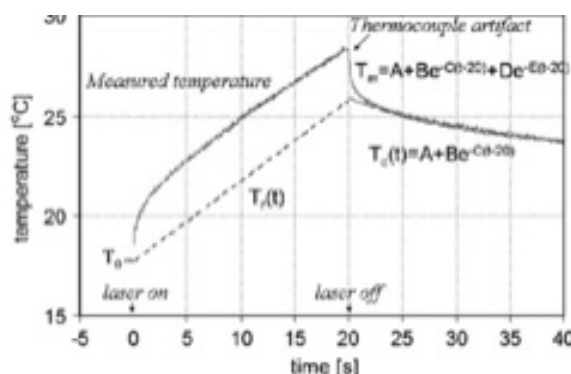
Figure 3.1. Trend of temperature measured by thermocouple during

laser ablation. It is evident the artifact due to the direct absorption of light by the thermocouple. Adapted from [3].

Regarding the dynamic response of the sensor, the presence of the metallic needle increases the sensor's response time due to the increase of thermal inertia. The analysis of the sensor's transient response has been carried out by calculating the response time, τ, using the error fraction function Γ(t), defined as [4]:

$$\Gamma_{(t)} = \frac{y(t) - y_\infty}{y(0) - y_\infty} = e^{-\frac{t}{\tau}}$$

(5)

where y(t), y(0) and y_∞ are the output values at the generic instant (t), at the step instant, and at the steady-state, respectively. A linear regression of the logarithm of $\Gamma_{(t)}$ allows calculating τ.

III.3.3 Experimental setup

To assess the temperature artifact the following experimental set up was used (Fig. 3.2.A): an *ex vivo* swine liver was housed within a polymeric mask, employed to accurately place and control relative distances between FBG sensors and quartz bare fiber applicator (core diameter of 300 μm). LA of *ex vivo* livers has been performed with Nd:YAG laser (wavelength of 1064 nm) in continuous-wave mode (Smart 1064, DEKA M.E.L.A. S.r.l., Florence, Italy), and laser power of 2 W. FBGs were interrogated by an Optical Spectrum Analyzer (Optical Sensing Interrogator, sm125, Micron Optics), and the spectrum was collected by a computer.

Two FBG sensors were used simultaneously: the first one was housed within a hollow metallic needle (1.1 mm of external diameter) and fixed by means of a thermal grease.

This solution was used to increase the thermal conductivity of the interface between fiber and needle; the second one was inserted within the tissue without any protection. Both FBGs have a sensitive length of 1 cm, and λ_B =1549 nm (Fig. 3.2.B).
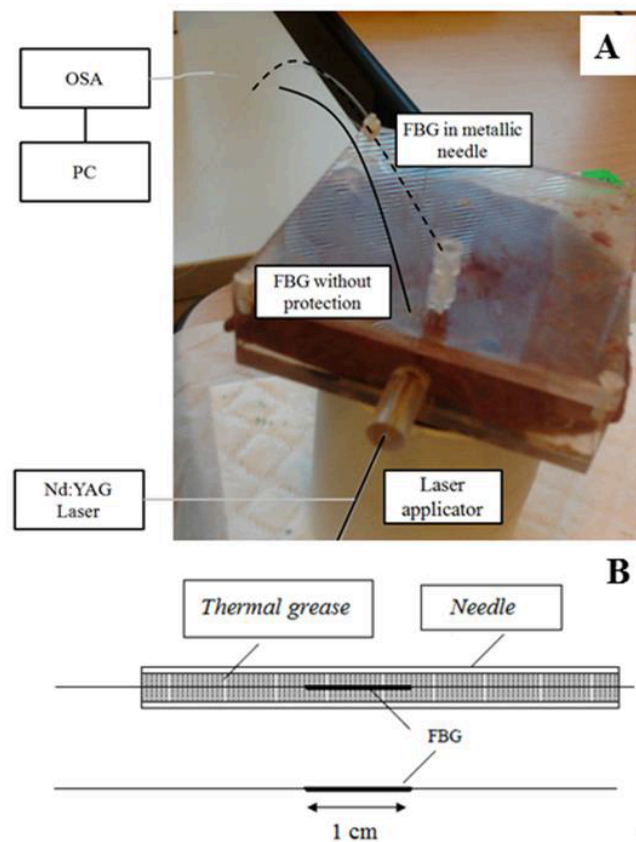
Fig. 3.2 A) *Ex vivo* liver undergoing Nd:YAG laser ablation placed in polymeric mask, housing quartz laser applicator and FBG sensors, with Optical Spectrum Analyzer and PC for data collection; B) FBG sensor in metallic needle, fixed by thermal grease, and FBG sensor without protection.

To assess the step response of the FBGs, with and without needle the experimental set up shown in figure 3.3 was used.

The experiments were performed in the traditional way: the two sensors under test were transferred from environmental temperature (i.e., 25±1 °C) into a vessel filled with warm water at constant temperature (i.e., ≈43±1 °C) equipped with a heating resistance. The temperature within the chamber was monitored by a thermocouple whose output was recorded by a multimeter.
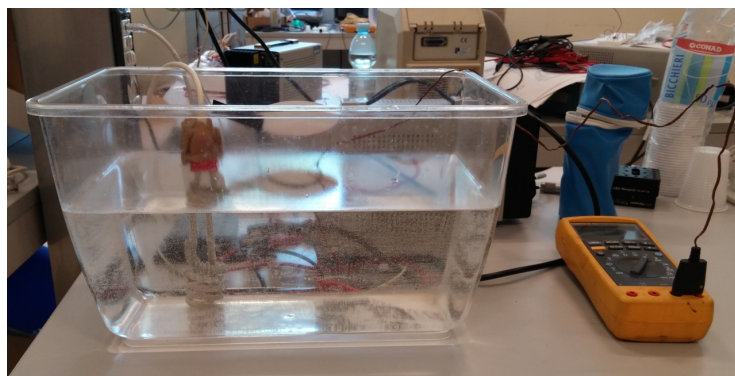
Fig. 3.3. Experimental setup used to estimate the response time of the FBGs. The vessel with warm water, the heating resistance, the multimeter and the thermocouple are shown.

III.3.4 Results and discussion

Assessment of artifacts is performed by irradiating liver with a series of 10 consecutive laser-on and laser-off: each laser-on lasted 20 s and, after the first laser-off, tissue temperature was left decreasing to the initial temperature (room temperature ranging from 20 °C to 25 °C), before to proceed with the next laser-on. The artifacts were also evaluated at different distances between FBGs and applicator, and the measurements were performed simultaneously by metallic protected and not-protected FBG, arranged in symmetrical configuration with respect to the laser applicator axis.

The configuration of the sensors is shown in Fig. 3.4.
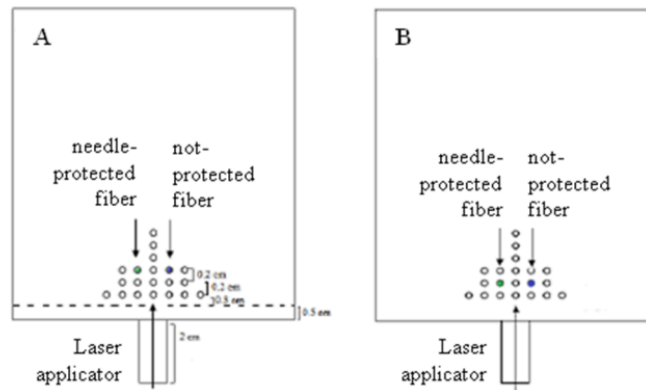
Fig. 3.4 Needle-protected and not-protected fibers at a distance of A) 6 mm from the laser applicator tip and B) 4 mm from the laser applicator tip.

Temperature measured by FBG housed in metallic needle was in each trial higher than the temperature measured by not-protected one: when FBGs were placed at a distance of 6 mm from the optical applicator, the maximum temperature difference (ΔT) monitored was about 10 °C (Fig. 3.5.A). During a single treatment (Fig. 3.5.B), the presence of artifacts was evaluated considering the difference between the temperature changes measured by the two FBGs in the period of about 2 s after both the laser-on (Fig. 3.5.C) and the laser-off.
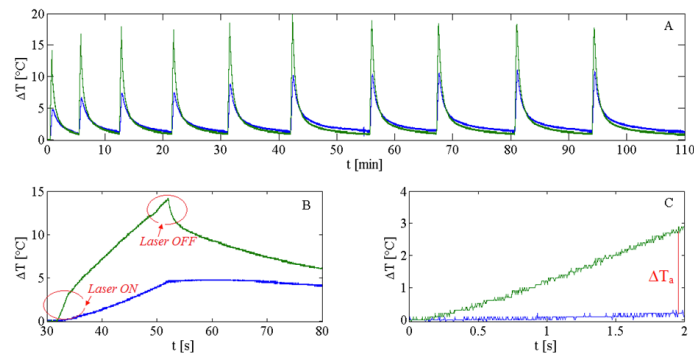
Fig. 3.5 A) Liver temperature trend during 10 consecutive laser-on and laser off, simultaneously measured by needle-protected (green line) and not-protected (blue line) FBGs at 6 mm from laser applicator; B) Zoom of one treatment; C) Evaluation of artifact after 2 s of laser-on.

Temperature measured by the FBG housed in the metallic needle was higher than the temperature measured by the not-protected one in each trial: when FBGs were placed at a distance of 6mm from the optical applicator, the maximum temperature difference (ΔT) monitored was about 10 °C (Fig. 3.5.A).

At a distance of 4 mm between needle-protected FBG and optical applicator tip, we measured $\Delta T_a = 4.4 \pm 0.7$°C, whereas at 6 mm the value of the artifact is $\Delta T_a = 2.0 \pm 0.4$°C. All the results are expressed as mean value ± expanded uncertainty; the expanded uncertainty has been calculated considering t-Student distribution, with a level of confidence of 95% and 19 degrees of freedom (the number of trials was 10 and for each trial we obtained two estimation of ΔT_a, the first one when the laser is turned on and the second one when the laser is turned off thus, the total number of samples for each configuration was 20) as recommended in [5].

Concerning the transient response, six measurements were

carried out in order to estimate the step response time (τ) of the developed sensor; considering (5), y(0) has been replaced with initial temperature value (i.e., environmental temperature), y(∞) with steady -state temperature value, and y(t) with temperature value at a generic instant t, respectively. Fig. 3.6 shows the experimental trend of the step responses of FBG without (τ_n) and FBG with (τ_c) needle obtained during a single trial and the constant time obtained during all the six experiments. $\Delta T(t)$ is the difference between the temperature at a generic t and initial temperature (25°C), whereas ΔT_{max} is the difference between the steady-state temperature and initial temperature.

As expected, the two configurations show different values of step response time: in particular, the sensors constituted by the FBG encapsulated within the needle is characterized by τ_c =140±14 ms, whereas the not-protected FBG shows a value of τ_n =40±4 ms. These values are obtained by considering a Student reference distribution (5 degrees of freedom and a level of confidence of 95%) [5]. The presence of metallic needle increases the response time of the sensor of more than three times, with respect to the configuration without needle.
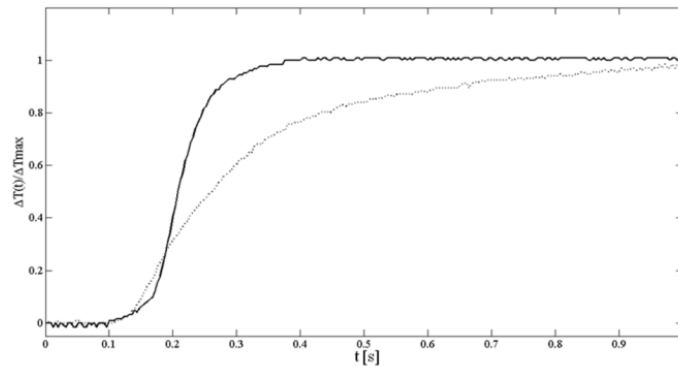
Fig. 3.6 Step response trend of the FBG with (dotted line) and without (continuous line) needle during an experimental trial. The constant times calculated using equations 1 and 2 for all the six trials are reported.

The results, in terms of both the artifact amplitude showed by protected needle at 4 mm and 6 mm from laser applicator and the step response time of the FBG in the two configurations, are summarized in Table 3.1.

Table 3.1. Artifacts cause by needle-protected FBG, and response time of needle-protected and not not-protected FBG.

Artifact amplitude [°C] mean value ± expanded uncertainty	
Distance of 4 mm	Distance of 6 mm
4.4±0.7	2.0±0.4
Response time [ms] mean value± expanded uncertainty	
Needle-protected FBG	Not-protected FBG
140±14	40±4

III.3.5 Conclusions

This study presents the design and evaluation of an FBG sensors encapsulated within a metallic needle to be employed in temperature monitoring during LA. This

solution aims at preventing the gratings from undesirable strains and to safely insert the sensor within the tissue. The experimental assessment of the artifact, induced in the proposed sensor, is performed on *ex vivo* liver. Moreover, response time of the sensor has been experimentally evaluated and compared to the one of a non-encapsulated FBG.

The comparison between the measurements performed by the encapsulated FBG and the non-encapsulated one, simultaneously used during LA, showed a temperature overestimation of about 4.4 °C when the distance between sensors and applicator tip is 4 mm, and a lower value at longer distance (i.e., 2 °C at 6 mm). As also previously discussed by Manns et al. [6], although artifacts affect the reliability of the measurement, they could be corrected through some mathematical strategies based on the modeling of temperature trend as function of time and distance between the sensor and the tip of the optical applicator.

Concerning the step response, the encapsulated FBG shows a response time of 140 ms, vs the value of 40 ms showed by not-protected one. However, the longer response time is still suitable for LA purposes.

The experimentally assessed characteristics make FBG encapsulated in metallic needle appropriate for temperature measurement during LA, and may allow overcoming the issue of respiratory movement artifacts on FBG output during in vivo trials. Moreover, the employment of a metallic needle allows facilitating the insertion of the sensor within the organ and avoids the risk of rupture of the fiber within the tissue making the measurement safer.

The major limitation of the study is that the trials were performed on healthy *ex vivo* swine livers. In fact, the substantial difference between the optical properties of the healthy liver and the tumor tissue strongly influences the artifact. As a consequence, the artifact should be different in the clinical scenario. Moreover, all the experiments have been performed at only one laser power value and employing only one laser which emits at 1064 nm; also these two parameters influence the artifact.

- III.4 Experimental validation of sensorized needle during MWA on *ex vivo* swine liver

Among percutaneous ablation techniques, the most recent development has been the use of MW energy, typically at 900 MHz-2.45 GHz, to increase the tumor temperature. Data focusing on the efficacy of MWA and on its effects in terms of tissue temperature distribution and amount of damaged volume lack because of the relative recent introduction of this method in the field of tumor treatment. In the present work [7] the effects of MWA on *ex vivo* porcine livers were simulated by finite element analysis method in terms of temperature increase and damaged volume. The simulations were validated by monitoring temperature by three custom made thermometric probes based on FBG sensors; these probes are three needles embedding four, three and one FBGs, respectively.

After the fabrication process, we calibrated the probes in a wide range of temperature (up to about 90 °C). Lastly, we inserted the probes within the *ex vivo* tissue undergoing MWA, in order to record its temperature in eight different

positions and to compare the experimental results with the simulations.

III.4.1 Theoretical background

Interaction between Microwave and biological tissue

The interaction of MW and biological tissue relies on dielectric hysteresis to produce heat [8]: at molecular level, the asymmetry of the distribution of positive and negative electric charges (either intrinsic or induced by an external electromagnetic field) involves the formation of electric dipoles. These dipoles maintain alignment when an electromagnetic field is applied from the outside. The application of an alternating field produces the "dielectric heating" in biological tissue: the electric dipoles rotate continuously, producing friction which leads to the conversion of the energy field into heat within tissue. The dielectric heating has high efficiency in the range of MW frequencies and in biological tissues with a high percentage of water (as in solid organs and tumors). The amount of absorbed energy per unit of time and volume Q [W/m^3] is computed from the electric field, E [V/m], in tissue:

$$Q = \frac{1}{2}\sigma|E^2|$$

(1)

where σ is the effective conductivity [S/m] [9].

The knowledge of Q and the use of Pennes' equation [10] contribute to the prediction of temperature map within the biological tissue by solving the following equation [11]:

$$\rho c \frac{\partial T}{\partial t} = \nabla \cdot k\nabla T + Q + Q_{bl} + Q_{met}$$

(2)

where ρ [kg/m^3] is the tissue density, c [J/kg·K] is the

specific heat capacity, k [W/m·K] is the thermal conductivity, T [K] is the tissue temperature, Q_{bl} [W/m^3] is the heat loss due to blood perfusion, and Q_{met} [W/m^3] is the metabolic heat generation. Q_{bl} and Q_{met} are considered negligible in case of examination of *ex vivo* organs.

Lastly, the degree of tissue injury Ω can be modeled with a first-order rate process described by the Arrhenius equation [12]:

$$\Omega(\tau) = \int_0^\tau A \, exp(-\frac{dE}{RT}) dt$$

(3)

where A [s^{-1}] is the frequency factor, dE [J/mol] is the activation energy for irreversible damage reaction, and R [J/mol·K] is the universal gas constant. The relationship below expresses the fraction of necrotic tissue, θ_d:

$$\theta_d = 1 - exp\,(-\Omega)$$

(4)

III.4.2 Numerical simulations: geometry and MWA settings

The theoretical model was developed to predict the temperature distribution and the necrotic tissue within the tissue around the antenna at settings largely employed in clinics (power of 100 W and treatment time of 4 minutes). The manufacturer recommends these settings to produce a lesion with a maximum diameter of 3 cm [13].

The simulations included the geometrical structures of the antenna and liver domain. The antenna consists of a thin coaxial cable (4 mm of diameter, inserted within the tissue for 6 cm) and it is enclosed in a sleeve made of poly-tetrafluoroethylene (PTFE). Moreover, it operates at 2.45 GHz, which is a frequency widely used in the MWA

therapy. The geometry takes advantage of the problem's rotational symmetry, which allows modeling in 2D using cylindrical coordinates. We used a mesh based on triangular components of sizes ranging from 3 mm (far from the antenna) to 0.024 mm (close to the antenna). Simulations were carried out with the FEM (finite element method) analysis, in Comsol Multiphysics 4.4 environment.

The theoretical model was based on:

- Pennes' equation (2) in order to give a prediction of temperature distribution in the liver undergoing to ablation treatment; in this study we considered negligible the terms Qbl and Qmet (*ex vivo* liver setting);

- external Q to simulate the effects of the MWs for a power of 100 W and a time of 4 minutes on tissue;

- simulations started with an initial liver temperature of 20°C (environmental temperature);

- the damaged volume was computed by the Arrhenius model (3 and 4).

We used the physical parameters of the liver tissue in (1, 2, and 3) as [14].

III.4.3 Experimental set-up

Two sets of experiments have been performed: the first one was dedicated to the static calibration of the eight FBGs embedded within the three probes; the second one was related to the measurement of temperature distribution during MWA of *ex vivo* porcine livers.

Static calibration of FBGs sensors

The static calibration of the sensorized needle was performed to obtain the thermal sensitivity of the sensors

(3), as reported in [15]. The three sensorized needles were placed within an oven (PN120 Carbolite®), whose temperature was monitored by two reference temperature sensors (Silicon bandgap temperature sensor EL-USB-2-LCD, Lascar Electronics®). The oven temperature increased from 21 °C to 90 °C. The data ($\Delta\lambda_B$) obtained from the FBGs were acquired by an Optical Spectrum Analyzer (Optical Sensing Interrogator si425 Micron Optics®) and synchronized with the temperature measured by the reference sensors.

Then the recorded $\Delta\lambda_B$ and ΔT were fit by a linear model. The slope of the best fitting line was considered the thermal sensitivity of the FBGs.

Temperature map within *ex vivo* porcine livers

Experiments were performed on four healthy *ex vivo* porcine livers at environmental temperature of 20 ± 2°C, which corresponds to tissue temperature measured before starting the treatment. The experimental set-up consisted of four elements: a MW generator, a cooled-shaft antenna, the three sensorized needles, and an optical spectrum analyzer which record the FBGs output. The 2.45 GHz generator (Emprint^{TM} Ablation System, Covidien, USA) includes a new technology (i.e., Thermosphere®) and it was connected to the cooled-shaft antenna (15 cm of length). The ablations have been performed at 100 W for 4 minutes.

The FBGs measured temperature in eight different positions within the liver. The distance between the eight FBGs (embedded in the three 16G needles) and the antenna was controlled by the custom made PTFE mask. A schematic representation of the relative positions

between the FBGs and the antenna is shown in Fig. 3.7. The first sensorized needle (A) was equipped with one FBG at 1cm away from needle's tip; the second sensorized needle (B) embedded four FBGs located at 1cm, 1.2cm, 1.4cm and 4.4cm away from the tip, respectively; the third sensorized needle (C) embedded three FBGs at 1cm, 1.2cm and 1.4cm away from the tip, respectively. An optical spectrum analyzer (Optical Sensing Interrogator, Si425, Micron Optics) is used to record data from FBGs with a sample frequency of 250 Hz.

After each MWA, the liver was sectioned to estimate the volume of damaged tissue.

Data analysis was performed in Matlab® environment.
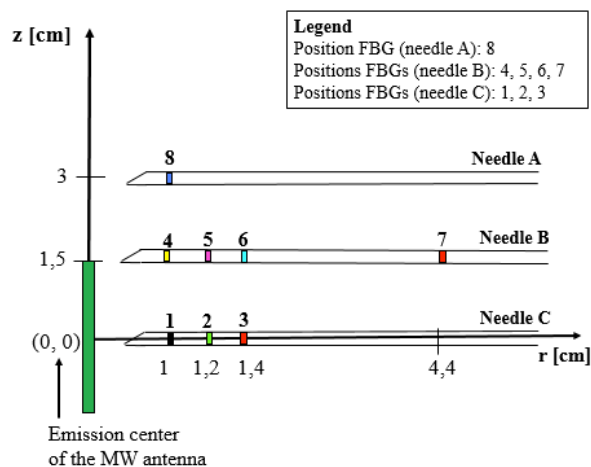
Fig. 3.7 Positioning of the eight FBGs sensors in the needles, placed within the liver tissue.

III.4.4 Results

Static calibration of the sensor

The temperature trends in correspondence of the eight FBGs positions are extracted from the ones provided by FEM in the whole domain. Then, the temperatures at the

end of MWA (after 4 minutes of simulation) are selected and shown in Fig. 3.8 (black bars). The lower the distance from the emission center of the antenna, the higher the temperature at the end of the procedure. The highest increment is obtained 1 cm from the emission center of the antenna (~50°C); it was negligible in positions 7 and 8 (<0.5°C). Table II reported temperature values achieved in the eight positions -corresponding to the position of the FBGs- after four minutes of MWA, which corresponds to the end of the treatment. The coordinates of the eight positions (i.e., r and z) are also reported.
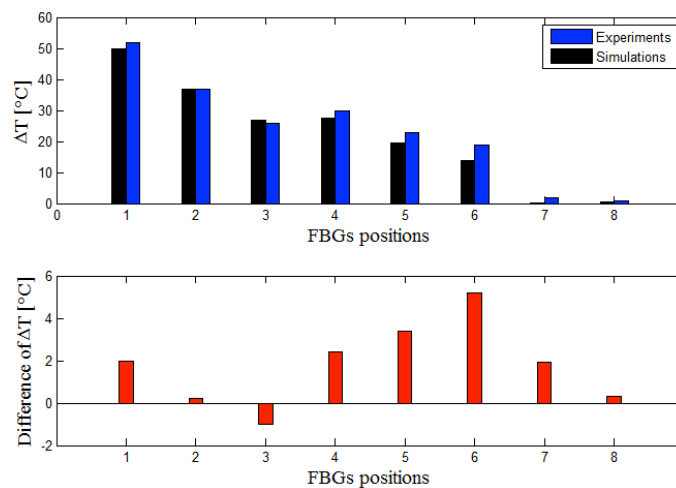
Fig. 3.8 Temperature values obtained at the end of the MWA (100 W, 4 minutes) in the eight FBGs positions. Black bars: theoretical data; blue bars: experimental data; red bars: differences between experimental and simulated temperature at the end of the treatment.

Table 3.2. Simulated and experimental temperature increment achieved in liver tissue after 4 minutes of MWA. The distances from the emission center of the antenna are also reported.

Position	r [cm]	z [cm]	Simulated ΔT [°C]	Experimental ΔT [°C]
FBG 1	1	0	50	52
FBG 2	1.2	0	36.8	37
FBG 3	1.4	0	27	26
FBG 4	1	1.5	27.6	30
FBG 5	1.2	1.5	19.6	23
FBG 6	1.4	1.5	13.8	19
FBG 7	4.4	1.5	0.06	2
FBG 8	1	3	0.4	0.7

Lethal isotherms were considered where temperature was higher than 60°C within the liver at the end of the ablation. Therefore, lethal isotherms had to fulfill the condition $\Delta T > 40°C$, because the initial temperature was about 20°C (it corresponded to the environmental temperature). Numerical simulations showed that the necrotic volume, calculated considering an elliptic shaped damage, was about 12.5 cm^3 (see Fig. 3.9).
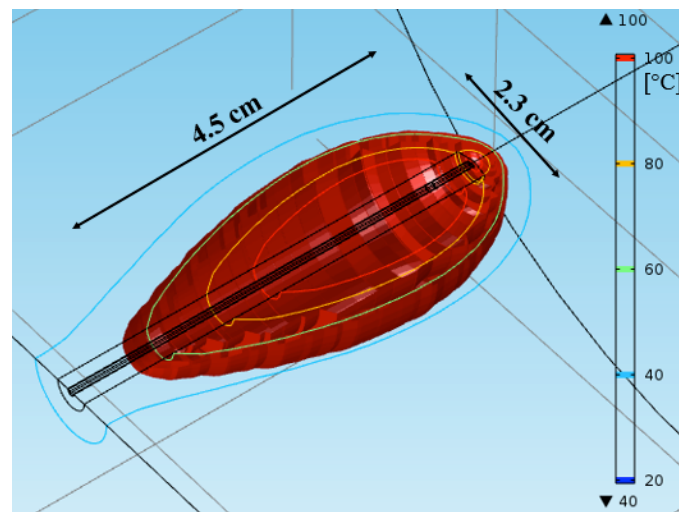
Fig. 3.9 Three-dimensional representation of the damaged volume (considering all the tissue at temperature higher than 60°C at the end of the MWA). Other isotherms (100 °C, 80 °C, 60 °C, and 40 °C) are also showed by continuous lines.

Results during MWA

The static calibration of the sensors embedded within the three probes showed a good linearity. The linearity was confirmed by the high values of the correlation coefficient ($R^2 > 0.99$) for all the eight calibration curves. The thermal sensitivity of the sensors –considered equal to the slope of the best fitting lines–ranged from 0.01 nm·°C^{-1} to 0.02 nm·°C^{-1}.

The lowest value is equivalent to the one of the nude FBG sensor (as reported by the manufacturer). This aspect confirmed the lack of cohesion between FBGs and the needle, therefore the change of $\Delta\lambda_B$ was related by temperature variation and not by thermal expansion of the needle. The FBGs with high sensitivity values (i.e., about 0.02 nm·°C^{-1}) were fixed to the needle by an epoxy resin. In this case the bond with the metallic needle was strong and the contribution of the thermal expansion of the

needle was not negligible on the $\Delta\lambda_B$.

Temperature measured at the end of MWA by the eight FBGs embedded in the three needle on *ex vivo* porcine livers, were reported in Fig. 3.8 (blue bars). Results show that the shorter the distance from the emission center of the antenna, the higher the temperature. Moreover, the experimental temperature agreed with those obtained in the simulations: for instance the increment in position 1 was 52 °C (experimental) vs 50 °C (simulated).

In order to easily compare experimental ΔT and simulated ones, Fig. 3.8 also shows their differences (red bars). Moreover, Table II also reported experimental temperature values achieved in liver tissue after 4 minutes of MWA in the eight FBGs positions.

Finally, we measured the volume of the damage tissue obtained at the end of the MWA. An example of the damage experienced by one of the four treated livers is shown in Fig. 3.10. The volume estimated by considering a damage with an elliptic shape was about 12.4 cm^3.
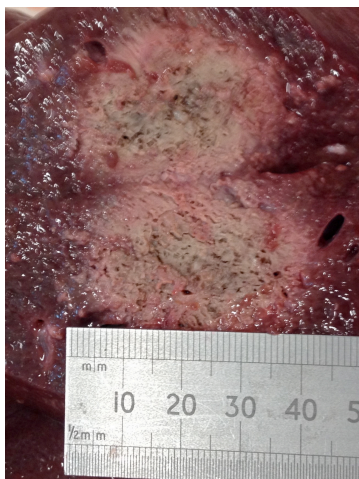

Fig. 3.10. Section of the damage tissue at the end of MWA at 100 W for 4 minutes experienced by one of the four *ex vivo* porcine livers.

III.4.5 Discussion and conclusions

Percutaneous thermal ablation is a targeted-destruction of tumoral tissue without surgery. It induces tissue necrosis by means of an increment (by LA, MWA, RFA) or a decrease (by cryoablation) of tissue temperature. Among all the available thermal treatments, literature regarding the effects of MWA is the poorest, because of the relative recent introduction of this technique in the field of cancer ablation. MWA allows generating high temperatures in a reduced treatment time; moreover, it minimize the exposure to vascular-mediated "heat-sink effect" [16].

In this work we simulated the effects of MWA on *ex vivo* liver in order to reconstruct and estimate the tissue temperature distribution and the tissue damaged volume. The simulations were performed considering the geometry of a novel commercial MW antenna. Then, we implemented the Pennes' equation to simulate the MWA effects on *ex vivo* porcine liver at a setting employed in clinics (i.e., 100 W for 4 minutes).

The model was experimentally validated. In the experiments, the temperature was measured in the eight positions by FBGs inserted in three custom made thermometric probes at fixed distances from the antenna. Temperature was measured in the axial plane in eight positions along two different directions (short and long axes of the necrotic volume).

This is an important step forward with respect on our previous study where temperatures were measured only at five positions along the short axis of the necrotic volume [17]. Therefore, our multiple temperature measurements represented the first step to develop a temperature

distribution around antenna.

It is crucial to deeply investigate the effects of MWA on tissue considering that only few studies are reported in literature [17, 18] and considering the differences in the interaction with the biological tissue between laser light and MW [19]. In MWA the energy forces dipoles to continuously realign with an applied electromagnetic field, producing heat. In LA, the light is absorbed by tissues, then it is converted into heat.

There exist two main limitations of the proposed study: i) experiments were performed on healthy *ex vivo* porcine livers, therefore the vascular impairment due to "heat-sink effect" was underestimated; and ii) the ablations were performed at room temperature ($\approx$ 20 °C), which was inferior to starting 37°C temperature *in vivo* systems.

The simulated temperature increments around the antenna agreed with experimental ones considering the eight different positions (the mean difference was $\approx$ 1.8°C). Moreover, we compared the necrotic volume predicted by Arrhenius equation with the one experienced by the liver underwent MWA. Also predicted and experimental volumes showed good agreement (12.5 cm^3 and 12.4 cm^3, respectively). The main difference between predicted necrotic volume and experimental one is related to their shape. The simulations provided an elliptic damaged volume, whereas both the experimental study [17] and the manufacturer suggested that the damaged tissue should be almost spherical-shaped. A possible cause of this aspect could be the fact that the model did not take into account the three levels of control (i.e., field control, thermal control, and wave-length control) of the 2.45 GHz system, which uses the new technology Thermosphere® [14].

In conclusion, our study developed a model able to predict temperature distribution and damaged volume around antenna during MWA.

- III.5 Experimental validation of sensorized needle during RFA on *in vivo* swine liver

III.5.1 Introduction

Liver RFA is usually performed under US guidance because CT or MR temperature monitoring is not feasible for real-time temperature assessment. The state of the art presents many studies regarding the use of thermocouples for thermal treatment monitoring, in dedicated probe [20], or embedded in the electrode, for the one-point measure of temperature [21]. Recently, also fiber optic sensors are gaining interest in the field of temperature measurement during thermal treatments.

The need to perform multi-punctual and distributed measurements has motivated the investigation of FBGs sensors, in several configurations. Among many advantages, an array of several FBGs can be placed with one single optical fiber, and permits to monitor temperature in different points simultaneously. Moreover, they are small (e.g., 1 mm of length), flexible, CT and MR compatible, and do not cause any measurement artifact due to direct absorption of source energy [21].

Aiming to ease the insertion of thin and flexible fibers housing FBGs within the organs, solutions for encapsulation are well accepted.

In this experimental session [22] the aim was to assess the feasibility of the previously described needle-like probe

during liver RFA in a *in vivo* animal model.

III.5.2 Radiofrequency ablation: experiments and settings

A 6 months healthy female pig has been adopted as animal model in a veterinary clinical lab. The choice of this model is related to the similar anatomical features between the porcine liver and the human one. After sedation of the animal, a US-guided RFA procedure has been performed on healthy liver parenchyma in free breath conditions; the RFA ablation was carried out on the right lobe (Fig. 3.11). The US-guidance was conducted with a convex probe (1-8 MHz, ultrasound equipment: MyLab Gold 30, ESAOTE®, Italy).
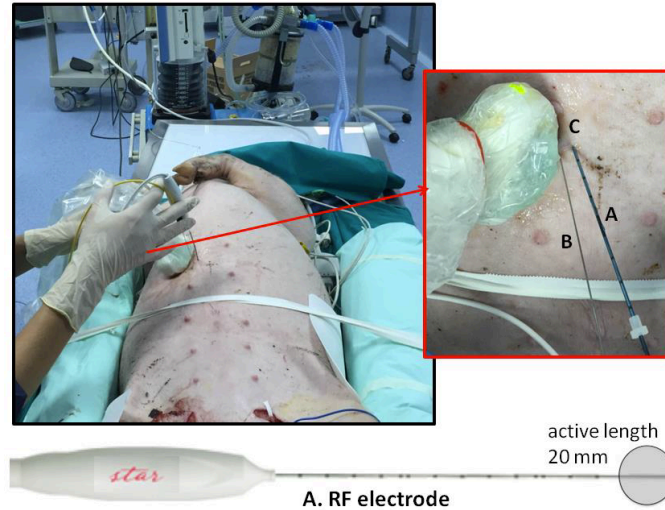
Fig. 3.11 US-guided RFA on *in vivo* pig liver: A) RF electrode, B) needle-like probe and C) US probe.

The RFA equipment was composed of an RF generator (VIVA RF Generator, STARMed ®, Korea) and a needle probe (Star Electrode Fixed type, STARMed ®, Korea);

the RF electrode measured 17 Gauge, had length of 150 mm and presented an active length of 20 mm, able to perform a spherical shaped ablation area with a diameter of 20 mm backward from the tip (Fig. 3.11). A coolant circulation system maintained a suitable impedance at the surface of the electrode.

After positioning the RFA probe into the liver parenchyma, the needle-like probe was inserted at 11 mm of distance from the RFA needle tip, in order to measure the temperature distribution into the surrounding tissues. Fig. 3.12 provides US images of placement of RF electrode and needle-like probe into the liver.

The ablation process lasted 350 s with a power of 80 W.

Fig. 3.12 US image of the placement of the needle-like probe housing the three FBGs anf the RF electrode, placed at relative distance of 11 mm, inside the pig liver.

III.5.3 Results

Before starting the RFA, the FBGs response due to the breathing movements of the animal has been recorded.

This output is expressed as temperature error, i.e., the error in the measurement of the temperature due to strain. The breathing pattern has been monitored for 30 s before RFA, as shown in Fig. 3.13:

Fig. 3.13. Breathing movements error experienced by the three FBGs embedded in the needle-like probe before starting RFA on pig liver.

At systemic liver temperature, the FBGs experienced a slight temperature change due to the movements of the liver induced by breathing. The maximum error, defined as the absolute value of maximum increment with respect to 0 °C, is recorded by FBG3 (2.9 °C), that is the FBG closest to the needle-tip, while the other two FBGs are less affected (2.1°C).

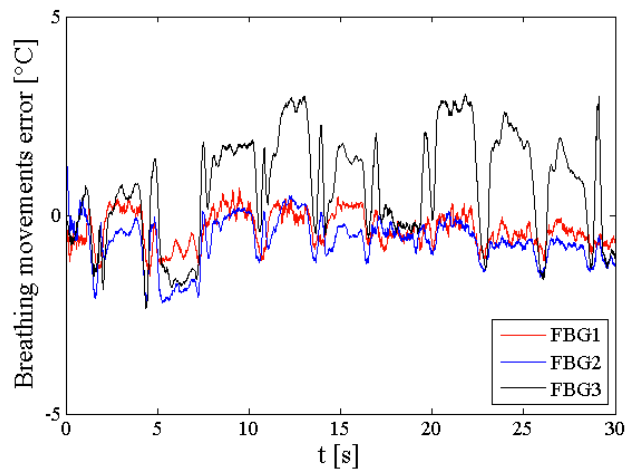Afterwards, the RFA is performed according to settings previously listed, and the temporal temperature evolution measured by the three FBGs is shown in Fig. 3.14:
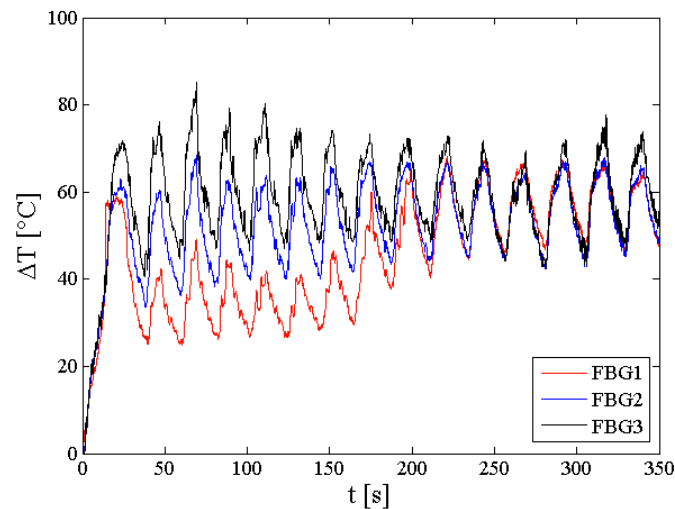
Fig. 3.14 Breathing movements error experienced by the three FBGs embedded in the needle-like probe during RFA on pig.

After a short time of overall temperature increase (from 0 s to 30 s), the FBGs experieced a regular change of T (consecutive decrements and increments) due to the modality of the RF energy delivering, i.e., the power roll-off. Till the half RFA (around 160 s), the three FBGs measured different ΔT, due to their different distance to the active part of the RFA needle (the FBG3 is the closest to RFA needle, followed by the FBG2 and FBG1). FBG3 measured ΔT ranging from about 48 °C to 79 °C; FBG2 experienced ΔT from about 40 °C to 63 °C; FBG1 provided ΔT between about 30 °C and 45 °C. The second part of the treatment is characterized by values of ΔT very close for the three FBGs, ranging from about 44 °C to 70 °C (with the exception of the last two peaks, where FBG3 measures about 8 °C more than the remainig ones).

III.5.4 Discussion and conclusions

The real time monitoring of tissue temperature during

ablative procedures is crucial to assess the performances of the treatment. Usually, studies are performed on *in vitro* or *ex vivo* tissues, in which several physiological conditions, like blood perfusion, metabolic heat generation, cannot be taken into account.

The novelty of our work is the first employment of needle-like probe based on FBGs array in *in vivo* animal model undergoing RFA. This measurement system allows monitoring the tissue temperature at three different locations from the RFA electrode, in order to obtain information about the temperature distribution, as sensors are placed in correspondence of different isothermal lines. In the first part of the RFA (t<160 s), the three FBGs provided different temperature values, because of their relative distance from the antenna active part. In the second part (t>200 s), the FBGs experienced mostly the same ΔT, meaning that in their positions the liver underwent the same thermal damage.

It is worth noting the effect of power roll-off strategy on the temperature: the ΔT is forced to change between 44 °C and 70 °C (under the hypothesis that liver initial T is 37 °C, the actual liver temperature changes between 81 °C and 107 °C) in the last part of the ablation along the region monitored by the three FBGs.

The maximum error induced by the liver movements of the pigs due to breathing is experienced by the FBG3, the closest to the needle tip, and has a peak-to-peak value of about 3 °C. This value is acceptable for the application, where an accuracy of about 2 °C is satisfactory to achieve a controlled and safe tissue ablation [23]. Moreover, considering that in current practice the ablation procedures are usually performed without accurate temperature

monitoring, this result is reasonable.

The promising results of this study open interesting perspectives for the novel needle-like probe in *in vivo* trials, even on humans. Further trials could be performed to evaluate the tissue contraction during heating, and efforts may be made to improve the performances and enhance the features of the probe, e.g., by embedding more FBGs (up to 10 gratings can be easily embedded in the array), by using a needle compatible with CT and/or MRI-guided procedures, or, by encapsulating the array on the RFA electrode.

- III.6 Bibliography

1. S. Silvestri and E. Schena, "Optical-Fiber Measurement Systems for Medical Applications," in Optoelectronics- Devices and Applications, Padmanabhan Predeep, InTech, 2011, pp. 205-224.

2. Schena E, Saccomandi P, Massaroni C, Quattrocchi V, Frauenfelder G, Giurazza F, Caponero MA, Polimadei A, Silvestri S. Temperature monitoring during laser ablation by FBG sensors encapsulated within a metallic needle: experiment on healthy swine tissue. 10th International Symposium on Medical Measurement and Application, Turin, Italy 2015

3. Van Nimwegen, S.A., L'eplattenier, H.F., Rem, A.I., Van Der Lugt, J.J. and Kirpensteijn, J., 2008. Nd: YAG surgical laser effects in canine prostate tissue: temperature and damage distribution. Physics in medicine and biology, 54(1), p.29.

4. Beckwith, T.G., Marangoni, R.D. and Lienhard, J.H., 2009. Mechanical measurements. Pearson.

5. Evaluation of measurement data—Guide to the expression of uncertainty in measurement, JCGM 100, 2008.

6. F. Manns, P. J. Milne, X. Gonzalez-Chirre, D. B. Denham, J. M. Parel and D. S. Robinson, "In situ temperature measurements with thermocouple probes during laser interstitial thermotherapy (LITT): quantification and correction of a measurement artifact," Lasers Med Sci, vol. 23, pp. 94 - 103, 1998.

7. Villani S, Saccomandi P, Massaroni C, Schena E, Cazzato RL, Giurazza F, Frauenfelder G. Experimental validation of MWA effects on biological tissue by sensorized needles based on FBG technology. 11th IEEE International Symposium on Medical Measurements and Applications (MeMeA), 2016. 10.1109/MeMeA.2016.7533804

8. C.J. Simon, D.E. Dupuy, and W.W. Mayo-Smith, "Microwave Ablation: Principles and Applications," RadioGraphics, vol. 25, pp. 69- 83, 2005.

9. C.L. Brace, "Microwave Tissue Ablation: Biophysics, Technology and Applications," Crit. Rev. Biomed. Eng., vol. 38(1), pp. 65-78, 2010.

10. Zhen Ji, and C.L. Brace, "Expanded modeling of temperaturedependent dielectric properties for microwave thermal ablation," Phys. Med. Biol., vol. 56(16), pp. 5249–5264, 2011.

11. A.J. Welch, and M.J.C. van Gemert, Optical-thermal response of

laser irradiated tissue, 2nd Ed., New York, NY: Springer, 2011.

12. A.D. Kersey, M.A. Davis, H.J. Patrick, M. LeBlanc, and K.P. Koo, "Fiber Grating Sensors," J. lightwave technol., vol. 15(8), pp. 1442- 1463, 1997.

13. D.A. Christensen. "A new nonperturbing temperature probe using semiconductor band edge shift," J. Bioeng., vol. 1, pp. 541-545, 1977.

14. A.M. Ierardi, A. Mangano, C. Floridi, A. Biondi, E. Duka, N. Lucchina, G.D. Lianos, and G. Carrafiello, "A new system of microwave ablation at 2450 MHz: preliminary experience," Updat. Surg., vol. 67(1), pp. 39–45, 2015.

15. P. Prakash, "Theoretical Modeling for Hepatic Microwave Ablation," Open Biomed. Eng. J., vol. 4, pp. 27-38, 2010.

16. D. Polito, M.A. Caponero, A. Polimadei, P. Saccomandi, C. Massaroni, S. Silvestri, and E. Schena, "A needlelike probe for temperature monitoring during laser ablation based on fiber Bragg grating: Manufacturing and characterization," J Med Devices, vol. 9(4), Article number 041006, 2015

17. C.L. Brace, "Microwave ablation technology: what every user should know," Curr. Probl. Diagn. Radiol., vol. 38(2), pp. 61-67, 2009.

18. P. Saccomandi, E. Schena, C. Massaroni, Y. Fong, R.F. Grasso, F. Giurazza, B. Beomonte Zobel, X. Buy, J. Palussiere, and R.L. Cazzato, "Temperature monitoring during microwave ablation in ex vivo porcine livers," Eur. J. Surg. Oncol., vol. 41(12), pp. 1699-1705, 2015.

19. Y. Sun, Y. Wang, X. Ni, Y. Gao, Q. Shao, L. Liu, and P. Liang, "Comparison of ablation zone between 915-and 2,450-MHz cooledshaft microwave antenna: results in in vivo porcine livers," Am. J. Roentgenol., vol. 192(2), pp. 511-514, 2009.

20. H. Ishizaka, A. Shiraishi, S. Awata, A. Shimizu, S. Hirasawa, "Development of a fine thermocouple-needle system for real-time feedback of thermal tumour ablation margin," Brit. J. Radiol., vol. 84, pp. 1139-1141, 2011.

21. E. Schena, L. Majocchi, "Assessment of temperature measurement error and its correction during Nd: YAG laser ablation in porcine pancreas," Int. J. Hyperthermia, vol. 30, pp. 328-334.

22. Saccomandi P, Frauenfelder G, Massaroni C, Caponero MA, Polimadei A, Taffoni F, Di Matteo FM, Costamagna G, Giurazza F and Schena E. Temperature monitoring during radiofrequency

ablation of liver: in vivo trials. Conf Proc IEEE Eng Med Biol Soc.
2016 Aug;2016

23. L. Frich, "Non-invasive thermometry for monitoring hepatic
radiofrequency ablation," Minim. Invasiv. Ther. Allied Technol., vol.
15, pp. 18-25, 2006.

Chapter IV

Temperature monitoring based on Computed Tomography imaging

The potential of CT for non-invasive temperature measurement was pointed out by different authors since the late 1970s: it was considered useful in local tumour ablation [1]. However, at that time the repeatability of quantitative CT number measurements was not guaranteed, hampering the use of this method. Modern CT scanners provide fairly stable CT numbers, thus, this kind of research has been recently restarted with the aim to make a relevant step forward to the employment of CT thermometry.

The use of CT thermometry during hyperthermal treatment involves strict requirements, among others: spatial resolution of 1-2 mm, acquisition time shorter than 10-30 s; and temperature accuracy of 1-2 °C [2].

Pandeya *et al.* met the first criterion during *ex vivo* experiments on porcine liver [3], Weiss *et al.* met the second one [4]. On the other hand, further studies are needed to reach the third goal, for instance Bruners *et al.* stated that a temperature discrimination of 3-5 °C could be obtained [5].

Lastly, limiting patients' exposure is crucial in the use of CT thermometry, and both noise and patient dose are dependent on exposition parameters (i.e., mAs and kVp). For this reason the analysis of the influence of scan parameters on CT number measurements is mandatory to establish the right trade-off between patient exposition

levels and measurement precision. In this analysis, the mostly palliative character of thermal treatments in oncology patient with limited life expectancy needs to be considered.

The experimental sessions have evaluated the influence of ROI and CT settings on metrological properties for temperature monitoring during thermal procedure. Furthermore I conducted *ex vivo* sessions on swine livers to validate CT thermometry and monitor tissue vaporization during LTA and MWA.

- IV.1 Feasibility assessment of CT-based thermometry for temperature monitoring during thermal procedure: influence of region of interest (ROI) size and scan setting on metrological properties

The aim of this experimental session [6] is twofold: to assess the influence of CT scan settings (i.e., kVp and mAs) and of ROI size on the performances of CT thermometry; and to investigate the feasibility of CT thermometry to offer a good compromise between temperature precision and spatial detail, which meets the requirements of thermal treatment.

IV.1.1 Experimental setup

The study was conducted on a calibration water-equivalent phantom (fig. 4.1.A). The phantom was scanned by a multidetector CT scanner (Somatom Sensation 64-slices, Siemens, Germany) in sequential acquisition mode

(pitch=0.9 and 2 Hz rotation frequency). CT images were reconstructed with a slice thickness of 2 mm, applying a B30f convolution kernel and a 512x512 reconstruction matrix. The phantom was inserted in the CT room eight hours before the scan session, in order to reach the thermal equilibrium with the surrounding environment (23.3±0.2°C). The influence of control panel exposure parameters on CT number measurements, hence on temperature precision and spatial resolution, was investigated using nine different combinations of kVp and mAs (fig. 4.1.B).
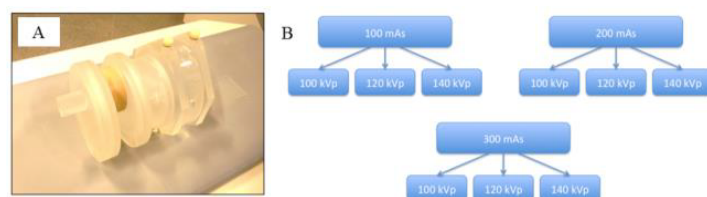
Fig. 4.1. A) Siemens CT Quality Phantom; B) Combinations of kVp and mAs for images acquisition.

After raw data acquisition and reconstruction, images were converted and processed in Matlab® environment: the transformation was implemented by SPM8 (Statistical Parametric Mapping), a Matlab® software package designed for the analysis of image data sequences. A statistical analysis was conducted on the ROIs selected; from the ROIs, area-averaged CT number, CT_{mean}, standard deviation σ_{CT} and uncertainty δ_{CT} were calculated. The values of δ_{CT} were calculated as recommended in [7]:

$$\delta_{CT} \approx k \cdot \frac{\sigma_{CT}}{\sqrt{N_p}}$$

(1)

Where N_p is the number of pixels within the ROI, and k is the coverage factor, calculated considering a level of confidence of 95%.

Referring to the linear relationship between CT number and temperature, and to the law of propagation of uncertainty [7], δ_T was estimated as follows:

$$\delta_T \approx \frac{\delta_{CT}}{k_T}$$

(2)

Where k_T is the thermal sensitivity of the water-equivalent phantom under investigation, whose value was experimentally assessed for each scan configuration.

IV.1.2 Results

The phantom was scanned at temperatures ranging from 18 °C up to 60 °C. Phantom temperature was monitored by a K-type thermocouple, connected to a 4-channel data acquisition system (FX100, Yokogawa). In each procedure, temperature was measured before and after the scan. The temperature difference between the measurements performed before and at the end of the procedure was always lower than 0.2 °C, hence can be considered constant during the whole protocol.

Linear regression analysis was performed between the averaged CT number and the phantom temperature, in order to obtain the k_T. CT number and phantom temperature showed an inverse relationship. Data show that k_T is almost independent from ROI size and scan settings, since it varies in a narrow range of values (from -0.37 HU·°C^{-1} to -0.34 HU·°C^{-1}). Table 4.1 shows the values of k_T at the nine scan settings and using a medium-large ROI size (fig. 4.3.A).

Table 4.1: Results of the regression analysis: thermal sensitivity, correlation coefficient and statistical significance.

Scan configurations [kVp - mAs]	k_T [HU·$^\circ$C^{-1}]	R^2	ρ
100 – 100	-0.36±0.15	0.99	< 0.05
120 – 100	-0.35±0.08	0.99	< 0.05
140 – 100	-0.36±0.04	0.99	< 0.05
100 – 200	-0.36±0.07	0.99	< 0.05
120 – 200	-0.37±0.06	0.99	< 0.05
140 – 200	-0.34±0.05	0.99	< 0.05
100 – 300	-0.34±0.12	0.98	< 0.05
120 – 300	-0.36±0.09	0.98	< 0.05
140 – 300	-0.35±0.06	0.99	< 0.05

The high correlation coefficient and the significance of the regression analysis confirm the good agreement between the experimental data and the linear model used to fit the data.

Regarding the precision and the spatial resolution, the ROI size was the first influencing factor investigated. In many applications of temperature mapping, such thermal therapies, the scanner would detect small density changes to ideally obtain a punctual temperature measurement: this is possible selecting on CT images very small ROIs. For the same scan conditions, a comparative analysis between four different sized ROIs, placed centrally within the cross-section of the cylindrical phantom, was made (fig. 4.2.A). The temperature uncertainty dependence on ROI size was described with a decreasing power model (fig. 4.2.B), where A indicates the area of the ROI selected.

$$\delta_T \approx a \cdot A^{0.5}$$

(3)

The theoretical basis of this model can be found in the estimation of uncertainty and in the law of propagation of uncertainty [7], being A and N_p directly proportional.

Therefore, the model shows that punctual temperature mapping and measurement precision work against each other: a better spatial resolution can only be achieved by a simultaneous degradation in temperature measurement precision and viceversa, confirming Fallone's results [8]. The second part of the analysis was conducted on images coming from the nine different combinations of kVp and mAs (figure 1.B), for the same ROI size. The two exposition parameters influence both the image noise and the patient dose; therefore this analysis might be useful to establish the right trade-off between patient exposition levels and measurement precision. In fact measurement precision shows an evident reliance on scan parameters: the higher kVp and mAs the lower the uncertainty, see fig. 4.2.C.
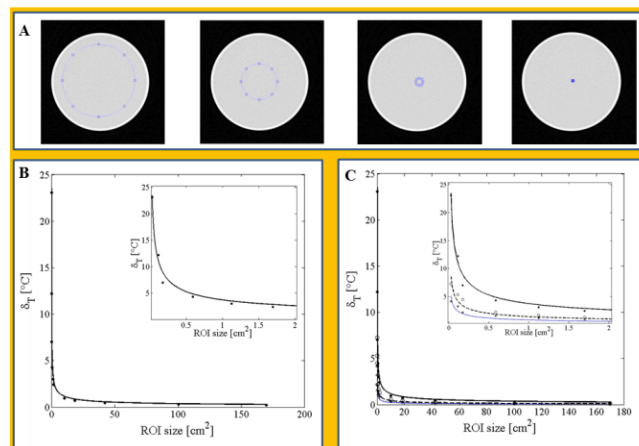
Figure 4.2. A) Slice of the water-equivalent phantom with large, medium-large, medium, and small ROIs selected; B) Temperature uncertainty vs the area of selected ROI at 100kVp and 100 mAs. The fitting curve is shown; C) Temperature uncertainty vs the area of selected ROI for three scan conditions: 100 kVp and 100 mAs (continuous line and black dots), 120 kVp and 200 mAs (dashed line and black circles), 140 kVp and 300 mAs (dotted line and black

asterisks). The fitting curves at the three settings are shown.

This analysis confirms the data of Bruners' study performed on 0.9% NaCl solution [5]. This is an expected result: as a matter of fact the value of SNR increases by increasing mAs and kVp, hence noise contribution to CT number measurement decreases; on the other hand, absorbed dose raises. This finding can be described by showing the histograms of the CT number obtained at the different settings. Figure 3 shows the histograms obtained by considering the CT number of the pixels contained in the large ROI (about 70000 pixels), at the 9 different settings.

Figure 3 clearly shows that the higher the mAs and kVp, the closer the dispersion of the CT number to the mean. It implies that temperature precision improves increasing these two settings, hence raising the patients' dose.
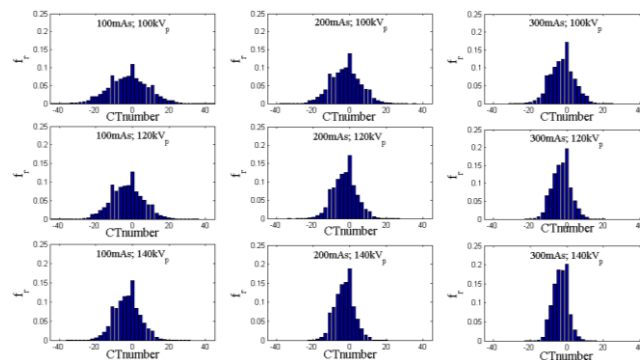

Figure 4.3. Histograms of the pixels' CT number contained in the large ROI at the 9 settings.

IV.1.3 Discussion

The goal of the described study consisted in an experimental analysis of the main factors which influence

precision and sensitivity of CT thermometry, giving the technical basis for clinical evaluation.

The study, conducted on a homogeneous phantom of water, demonstrated that CT number uncertainty and, consequently, temperature uncertainty improves with ROI size and with kVp and mAs values. On the other hand the increase of these two parameters entails an increment of patient's dose. Moreover, the exposition settings did not seem to influence the thermal sensitivity of CT thermometry: the thermal sensitivity varies in a narrow range of values (from -0.37 HU·°C^{-1} to -0.34 HU·°C^{-1}) considering all the nine couples kVp–mAs employed during the trials (Table 4.1).

Particular attention was drawn to the two main requirements to fulfill in hyperthermia thermometry: temperature precision of 1-2 °C and spatial resolution of 1-2 mm.

As a matter of fact, the feasibility of CT thermometry depends on three main factors: spatial resolution, temperature precision, and patient dose. Data showed an inverse relationship between the first two requirements: any improvement in the spatial resolution causes a degradation of temperature measurement precision. Indeed, the precision improved by averaging the CT number on a larger number of pixels (figure 4.3.B and 4.3.C). For a particular scan protocol (i.e., 140 kVp, 300 mAs) a temperature precision of 2 °C at a spatial resolution of 1 mm was met, since the area averaged CT numbers can be obtained with great precision for small ROIs. The presented data fulfil the requirements of CT-based thermometry for the application during thermal ablation therapies as suggested in literature [9].

In conclusion this perspective offers a systematic analysis of the principal influencing factors on CT-based thermometry. Further studies are required to investigate other potential influencing parameters, such as slice thickness, pitch factor and reconstruction kernel.

Summarizing, CT thermometry has turned out to be a promising technique, offering good levels of thermal-spatial detail. *In vivo* biological tissues will have to be investigated, as long as the previous results are obtained for a homogeneous water-equivalent phantom. Physiological effects (e.g., increased local blood perfusion at elevated temperatures) will have to be taken into account as they may cause an atomic composition change in living subjects, contributing to a CT number shift [8]. In addition, further studies are requested in order to quantify and limit the radiation exposure caused by CT thermometry. However, with innovative filters and data reconstruction algorithms, CT thermometry could be developed, after more than three decades, into an efficient clinical tool.

- IV.2 Validation of CT thermometry and monitoring of tissue vaporization during LTA on *ex vivo* swine liver.

LTA outcome strongly depends on the temperature reached within the tissue during treatment, and the spatial temperature distribution defines the amount of vaporized and damaged volume. Therefore, the monitoring of temperature increase during the LTA may be beneficial for improving the therapy outcomes, in order to

completely remove the neoplastic volume, and to avoid thermal damage of the surrounding healthy tissue.

The aims of the present research [10] are: 1) to assess the HU decrease of *ex-vivo* swine livers undergoing LTA at three different power (P) (i.e., 1.5 W, 3 W, 5 W) and at two distances, d, from the applicator (i.e., 3.6 mm, 8.7 mm) and 2) to assess the tissue vaporization during treatment.

IV.2.1 Experimental setup

Nine *ex-vivo* swine livers were treated with a Nd:YAG laser (1064 nm, Smart 1064, DEKA M.E.L.A. s.r.l., Florence, Italy, Fig. 4.4.A).

The radiation was conveyed into a quartz bare fiber applicator with a core of 300 μm diameter (Fig. 4.4.B) using the laser settings reported in Table 4.2.
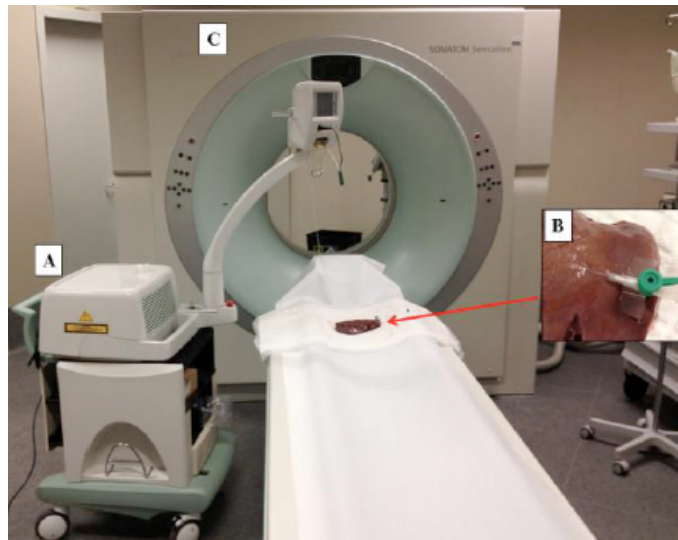
Figure 4.4. Experimental setup: A) laser source; B) laser applicator inside the *ex-vivo* liver; C) CT scanner.

Table 4.2. Laser settings used during LTA

Number of livers treated	P [W]	E [J]	t [s]
3	1.5	300	200
3	3	600	200
3	5	1000	200

During LTA, images were acquired by a CT scanner (Siemens Somatom 64 slices, Fig. 4.4.C) at 150 mAs, 120 kVp and 0.6 mm slices. The total time required to scan the whole organ was 9 s; therefore this was the repetition time at which each slice was acquired. The averaged HU was calculated on two ROIs with ellipsoidal shape of area=0.2 cm^2 and centered at d=8.7 mm (Fig. 4.5.B) and d=3.6 mm (Fig. 4.5.C) downward the applicator (Fig. 4.5.A). A further ROI at a distance d=30 mm (Fig. 4.5.D) from the applicator was used as reference.
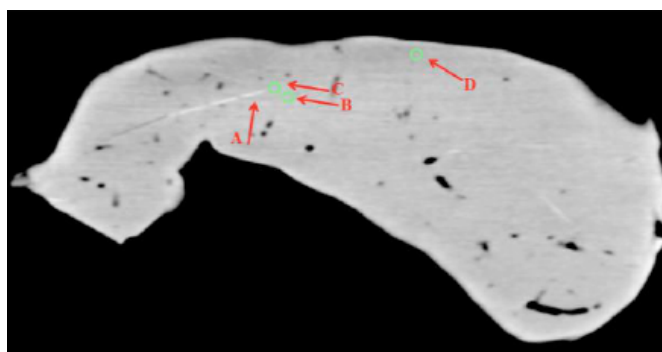
Figure 4.5. CT scan image of the liver: A) applicator; B) ROI at d=8.7 mm; C) ROI at d=3.6 mm of distance; D) ROI of reference (d=30 mm).

IV.2.2 Results

All three livers undergoing LTA at P=1.5 W did not show vaporized region at the end of the treatment, as reported in Fig. 4.6B; on the other hand, all livers showed a vaporized region at the end of treatment when the laser power was 3 W and 5 W. This is depicted in Fig. 4.6D (P=3 W) and 6F (P=5 W) where the vaporized tissue are represented by hypodense regions. In both cases, the selected ROIs, surrounded by green circles, contain vaporized tissue at the end of treatment.
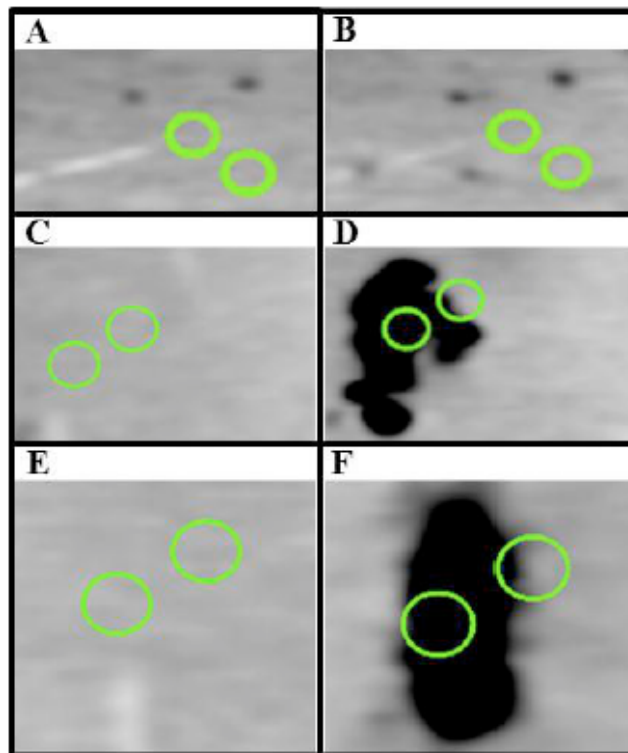
Figure 4.6. CT scan images of the liver close to the applicator. P=1.5 W: A) before and B) at the end of the treatment; P=3 W: C) before and D) at the end of the treatment; P=5 W: E) before and F) at the end of the treatment.

These results confirm data obtained in a previous work where LA was carried out on *ex-vivo* pancreases [11]: at 1.5 W and same time of application the pancreases did not show a vaporized region; tissues showed vaporization when treated at 3 W, 6 W, and 10 W.

The averaged HU can be used to assess the presence of vaporized tissue because of its high variation when the liver tissue has undergone vaporization. In fact, at environmental temperature (22°C±2°C) the 9 *ex vivo* swine livers showed an averaged HU of about 77; this value agrees with the one reported in [5].

Experiments show that tissue vaporization causes a marked decreases of the HU: when a ROI contains only vaporized tissue (Fig. 4.6F), it shows an averaged HU lower than -450. The three livers treated at 3 W show a sudden decrease of the HU in the ROI closest to the applicator (d=3.6 mm) between 90 s and 99 s after the start of the treatment. At 5 W the vaporization starts earlier than at 3 W due to a steep increase of T; in fact the marked decrease of HU happens between 9 s and 18 s after the start of the treatment.

IV.2.3 Discussion

These results agree with literature showing a higher and faster T increase when P increases [11, 12]. When the ROIs do not contain vaporized volume, the HU shows a slight decrease during treatment caused by the increase of T. This phenomenon can be used to observe the tissue temperature variation during LTA.

In order to assess the feasibility of monitoring temperature with CT-based thermometry during tissue hyperthermia induced by laser absorption, we calculated the ΔHU of the

liver undergoing treatment as a function of time:

$$\Delta HU(t) = HU(t) - HU(T_0)$$

(1)

being $HU(T_0)$ the averaged HU in the selected ROI before the starting of treatment and $HU(t)$ the averaged HU in the selected ROI calculated after a treatment time t .

In Fig. 4.7 the trend of ΔHU during the treatment at P=1.5 W is shown for the two selected ROIs and the reference one. In the graphics are reported the mean of ΔHU calculated considering the three livers treated at 1.5 W.
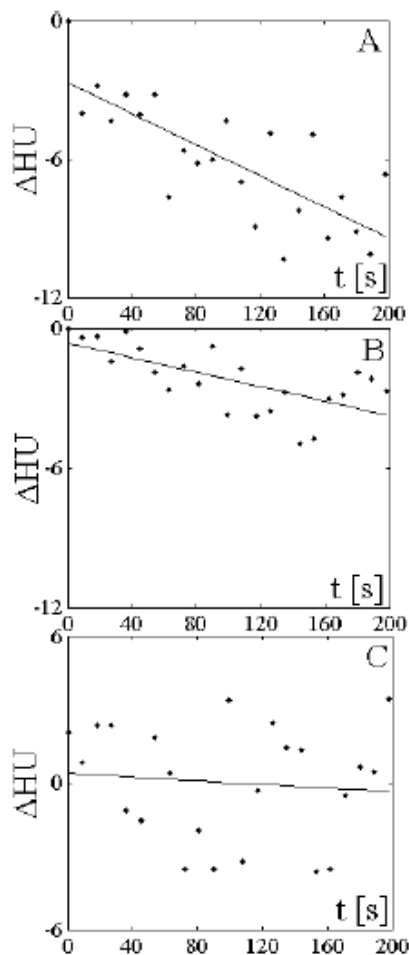

Fig. 4.7. Averaged ΔHU vs t during the treatment at P=1.5 W in the

ROI at the three distances: A) d=3.6 mm; B) d=8.7 mm; C) d=30 mm. The best fitting lines are also reported.

As it is well-known [13], the shorter the distance from the applicator, the higher the temperature increase of tissue having undergone LTA. Therefore we expected a more marked decrease of ΔHU within the ROI close to the applicator (d=3.6mm) than in the ROI at 8.7mm. This is confirmed by experimental data, by comparing Fig. 4.7.A with Fig. 4.7.B; furthermore, this result is strengthened considering a simple linear relationship between ΔHU and t: 1) in both mentioned ROIs the averaged HU decreases during treatment due to the increase of T; 2) in the ROI placed at 3.6 mm (Fig. 4.7.A) the decrease of HU is more evident than in the ROI placed at 8.7 mm (Fig. 4.7.B). This result is confirmed by the slope of the best fitting lines reported in Table 4.3; 3) In the ROI used as reference (d=30 mm), the tissue did not show any significant temperatureincrease during treatment; this is also confirmed by the flat trend of the ΔHU (Fig. 4.7.C) showing a negligible slope (-0.004 s^{-1}).

Table 4.3. Linear regression between ΔHU of the three ROI sans time at P=1.5W. Slope, correlation coefficient and significativity of the best fitting line are reported.

d	P [W]	slope [s^{-1}]	R^2	ρ
3.6 mm	1.5	-0.034	0.60	<0.001
8.7 mm	1.5	-0.016	0.46	<0.001
30 mm	1.5	-0.004	0.009	No sign

Only at high distance (i.e., 30 mm) HU results almost

constant during the treatment and ΔHU and t are not significantly correlated.

Vaporized region was not present in liver treated at 1.5 W, whereas it was evident in livers treated at 3 W and 5 W; these results agree with the ones reported in a previous study on porcine pancreases [11].

During LA, the relative distance between the selected ROIs and the applicator, strongly influences the HU decrease; in fact, a smaller HU decrease is associated with a greater distance from the applicator, and it is negligible at 30 mm because T is almost constant [11, 14].

These findings show that HU variation can be used to assess the tissue region interested to a consistent T increase during treatment.

In conclusion, the assessment of the HU variation could be useful to monitor the effects of LTA in terms of both T variation and the presence of vaporized tissue, with the aim to obtain an effective therapy. The introduction of CT based thermometry in this field is also encouraged by some advantages, such as the non-invasivity and the chance to track tissue modifications during the procedure.

- IV.3 Validation of CT thermometry during MWA: experimental sessions on *ex vivo* swine liver

MWA has gained popularity in recent years as a viable focal therapy for many different tumors including liver cancer [15]. MW energy forces dipoles to continuously realign with an applied electromagnetic field, producing kinetic frictional energy which results into tissue heating

[16]. Cell death occurs due to "coagulative necrosis" from thermal damage and cellular apoptosis.

CT thermometry during thermal ablation procedures has been performed in *ex vivo* animal model during LTA [9, 17] or RFA [18].

The aim of this study [19] is to assess the feasibility of CT thermometry during MWA in an *ex vivo* porcine liver model and to examine the thermal sensitivity of this technique.

IV.3.1 Experimental set-up

The decrease in CT number with temperature can be explained by the thermal expansion of tissue with increasing temperature. This expansion entails a decrease of tissue density and as a consequence a decrease of the linear attenuation coefficient and of the CT number. Simple models are used to describe the CT number dependance on temperature [20]:

$$\Delta CT = -(1000 + CT(T_0)) \cdot \alpha(T - T_0)$$

(1)

where α is the expansion coefficient of the tissue and T_0 is a reference temperature. Equation (1) shows the dependency of CT on T and explains that CT number changes can be used as indirect measurement of tissue temperature.

According to (1), a linear regression analysis was carrried out using all the measured points to determine the best fitting line. Lastly, CT thermal sensitivity was calculated as the slope of the best fitting line. All data analysis was performed in Matlab® environment.

The MWA was performed on healthy porcine livers with two synchronized 2.45 GHz cooled-shaft microwave

antennas (NeuWave Inc., Madison, Wisconsin, USA). Livers were heated for 4 minutes using a power of 65 W for each applicator. The two antennas were placed at a relative distance of about 1 cm.

Two K-type thermocouples, connected to a data acquisition system (FX100, Yokogawa) were used to monitor tissue temperature throughout the entire procedure, with a sample time of 2 s. Thermocouples were inserted within the tissue using a 16-Gauge coaxial needle (~1.6 mm of outer diameter and ~1.2 mm of inner diameter). After inserting each thermocouple, the coaxial needle was extracted to avoid artifacts on CT images. In the first experiment, thermocouples were placed at distances of 1.3 cm and 2.2 cm from the parallel-placed antennas; in the second experiment, thermocouples were moved 1.6 cm and 2.8 cm from the antennas. The positioning of thermocouples at different distances from the antennas allowed temperature recording in a wide range of values. A schematic of the configuration is shown in Fig. 4.8.
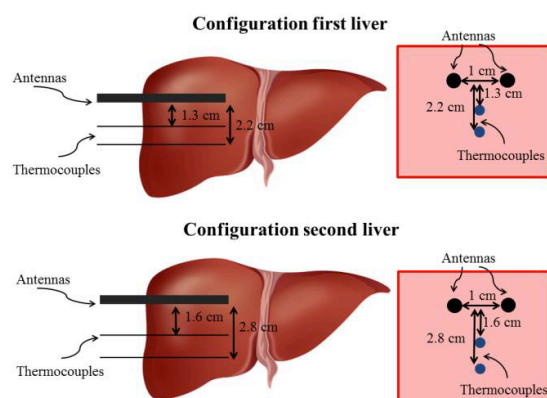

Fig. 4.8. Schematic representation of experimental set up. The antennas were inserted within the porcine liver at a relative distance of 1 cm; the two thermocouples at a variable distance from the center

between the two antennas: in the first liver at 1.3 cm and 2.2 cm, in the second liver at 1.6 cm and 2.8 cm.

All devices were placed under ultrasound guidance, and distances determined by ultrasound were subsequently confirmed by CT images. Experiments were performed at environmental temperature (22±1 °C) and the initial temperature of the livers were almost equal to the environmental one.

Ablations were carried out on a multidetector CT scanner (Discovery CT750 HD; General Electric Healthcare, USA). An initial CT acquisition was performed before starting MWA, and 16 subsequent scans every 15 s along the entire treatment. Applied CT parameters were 120 kVp and 200 mAs and acquired images were volumetrically reconstructed with a slice thickness of 0.625 mm.

The area-averaged CT number was calculated in two ROIs selected close to the tip of each thermocouple. Circular ROIs with an area of approximately 0.02 cm^2, containing about 57 pixels, were used. In order to investigate the CT number dependence on tissue temperature, the averaged CT-numbers monitored during the CT scans were synchronized with the temperature measured by the thermocouples.

IV.3.2 Results

The trends of temperature increase measured by the two thermocouples during MWA of the two livers are shown in Fig. 4.9.
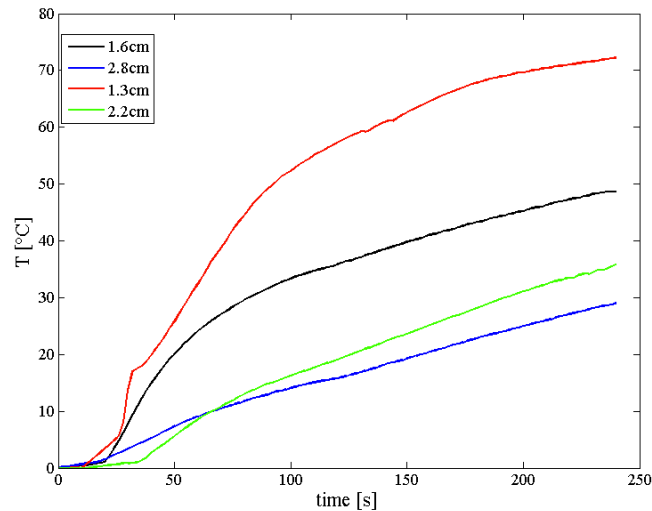
Fig. 4.9. Tissue temperature during MWA at four different distances
(i.e., 1.3 cm, 1.6 cm, 2.2 cm, and 2.8 cm) from the antennas.

As expected, local tissue temperature increased during MWA. The shorter the distance from the applicator, the higher the temperature increase at the end of the treatment: for instance, at the end of the procedure the thermocouple placed at 1.3 cm from the applicator measured a temperature increase of about 71 °C (final temperature of 94 °C), the thermocouple placed at 2.2 cm from the applicator measured an increase of about 36 °C (final temperature of 58 °C).

During treatment, T increases from T_0=22 °C up to a maximum value (Tmax) reached at the end of the procedure. The temperature variations (ΔT) steeply decrease with the distance from the antennae: i.e., the experimental data demonstrate that ΔT at 1.6 cm distance is 67% of the ΔT at 1.3 cm; at 2.2 cm, the ΔT is only 50% of the increase at 1.3 cm; at 2.8 cm it is only 40% of the increase at 1.3 cm. Simultaneously, CT examinations of livers were carried out to monitor the CT number changes caused by MWA heating. The averaged-CT numbers of

the ROIs selected within the two livers undergoing MWA are shown as a function of time (Fig. 4.10). ROIs are selected in correspondence of the thermocouples tips. Hence, they represent the actual CT number changes caused by the ΔT at the four different distances from the antennas (i.e., 1.3 cm, 1.6 cm, 2.2 cm, and 2.8 cm).

Fig. 4.10 clearly shows that the closer is the ROI to the antennas, the larger is the decrease of the averaged-CT number experienced during the MWA (e.g., the ROI at 1.3 cm from the antennas show an averaged CT number difference between the scan performed before starting the treatment and the one obtained at the end of the treatment (ΔCT) of -38.0 HU; the ROI at 2.2 cm shows a ΔCT of -15.9 HU).
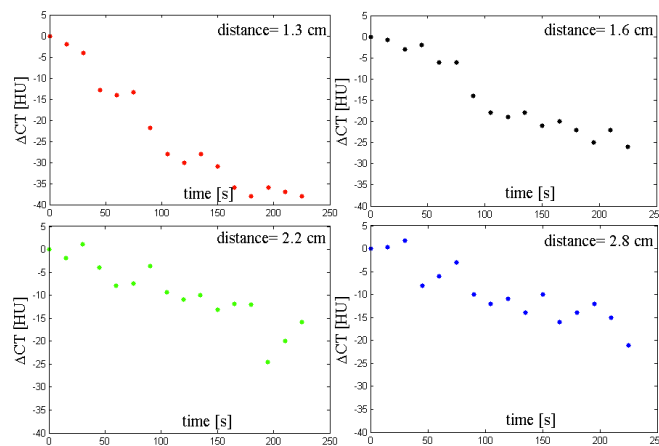
Fig. 4.10. Averaged-CT number as a function of time at the four different distances from the antennas (i.e., 1.3 cm, 1.6 cm, 2.2 cm, 2.8 cm).

Lastly, to investigate the relationship between the ΔCT experienced by the liver tissue and its ΔT, the averaged-CT number monitored during MWA (Fig. 4.10) was

synchronized with the temperature measured by thermocouples (Fig. 4.9). This trend and the best fitting line, considered the linear model reported in Eq. 1, are shown in Fig. 4.11.
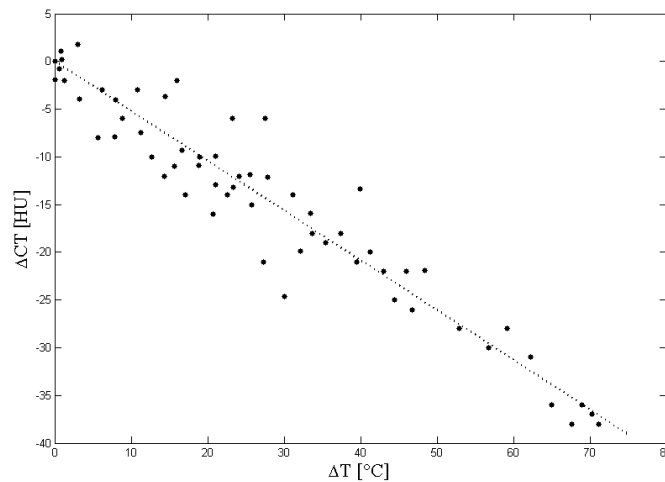
Fig. 4.11. Averaged-CT number change as a function of tissue temperature increase during liver MWA.

The regression analysis showed an inverse linear relationship between the averaged ΔCT number and the ΔT. The thermal sensitivity, considered the slope of the best fitting line, is -0.52 ± 0.02 HU/°C in the considered range (temperature from 22 °C to 93 °C, which corresponds to a maximum ΔT of 71 °C). The good linear fitting is confirmed by the high value of the R^2 (0.91).

IV.3.3 Discussion

Among the several thermometric techniques, data reported in this work show that thermal shift of CT number can be used to monitor temperature change in porcine liver undergoing MWA.

In particular, a linear relationship can be used to model the

dependency of CT numbers on temperature. In the measurement range from 22°C to 93°C, a mean thermal sensitivity of -0.52±0.02 HU/°C was found. The good linear regression is confirmed by the high value of R^2 (0.91) and is supported by other studies reported in literature, which linearize the CT number dependency on temperature by a Taylor series expansion. This hypothesis has been considered valid for both *ex vivo* tissue and phantoms [20], although some authors used quadratic or cubic curves [21, 22].

Thermal sensitivity of this work agrees with data reported by several studies performed on different kind of ex vivo healthy tissues, which show a thermal sensitivity ranging from -0.43 HU/°C up to -0.65 HU/°C. Fallone *et al.* estimated a thermal sensitivity of -0.45 HU/°C on muscle tissue heated by an external water bath [8]. Jenne *et al.* calculated a thermal sensitivity of -0.43 HU/°C by heating pig muscle with High Intensity Focused Ultrasound [23]. Schena *et al.* investigated the performances of CT-thermometry on healthy porcine pancreases, and found a thermal sensitivity of about -0.50 HU/°C [22]. Lastly, the group of research of Pandeya carried out several works focused on the feasibility assessment of CT thermometry for temperature monitoring during hyperthermal procedures. In particular they performed experiments using different sources of heating: *i)* during laser ablation on *ex vivo* bovine liver and they found a thermal sensitivity of -0.65±0.05 HU/°C [17]; *ii)* during radiofrequency ablation on *ex vivo* bovine liver and they found -0.60±0.026 HU/°C; *iii)* by heating *ex vivo* pig liver through hot air and they found a thermal sensitivity of -0.54±0.03 HU/°C [24].

A serious issue in CT thermometry is related to the metal components of the MW antenna, which can cause artifacts in CT image. Nevertheless, they affect absolute CT numbers only in proximity of applicators; as a consequence, CT images cannot be used to monitor the temperature close to the applicator. In this study we demonstrate that CT images can be used to estimate temperature tissue for distances higher than about 1 cm, in fact at 1.3 cm the metallic artifacts are not evident. Experiments were performed employing two antennas, therefore the metallic artifact was worse than in a clinical setting using only one probe. This particular artifact may be mitigated with the use of certain proprietary software. However, these programs were not used during this feasibility study, aiming to insure no alterations to the CT numbers during data acquisition. Nevertheless, information about temperature distribution very close to the applicator may not be very important because the tissue is completely destroyed in this region [9]. On the other hand, temperature distribution at the margins of the ablation zone is crucial, and intermittent CT imaging during ablation or immediately after may allow real-time monitoring of temperatures experienced in the tumor margins, potentially affecting MWA endpoint determination and even clinical outcomes. Summing up, the metallic artifacts do not allow temperature measurement in the immediate vicinity of the antenna(s), but they do not affect monitoring of the tissue temperature at the margins of the ablation zones (i.e. where it is critical to know where the last lethal isotherm occur).

One of the major limitations of the study is that the experiments were performed on healthy *ex vivo* porcine

liver, which may pose substantial differences between ex vivo and in vivo clinical scenarios. For instance, in a clinical setting the patient respiratory movements may worsen the performances of CT thermometry because they can cause motion artefact. Additionally, during *in vivo* trials, measurements can be affected by physiological processes (e.g., blood perfusion) that can cause local alterations in data points due to thermal conductivity and heat redistribution, or "heat sink" effect. A further limitation is related to the presence of thermocouples themselves, which can influence heat distribution because of the high heat conduction of the metallic wires which constitute the thermocouples. Lastly, the presence of thermocouples can also cause image artifact due to their metallic construction: the presence of metal into the organ produces dark streaks with surrounding bright streaks mainly due to beam hardening and scatter effects [25]. This concern has not been considered significant because: *i)* we used very small thermocouples (diameter~1mm), and *ii)* the selected ROIs did not contain the thermocouples, but we selected them close to the thermocouples tip.

In the current study, both thermocouples and CT-thermometry were utilized to analyze and successfully model tissue temperatures during MWA procedures.

Our results support the feasibility of CT-thermometry during MWA. The non-invasiveness of the technique and the capability to provide three-dimensional temperature distributions makes CT-thermometry a potentially valuable tool in improving endpoints and outcomes during thermal ablation procedures, such as MWA. Moreover, it may also provide invaluable information regarding non-

target tissue heating, enabling the operator to better protect adjacent structures for thermal injury. Thanks to these advantages it may supplant or become an alternative to invasive temperature tissue monitoring during CT-guided percutaneous thermal ablation procedures. After further improvements, this technique could be used during MWA of liver tumors in a clinical setting. Moreover, CT-thermometry can also be utilized in the evaluation of different thermal devices, such as comparing the temperature curves and ablation effects of different microwave antennas and generators, without influencing the heat distribution, and more in general in the assessment of new solutions for hyperthermal treatments, such as the use of nanoparticles in laser ablation [26, 27]. One of the main concerns related to the use of this technique is the health risk related to the X-rays dose. Although the dose of a typical CT exam is comparable to the annual dose received from natural sources of radiation [28], temperature monitoring during hyperthermal procedures requires multiple scans of the organ. The Dose Length Product (DLP) related to a thermal procedure guided by CT-thermometry is function of several factors (i.e., CT scan protocol, type of CT scan, scan length, number of scans during the MWA). Therefore, the main recommendation in this application must follow the well-known principles of ALARA: procedure must be performed using doses that are As Low As Reasonably Achievable (ALARA), consistent with the diagnostic task. The aggressive effort of the scientific community to minimize the doses and optimize image quality has led to good results of low dose protocol and pave the way for clinical application of CT-thermometry [28].

- IV.4 Bibliography

1. Bydder GM, Kreel L. The temperature dependence of computed tomography attenuation values. J Comput Assist Tomogr 1979

2. Schena E, Saccomandi P, Giurazza F et al. Experimental assessment of CT based thermometry during laser ablation of porcine pancreas. Phys Med Biol (58) 2013 5705-16.

3. G.D. Pandeya, M. Greuter, B. Schmidt, T. Flohr, and M. Outkerk, "Assessment of thermal sensitivity of CT during heating of liver: an ex vivo study," Brit J Radiol, vol. 85, pp. e661-5, 2012.

4. N. Weiss, J. Sosna, S.N. Goldberg, and H. Azhari, "Non-invasive temperature monitoring and hyperthermic injury onset detection using X-ray CT during HIFU thermal treatment in ex vivo fatty tissue," Int J Hyperthermia, vol. 30, pp. 119-125, 2014.

5. P. Bruners, E. Levit, T. Penzekofer, P. Isfort, C. Ocklenburg, B. Schmidt, T. Schmitz-Rode, R.W. Günther, and A.H. Mahnken, "Multi-slice computed tomography: a tool for non-invasive temperature measurement?" Int J Hyperthermia, vol. 26, pp. 359-365, 2010.

6. Schena E, Fani F, Saccomandi P, Massaroni C, Frauenfelder G, Giurazza F, Silvestri S. Feasibility assessment of CT-based thermometry for temperature monitoring during thermal procedure: Influence of ROI size and scan setting on metrological properties. Conf Proc IEEE Eng Med Biol Soc. 2015 Aug;2015:7893-6. doi: 10.1109/EMBC.2015.7320222. PubMed PMID: 26738122.

7. Joint Committee for Guides in Metrology 100:2008, "Evaluation of measurement data – Guide to the expression of uncertainty in measurement".

8. B.G. Fallone, P.R. Moran, E.B. Podgorsak, "Noninvasive thermometry with a clinical X-ray CT scanner," Med Phys, vol. 9, pp. 715-721, 1982.

9. L. Frich, "Non-invasive thermometry for monitoring hepatic radiofrequency ablation," Minim Invasiv Ther Allied Technol, vol. 15, pp. 18-25, 2006.

10. G. M. Bydder, L. Kreel, The temperature dependence of computed tomography attenuation values. J. Comput. Assist. Tomogr., vol. 3, pp. 506-510, 1979.

11. Schena E, Saccomandi P, Giurazza F, Del Vescovo R, Mortato L, Martino M, Panzera F, Di Matteo FM, Beomonte Zobel B, Silvestri S.

Monitoring of temperature increase and tissue vaporization during laser interstitial thermotherapy of ex vivo swine liver by computed tomography. Conf Proc IEEE Eng Med Biol Soc. 2013;2013:378-81. doi: 10.1109/EMBC.2013.6609516. PubMed PMID: 24109703.

12. P. Homolka, A Gahleitner and R. Nowotny Temperature dependance of HU values for various water equivalent phantom materLDOV_´_Phys. Med. Biol., vol. 47, pp. 2917-2923, 2002.

13. P. Saccomandi, E. Schena, M. A. Caponero, F. M. Di Matteo, M. Martino, M. Pandolfi and S. Silvestri. Theoretical analysis and experimental evaluation of laser-induced interstitial thermotherapy in ex vivo porcine pancreas. IEEE T Bio-Med Eng, vol. 59, pp. 2958-64, 2012.

14. S. C . Jiang and X. X. Zhang. Dynamic modeling of photothermal interactions for laser induced interstitial thermotherapy: parameter sensitivity analysis. Lasers Med. Sci., vol. 20, pp. 122-131, 2005.

15. U. Leung, D. Kuk, M.I. D'Angelica, T.P. Kingham, P.J. Allen, R. P. DeMatteo, W.R. Jarnagin, Y. Fong Y, "Long-term outcomes following microwave ablation for liver malignancies," British J. Surg., vol. 102, pp. 85-91, 2015

16. C.L. Brace, "Microwave ablation technology: what every user should know," Curr. Probl. Diagn. Radiol., vol. 38, pp. 61-67, 2009

17. G.D. Pandeya, J.H.G.M. Klaessens, M.J.W. Greuter, B. Schmidt, T. Flohr, R. van Hillegersberg, M. Oudkerk, "Feasibility of computed tomography based thermometry during interstitial laser heating in bovine liver," Eur. Radiol., vol. 21, pp. 1733-1738, 2011

18. P. Bruners, G.D. Pandeya, E. Levit, E. Roesch, T. Penzkofer, P. Isfort, B. Schmidt, M.J.W. Greuter, M. Oudkerk, T. Schmitz-Rode, C.K. Kuhl, A.H. Mahnken, "CT-based temperature monitoring during hepatic RF ablation: Feasibility in an animal model," Int. J. Hypertherm., vol. 28, pp. 55-61, 2012

19. P. Homolka, A. Gahleitner, R. Nowotny, "Temperature dependence of HU values for various water equivalent phantom materials," Phys. Med. Biol., vol. 47, pp. 2917-2923, 2002

20. S. Bentzen, J. Overgaard, J. Jorgensen, "Isotherm mapping in hyperthermia using subtraction X-ray computed tomography," Radiother. Oncol., vol. 2, pp. 255-260, 1984

21. E. Schena, P. Saccomandi, F. Giurazza, M.A. Caponero, L. Mortato, F.M. Di Matteo, F. Panzera, R. Del Vescovo, B. Beomonte Zobel, S. Silvestri, "Experimental assessment of CT-based

thermometry during laser ablation of porcine pancreas," Phys. Med. Biol., vol. 58, pp. 5705-5716, 2013

22. J.W. Jenne, M. Bahner, J. Spoo, P. Huber, R. Rastert, I. Simiantonakis, W.J. Lorenz, J. Debus, "CT on-line monitoring of HIFU therapy," Proc IEEE Ultrason Symp 1997, pp.1377-1380

23. G.D. Pandeya, M.J. Greuter, B. Schmidt, T. Flohr, M. Oudkerk, "Assessment of thermal sensitivity of CT during heating of liver: an ex vivo study," British J. Radiol., vol. 85, pp. e661–e665, 2012.

24. J. F. Barrett, N. Keat, "Artifacts in CT: recognition and avoidance," Radiographics, vol. 24, no. 6, pp. 1679-1691, 2004.

25. R. Mooney, E. Schena, A. Zhumkhawala, K. S. Aboody, J. M. Berlin, "Internal temperature increase during photothermal tumour ablation in mice using gold nanorods," 37th Annual International Conference of the IEEE, Engineering in Medicine and Biology Society (EMBS), pp. 2563-2566, 2015.

26. R. Mooney, E. Schena, P. Saccomandi, A. Zhumkhawala, K. Aboody, J. M. Berlin, "Gold nanorod-mediated near-infrared laser ablation: in vivo experiments on mice and theoretical analysis at different settings," Int J Hyperthermia, vol. 33, no. 2 pp.150-159, 2017.

27. C. H. McCollough, A. N. Primak, N. Braun, J. Kofler, L. Yu, J. Christner, "Strategies for reducing radiation dose in CT," Radiol Clin N Am, vol. 47, no. 1, pp. 27-40, 2009.

28. R. F. Grasso, R. L. Cazzato, G. Luppi, F. D'Agostino, E. Schena, R. Del Vescovo, F. Giurazza, E. Faiella, B. Beomonte Zobel, "Percutaneous lung biopsies: performance of an optical CT-based navigation system with a low-dose protocol," Eur Radiol, vol. 23, no. 11, pp. 3071-3076, 2013.

Chapter V

Temperature monitoring based on Magnetic Resonance imaging

After having discussed the role of CT thermometry in the previous chapter, now the aim is to analyze the feasibility of MR thermometry during ablation procedures.

Before deepening this issue it is crucial to underline that, being MR scanner based on high field magnets, only amagnetic devices can be adopted when working in this radiological setting.

Compared to CT thermometry, MR shows some advantages: high thermal sensitivity, low sensitivity to motion, good linearity and it does not employ ionizing radiation [1].

The first investigation about the influence of temperature on MR parameters was conducted by Bloembergen *et al.* [2] in 1948, and only after four decades Jolesz and coauthors proposed to guide laser ablation by Magnetic Resonance Imaging [3]. Since the study of Jolesz, a big research effort has been dedicated to assess the feasibility of MR-thermometry for temperature monitoring during hyperthermal procedures, and several groups have focused their scientific activities on the improvement of MR thermometry in terms of accuracy and of both spatial and temporal resolution [4, 5]. The use of MR-thermometry is particular attractive during LTA, because the laser light can be transported within the MR environment by a fiber optic, as a consequence specific MR-compatible devices are not required. The calibration of MR-thermometry

technique requires the use of MR-compatible temperature sensors; the most prominent are FBG sensors.

In this chapter I report the experimental sessions I performed to assess the feasibility of MR-thermometry during LTA on pancreas and liver *ex vivo*, evaluating the influence of different MR parameters.

- V.1 MR guided thermometry during LTA on *ex vivo* swine pancreas

The aim of this work [6] is threefold: to assess the feasibility of three sequences (IRTF, SRTF, and FLASH) during LTA of pancreas; to calculate the thermal sensitivity of MR thermometry using the three abovementioned sequences on freshly excised pancreatic tissues undergoing LTA; the comparison between the characteristics of MR thermometry using the three sequences.

In order to perform this study, the reference temperature has been measured by MR-compatible temperature sensors (i.e., FBG sensors).

V.1.1 Background

In this study we used T1-weighted sequences during experiments, hence we focused our attention on the T1-based MRI thermometry principles.

T1 of water protons is a measure of how quickly the protons return to the initial equilibrium conditions (ground state in the direction of the static magnetic field B0), after the interruption of the radiofrequency signal. The return of

nuclei to a lower energy state is associated with the interaction of the dipoles with the lattice, which is due to their translational and rotational motion [7]. These motions cause an increase of temperature which is related to T1 as expressed by (1) [8, 9]:

$$T_1 \propto \exp\left(-\frac{E_a(T_1)}{kT}\right)$$

(1)

where k is the Boltzmann constant, $E_a(T_1)$ is the activation energy of the relaxation process, and T is the absolute temperature. This relationship can be linearized in a wide temperature range (e.g., from 30 °C up to 70 °C):

$$T_1 - T_1^{ref} = m(T - T^{ref})$$

(2)

where T^{ref} is the reference temperature, m is the thermal coefficient, empirically determined for each tissue [10], and T_1^{ref} is the T_1 value at temperature T^{ref}.

Tissue coagulation during the LTA may affect tissue properties causing non-linear effects. Furthermore, due to the above-mentioned dependence of T1 from tissue type, the knowledge of thermal coefficients of each tissue is essential to obtain a temperature map [1].

V.1.2 Experimental setup

The light emitted by a Nd:YAG laser (1064 nm, Smart 1064, DEKA M.E.L.A. s.r.l. Florence, Italy), was conveyed into a quartz fiber applicator (external diameter of 300 μm) within an *ex vivo* swine pancreas. The LA was carried out with laser power of 2W and laser energy of 2700 J (as a consequence the treatment lasted 1350 s), deposited within the tissue with continuous wave mode.

The heating process was monitored simultaneously by the FBG sensors, and by the 1.5-T MR scanner using three T1-weighted sequences: IRTF, SRTF, and FLASH. Twelve MR scans were performed during the whole LTA procedure. During each scan, IRTF, SRTF and FLASH sequences were consecutively run-off. The first scan was performed at room temperature, before starting the LTA, the following eleven scans during the heating process. The settings for each MR sequence are listed in Table 5.1, where: TR (repetition time) is the amount of time existing between successive pulse sequences applied to the same tissue slice, TE (echo time) represents the time between the application of the 90° pulse and the peak of the echo signal, TI (inversion time) is the time period between the 180° inversion pulse and the 90° excitation pulse in IRTF and SRTF, FA (flip angle) is the angle to which the net magnetization is rotated relative to the main magnetic field direction, FOV is the field of view, slice thickness is the thickness of each scanned slice, and bandwidth is the frequency range of the excitation radiofrequency signal transmitted to each pixel. Such parameters are mostly responsible for the quality and contrast of the image [7]. The freshly excited pancreas was placed into an MRI compatible box (10 x 10 x 2 cm) composed of polymethyl methacrylate (PMMA), necessary to insert the applicator and the FBGs, and to control their relative distances during LTA. The mask does not affect the signal of the images. Fig. 1a shows the pancreas contained in the PMMA box placed within the coil of 1.5-T MR scanner (Siemens Magnetom Avanto, 1.5 T); Fig. 1b shows the top-view of the box and the positions of the laser applicator and the three fibers, each of them equipped with

one FBG sensor (represented in figure as FBG1, FBG2 and FBG3). The FBG sensors have a 1 cm - length sensing element and the FBG centers are placed at the same quote of the applicator axis (Fig. 5.1c). The laser applicator was inserted into the tissue at a depth of 1 mm and at the center of the box.

The analysis of MR images obtained using the three sequences (IRTF, SRTF and FLASH) was performed by placing the center of three ROIs in correspondence of the axis of each FBG sensor. For each scan of the image, three ROIs were selected, for a total of 36 samples for each sequence.

The variation of T_1, due to the increase of temperature (Eq. 2), entails a change in image signal intensity, ΔI. In order to obtain the thermal dependence of ΔI, images were analyzed in ROIs centered in correspondence of the FBG sensors. The FBGs output (Bragg wavelength, λ_B) was recorded by an optical spectrum analyzer (Optical Sensing Interrogator, sm125, Micron Optics). The optical spectrum analyzer records the wavelength shift due to the temperature variation with a sample frequency of 250 Hz.

Table 5.1 Parameters of IRTF, SRTF and FLASH sequences used for MR-based thermometry in pancreas undergoing LA.

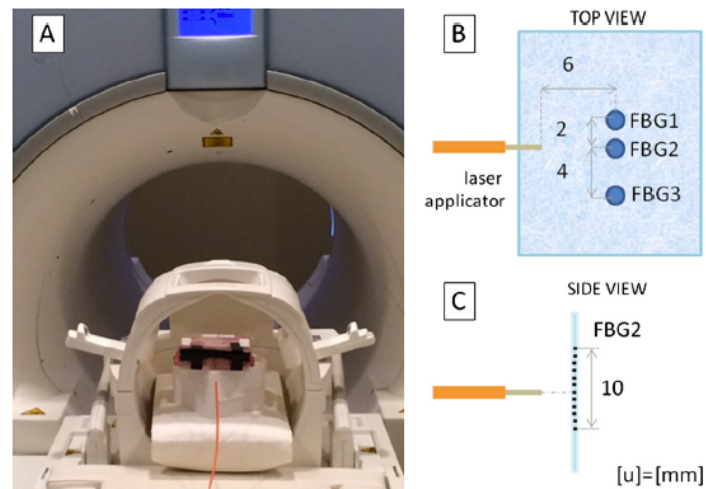|	IRTF	SRTF	FLASH
TR (ms)	820	820	20
TE (ms)	1.66	1.66	4.8
TI (ms)	520	520	\
Flip angle (°)	20	20	70
FOV (mm²)	300×300	300×300	300×300
Slice thickness (mm)	3.5	3.5	3.5
Bandwidth (Hz/pixel)	400	400	200

Fig. 5.1. Experimental set up for the MR thermometry during LTA in pancreas: (a) placement of the pancreas within the PMMA box inside the MR scanner; (b) top view of the PDMS box and positions of laser applicator and FBG sensors; (c) sensitive length of the FBG sensors and positions with respect to the applicator axis. All measurements are expressed in millimeters.

V.1.3 Static calibration of fiber Bragg gratings sensors

The temperature increment during LTA was estimated by the calibration curve of the FBG sensors. Before to perform MR thermometry experiments on livers, all the FBG sensors were calibrated using an experimental set up composed of: (i) an optical spectrum analyzer (Bragg Fiber Sensing, FS2200 8 CH, Sequoia Technology Group Ltd.), which records the output (λ_B) of the FBGs, (ii) an oven to control the temperature, (iii) a module to acquire and record the signal provided by four K-type thermocouples (FX106-4-2, YOKOGAWA®), (iv) a PC to record the output data from the optical spectrum analyzer and process data.

The calibration was performed between 18 °C and 100 °C. The mean value of the measures obtained by the four thermocouples was used as reference for the FBGs calibration. The change of the Bragg wavelength ($\Delta\lambda_B$) for each sensor during the whole process was recorded and synchronized with the temperature provided by the thermocouples in order to obtain the calibration curves of the FBGs by fitting the $\Delta\lambda_B$ with T.

The curves have been obtained by a linear regression of the data. A typical calibration curve was linear with a slope of approximately 0.010 nm °C^{-1}, which was considered the thermal sensitivity of the sensors.

V.1.4 Results and discussion

The relationship between ΔS, and the temperature increase, ΔT, was obtained by synchronizing and then correlating the averaged intensity of each ROI with the temperature values measured by the FBGs.

First of all the noise of the images obtained using the two sequences was analyzed. We considered the standard deviation, std, of the pixels intensity in a ROI with no nuclear MR signal. The std was calculated considering a ROI with about 4800 pixels in three images, the first one obtained using IRTF, the second one using SRTF, and the last using the FLASH. The STRF image showed lower noise (std = 0.57) than the IRTF image (std = 1.4), whereas the FLASH showed an intermediate value (std = 0.96).

Regarding the analysis of pixel intensity (I) in the image representing the tissue, it must be considered that the std increases because of the tissue inhomogeneity. A typical histogram obtained selecting a ROI of about 600 pixels

representing a region of the pancreas is shown in Fig. 5.2, considering images produced by using the three sequences. The same region of pancreas was selected.

The std values of the image obtained by SRTF is slightly lower than the one obtained by IRTF and FLASH (i.e., 5.6, 7.3 and 9.1 for SRTF, IRTF and FLASH, respectively). The tissue inhomogeneity could influence the performances of the MR thermometry.
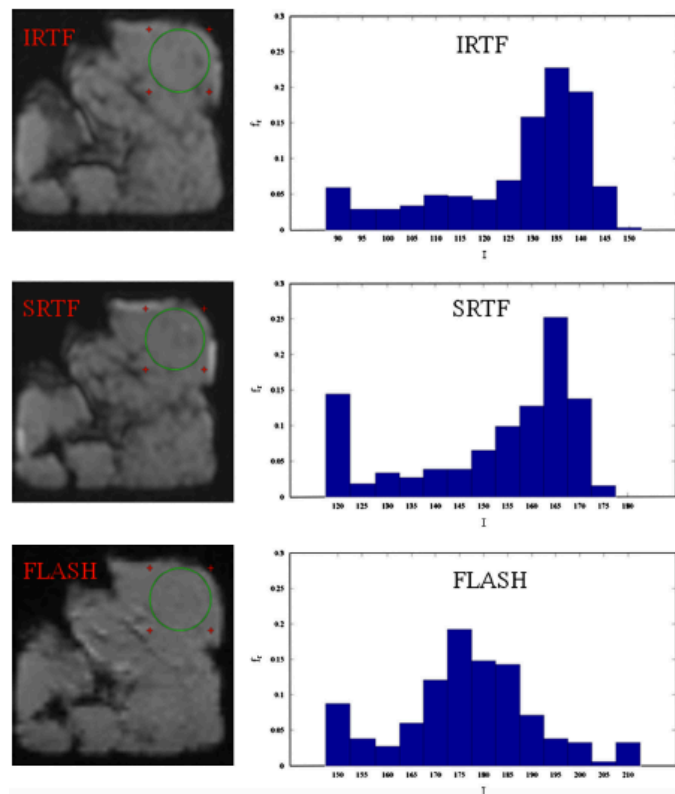

Fig. 5.2. Histograms of the signal intensity of a ROI (green circle) representing a region of pancreas obtained using IRTF, SRTF and FLASH sequences.

After this preliminary analysis, the changes of signal intensity, ΔI, during the treatment, caused by the

temperature increase was investigated. The changes of signal intensity, ΔI, was calculated as the difference between the intensity of the selected ROI with the reference image acquired at room temperature (before starting the LTA); ΔI was calculated for all the MR scans performed during the LTA and for the three sequences (ΔI_{IRTF}, ΔI_{SRTF} and ΔI_{FLASH}). Fig. 5.3 shows ΔI as a function of ΔT.

Fig. 5.3 shows that the use of IRTF allows increasing the sensitivity: the slope of the best fitting line, which represents the thermal sensitivity, is -1.47 ± 0.08 °C^{-1} using IRTF, -0.95 ± 0.05 °C^{-1} using SRTF and -0.56 ± 0.04 °C^{-1} using FLASH. On the other hand the correlation with ΔT improves using SRTF, as shown in Fig. 5.3 and confirmed by the values of correlation coefficient, R^2 (i.e., 0.94, 0.87 and 0.87 and for SRTF, IRTF and FLASH, respectively).
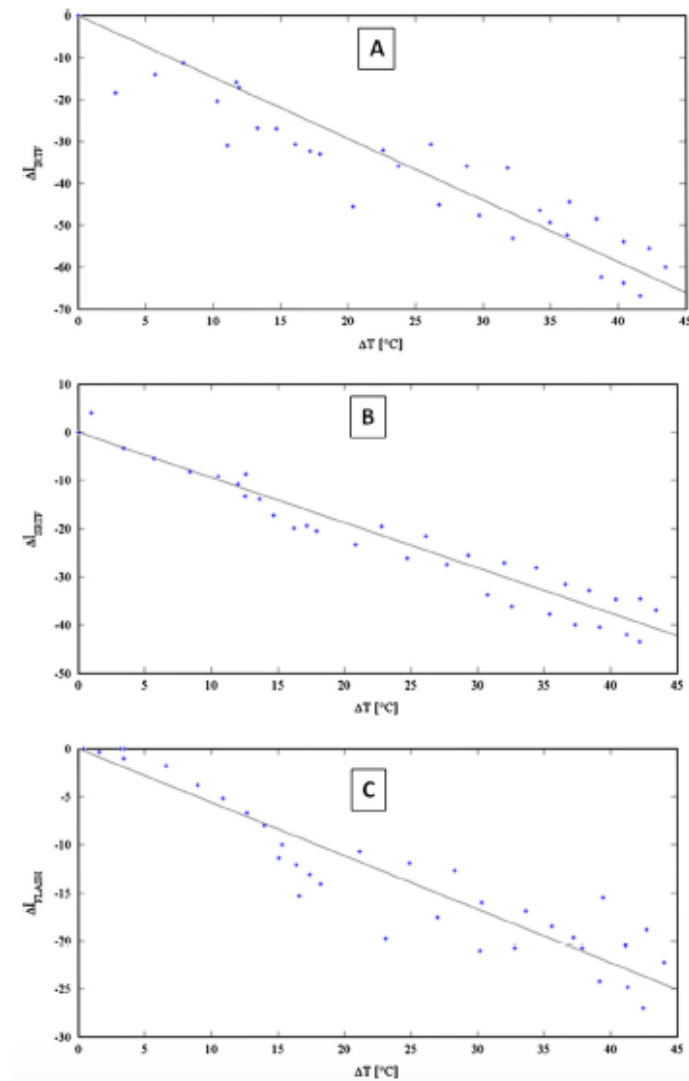
Fig. 5.3. Change of signal intensity, ΔI, as function of the change of temperature, ΔT, in pancreas undergoing LTA treatment (asterisks), scanned with (a) IRTF, (b) SRTF and (c) FLASH sequences. The best fitting lines for each sequence is shown.

Fig. 5.4 shows a comparison between the temperature increases measured by FBGs (ΔT_{ref}) and the ones estimated by the three sequences (ΔI_{IRTF}, ΔI_{SRTF} and ΔI_{FLASH}) obtained by considering the three best fitting lines reported in Fig. 5.3.
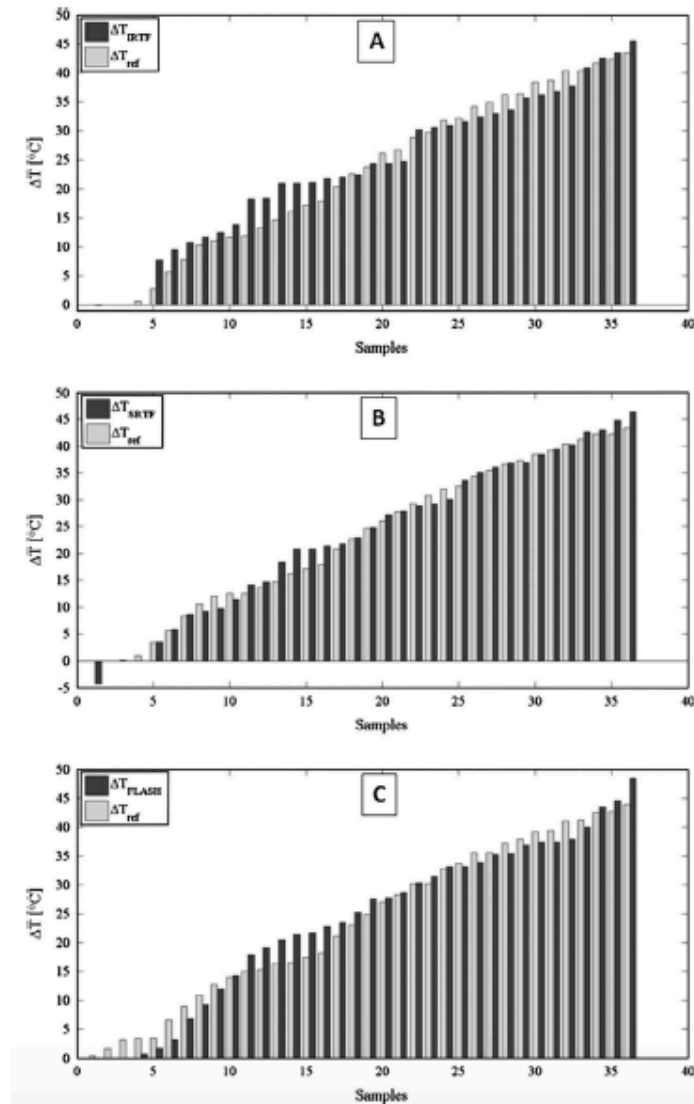
Fig. 5.4. Comparison between the temperature increases measured by FBG (ΔT_{ref}) and the temperature increase estimated by the change of signal intensity in the three sequences (a) IRTF, (b) SRTF and (c) FLASH.

Fig. 5.4 shows that for the 12 scans performed during LTA on the pancreas, the differences between the ΔT estimated by SRTF and the ΔT estimated by FBGs are

lower than the ones between the ΔT estimated by IRTF and FLASH sequences and the ΔT estimated by FBGs. This consideration is also confirmed by the Root Mean Squared Error for the three sequences calculated as:

$$RMSE_{sequence} \sqrt{\frac{\sqrt{\sum_{i=1}^{N}(\Delta T_{ref} - \Delta T_{sequ\ nce})^2}}{N}}$$

(4)

The value of RMSE$_{IRTF}$, RMSE$_{SRTF}$ and RMSE$_{FLASH}$ are 0.9°C, 0.7°C and 0.9°C respectively.

The improvement obtained by performing the estimation by SRTF has also strengthened by the results of Bland Altman analysis [11]; the range defined by the limit of agreements (LOAs) for SRTF (i.e, from -6.2 °C to 7.2 °C) confirms the better precision of these measures than the ones obtained by IRTF (i.e., from -7.7 °C to 9.8 °C) and FLASH (i.e., from -9.9 °C to 10.6 °C); also the mean of differences (MODs) show a lower value for SRTF and FLASH (i.e., 0.5 °C and 0.3 °C, respectively), than the MOD of IRTF (i.e., 1.0 °C).

The performances of IRTF, SRTF and FLASH sequences in the monitoring of temperature increase on pancreas undergoing LTA are also confirmed by results obtained by Bazrafshan et al. on phantoms and ex vivo porcine liver [4, 9]. Considering the absolute value of the thermal sensitivity, the highest one is achieved by using IRTF (-1.2 °C^{-1}), followed by SRTF and FLASH (-1 °C^{-1} and -0.9 °C^{-1}, respectively); on the other hand the FLASH has the smallest MOD value (0.8 °C, for SRTF and IRTF is 1.6 °C and 1.7 °C, respectively). Similar results were obtained for liver phantom by the same authors [4], with absolute modulus of thermal sensitivity decreasing from IRTF (-

1.49 °C^{-1}) to FLASH (-1.15 °C^{-1}) sequences. Differences in thermal sensitivity of the same sequences when employed for temperature monitoring in pancreas and liver are reasonably due to the tissue-dependence of T1 relaxation time. This characteristic makes the thermal sensitivity of T1-weighted images being dependent to the tissue [1]. Therefore a tissue-specific calibration of the T1 sequence employed during MRI thermometry would be required to improve the effectiveness of the technique. The abovementioned issue could be overcome by the use of other methods, such as PRF shift method, at the expenses of the marked thermal sensitivity exhibited by T1 relaxation time, especially at low field and of the artifact due to movements [1, 12].

V.1.5 Conclusion

This study presents the assessment of MR based thermometry during LTA on healthy porcine pancreas. Three *T1*-weighted sequences, IRTF, SRTF and FLASH, were evaluated by comparing the *ΔI* with the *ΔT* measured by MR compatible sensors based on fiber Bragg technology. The IRTF sequence showed higher sensitivity than the SRTF and FLASH ones; the SRTF sequence has the best precision, representing a good compromise for the employment during MR based thermometry.

Moreover, SRTF, IRTF and FLASH are standard sequences, therefore commonly used in clinical practice for the traditional analysis.

This study collocates in the challenging scenario of real time thermometry by non-invasive approaches during LTA. The characterization of already existing medical imaging techniques, as MR, for thermometric purposes

could represent a valuable tool to lead the physician in the optimal laser settings during thermal ablation procedure. This technique is particularly attractive for LTA due to the laser MR-compatibility.

- V.2 Temperature monitoring and volume ablation extimation MR-guided during LTA on *ex vivo* swine liver

After having discussed in the previous section the feasibility of MR thermometry in course of pancreas ablations, now the aim is to report on the same technique during liver ablation [13].

Liver is not only a different tissue, and so presenting different biological properties, but even an organ of the human body more frequently involved by metastatic lesions; from a clinical point of view, the impact of the reported results could have a relevant meaning in the daily practice of physician performing tumors liver ablations. As in the previous section, T1-weighted sequences have been adopted for MR thermometry.

V.2.1 Experimental setup

Static calibration of fiber Bragg grating sensors

Twelve FBGs, employed as reference thermometer during MR based thermometry on liver, were calibrated to estimate the temperature coefficient ($c_{\Delta T}$) (see also section V.1).

FBG sensors were placed inside a thermostatic chamber (B.E.77, BICASA, Italy), where the temperature was

adjusted and changed between 20 °C and 80 °C; the output of two silicon band-gap sensors, located inside the chamber, was used as temperature reference (LASCAR ELECTRONICS EL USB-2-LCD, accuracy of ± 0.5 °C) for the calibration of FBGs. The calibration curve is obtained by a linear fit of the data provided by the twelve FBGs, using the least mean squares error algorithm. The range of $c_{\Delta T}$ values, estimated by fitting the experimental data with a level of confidence of 95%, is $c_{\Delta T} = 0.008417 \pm 0.000004$ nm °C^{-1} [14].

Experimental setup: MR settings and data acquisition
LTA was performed by Nd:YAG laser (1064nm, Smart 1064, DEKAM.E.L.A s.r.l, Florence, Italy), delivering the radiation to an MR compatible fiber applicator (core of diameter 300 μm). It operated with a power of 2 W for 4 min on three livers.

It was used as a similar experimental setup described in our previous work [14]. Each organ was placed into an MR compatible box (10×10×2 cm), necessary to insert the applicator and FBGs and to control their positions during LTA. Fig. 5.5a shows a 3D view of the box and the positions of the laser applicator and the four fibers $F1$, $F2$, $F3$, $F4$, each of them equipped with 3 FBGs. The FBGs length was 1 mm. The laser applicator was inserted into the tissue at a depth of 2 mm and exactly at the center of the box.
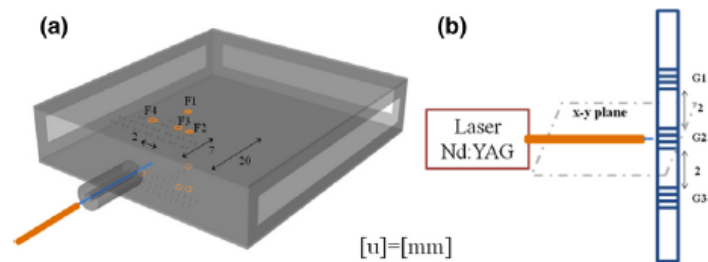
Fig. 5.5. (a) 3D rendering of polymeric box used to place organ, and to control distances between laser applicator and optical fibers housing FBGs, placed in positions $F1$, $F2$, $F3$, $F4$; (b) arrangement of FBGs ($G1$, $G2$, $G3$) inside one fiber, and quotes with respect to x–y plane of applicator.

Three FBGs, $G1$, $G2$ and $G3$, housed in each optical fiber (Technica SA Beijing Operation, China), are placed at an edge-to-edge distance of 2 mm each other; considering that the x-y plane of the applicator is perpendicular to the plane of the optical fibers, the central FBG, $i.e.$, $G2$, is placed at the same quote of the applicator (Fig. 5.5b). The four fibers were placed at the same four positions in all the tests corresponding to the center of the four ROIs selected to analyze the images. An optical spectrum analyzer, OSA (Optical Sensing Interrogator, si425, MicronOptics, stability of 2 pm), with sampling frequency of 250 Hz, was used to interrogate FBGs, and to monitor $\Delta\lambda_B$ during experiments. The OSA is provided with four channels, which allows the outputs of four fibers to be monitored. The three FBGs housed in each fiber were designed to have different λ_B ($i.e.$, 1.533, 1.541 and 1.549 nm, at 23 °C), to distinguish their output. A PC was employed to collect data from OSA.

The average of the data acquired from the three sensors $G1$, $G2$ and $G3$ housed on the same fiber was calculated,

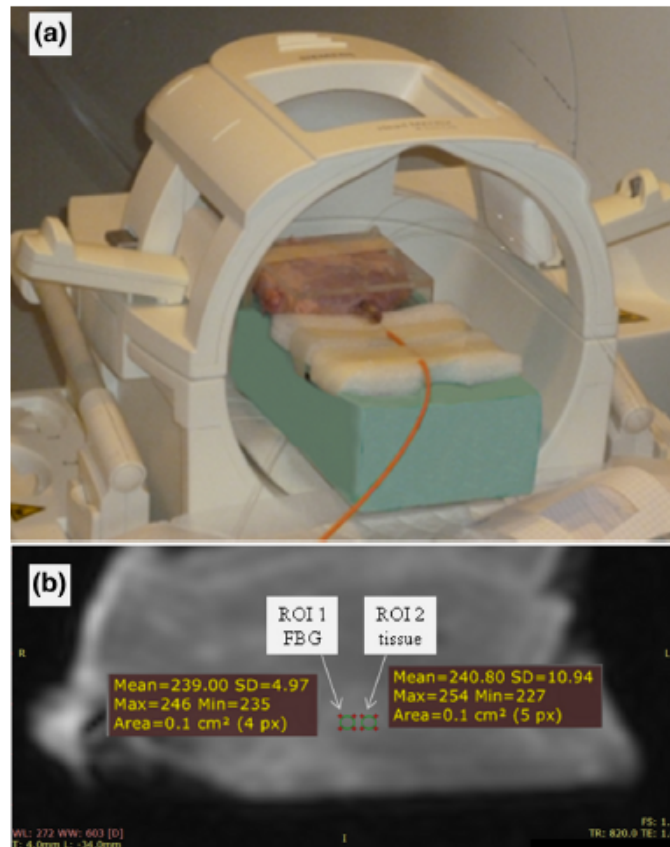considering that MR slice have thickness of 4 mm. Fig. 5.6 shows the experimental setup.

Fig. 5.6. (a) Experimental setup: liver tissue inside polymeric mask used to arrange laser applicator and FBGs, placed within MR coils; (b) MR image of liver before LTA and comparison of signal intensity between ROI placed on FBG sensor (ROI 1) and ROI on normal tissue (ROI 2).

The heating process was monitored by the 1.5-T MR scanner (Siemens Magnetom Avanto, 1.5 T), utilizing two different T1-weighted sequences: inversion recovery turbo flash (IRTF) and saturation recovery turbo flash (SRTF). IRTF and SRTF are standard sequences, and their thermal sensitivity and usefulness to monitor LTA is under

investigation [15, 16]. The sequences parameters are listed in Table 5.2.

Table 5.2. SRFT and IRFT sequence parameters used for MR thermometry during LTA.

Parameters	IRFT	SFRT
TR [ms]	820	820
TE [ms]	1,6	1,6
TI [ms]	520	520
FA [°]	20	20
FOV [mm]	280×280	280×280
ST [mm]	4	4
Number of slices	3	1
Matrix [pixel]	128×128	128×128
Bandwidth [Hz/pixel]	399	399
TA [s]	820	820

These parameters were chosen to obtain high image quality, and signal to noise ratio within a reasonable acquisition time (TA<3 s) [4]. The two sequences were alternately repeated 8 times during the whole ablation procedure (treatment time of 4min). Definitively, 8 IRTF and 8 SRTF images were obtained for each porcine liver and pancreas.

Four ROIs, centered in the same positions of the fibers, were selected for each MR image using the Radiant Dicom Viewer software. The averaged pixel value of each ROI, with a circular shape of 0.1 cm^2 (4 pixels), was read out. The data were elaborated in Matlab ® environment. The presence of optical fiber does not affect MR image. Indeed, before starting the LTA, the signal intensity in the ROI placed on the FBG sensors was compared with the value of signal intensity in another region of the organ, in both liver and pancreas. In each case the small changes of signal intensity are due to the inhomogeneity of the tissue,

and are negligible: as shown in Fig. 5.6.b, the mean value of the signal intensity in the ROI 1, placed on the FBG sensor, is 239, whereas the ROI 2 shows the value of 241 in a generic tissue position.

V.2.2 Results

Temperature measurement with FBGs

The initial T of the liver was registered (about 25 °C) before starting the LTA. Fig. 5.7 shows the temperature increases, ΔT, monitored by $F1$, $F2$, $F3$ and $F4$ during LTA, as a function of time, t. Each curve shown in Fig. 5.7 was obtained by averaging the outcomes of the three FBGs embedded in the same fiber. These data refer to one porcine liver; the same experimental setup and the LTA parameters, were used for the other two livers.

In each trial, $F1$ shows an almost constant temperature trend during LTA: the maximum temperature increment measured at the end of the LTA (ΔT_{max}) is about 5 °C. Indeed $F1$ is enough distant from the applicator ($d=2$ cm, Fig. 5.5), hence it is not experiencing any significant temperature increases. Instead, $F2$, $F3$ and $F4$, being close to the laser applicator ($d= 0.7$ cm), are subjected to a large temperature increase during the treatment. The maximum temperature increment registered by $F2$ was 32 °C, while $F3$ and $F4$ measured a peak increment, ΔT_{max}, of about 28 °C and 20 °C, respectively. $F2$ and $F3$ are placed in the direction of the main heat conduction, therefore they show highest ΔT values.
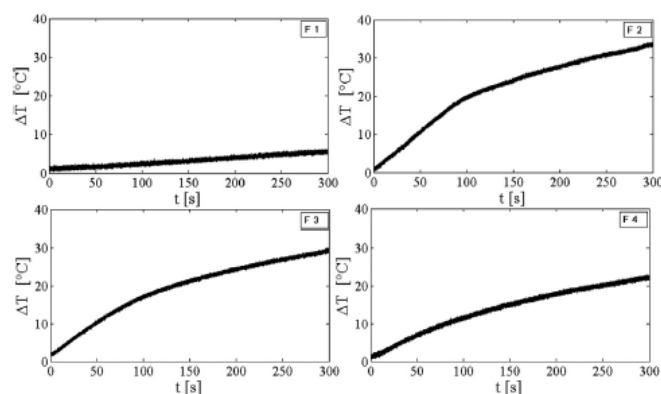
Fig. 5.7. Temperature increases, ΔT, as a function of time, t, monitored by F1, F2, F3 and F4 in porcine liver undergoing LTA.

Temperature measurement with MR T1-weighted images

Before starting LTA, a reference scan at initial T was acquired for each liver. Fig. 5.8 shows the signal intensity trend (pixel value) as a function of time during the whole LTA procedure, for the same liver in Fig. 5.7.
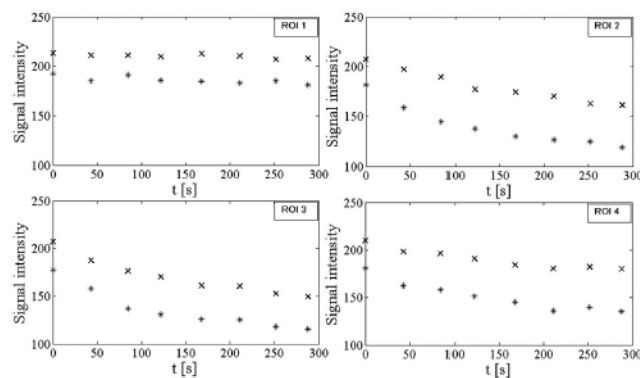

Fig. 5.8. Intensity variations within the four ROIs during LTA: image obtained with SRTF (cross) and IRTF (asterisks).

For the three livers, the signal intensity of the images presents a decreasing trend during LTA in the ROIs 2, 3 and 4, due to the high temperature increment; on the other

hand, the averaged signal intensity of ROI 1 is characterized by an almost constant trend due to the higher distance from the laser applicator.

The averaged variation of the signal intensity of the three livers, ΔS, was calculated for each ROI. Then, ΔS was correlated and synchronized with the temperature increment, ΔT, monitored by the FBGs. In particular, ΔS is the difference of ROI values between the current and the reference image acquired at the beginning of the trial. Each ROI corresponds to the position of one fiber, i.e., ROI 1 on F1, ROI 2 on F2, ROI 3 on F3, and ROI 4 on F4 (Fig. 5.5a). This is shown in Fig. 5.9.
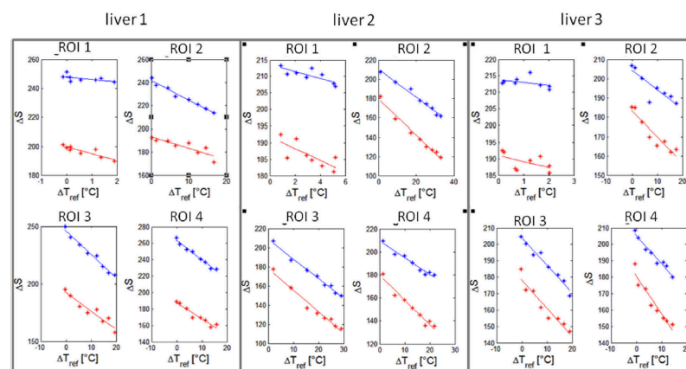

Fig. 5.9. Intensity variations (ΔS) *vs* temperature increase (ΔT) in the three livers undergoing LTA: experimental data (dots) and best fitting lines (continuous lines) using IRTF (red dots) and SRTF (blue dots) sequences.

Finally, data of ROIs 2, 3 and 4 of each liver were matched for a global assessment of the experiment, obtaining $\Delta S=f(\Delta T)$ for the IRTF and SRTF images. Data calculated by ROI 1 were considered as reference. The trend and the best fitting line are shown in Fig. 5.10.
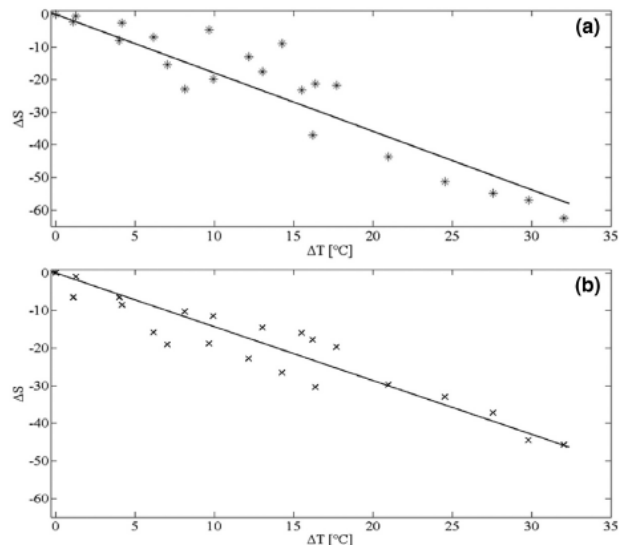
Fig. 5.10. Intensity variations (ΔS) *vs* temperature increase (ΔT) in liver undergoing LTA: experimental data (dots) and best fitting lines (continuous lines) using: (a) IRTF and (b) SRTF sequences.

Considering Eq. 5 $T_1 - T_{1ref} = m \cdot (T - T_{ref})$, where T_{ref} is the reference temperature, T is the current temperature, and m=dT1/dT is the thermal coefficient $[s \cdot °C^{-1}]$, empirically determined for each tissue, the slope of the fitting line in Fig. 5.10 represents the thermal coefficient β. Higher slope (absolute value) is due to higher intensity decrease with temperature, and the thermal coefficient represents the thermal sensitivity of the MR sequence. Table 5.3 shows β, the Pearson correlation coefficient R, and the significance of the linear fitting.

Table 5.3. Thermal coefficient, β, Pearson correlation coefficient, R, and the significance, *p*-value, of the linear fitting in liver tissue.

	β [°C^{-1}]	R	p-value
IRFT	[−1,8 ± 0,2]	−0,94	< 0,001
SRFT	[−1,4 ± 0,1]	−0,94	< 0,001

The comparison between the MR-based temperature measurements and the reference ones is assessed by using Bland–Altman method [17]. It is a graphical approach developed in 1983 for the comparison of two measurements methods. The Bland–Altman analysis was carried out for both IRTF and SRTF (Fig.11). The MR-based temperature was estimated by Eq.5, i.e., multiplying the signal intensity variation with the thermal coefficient β of the specific sequence.
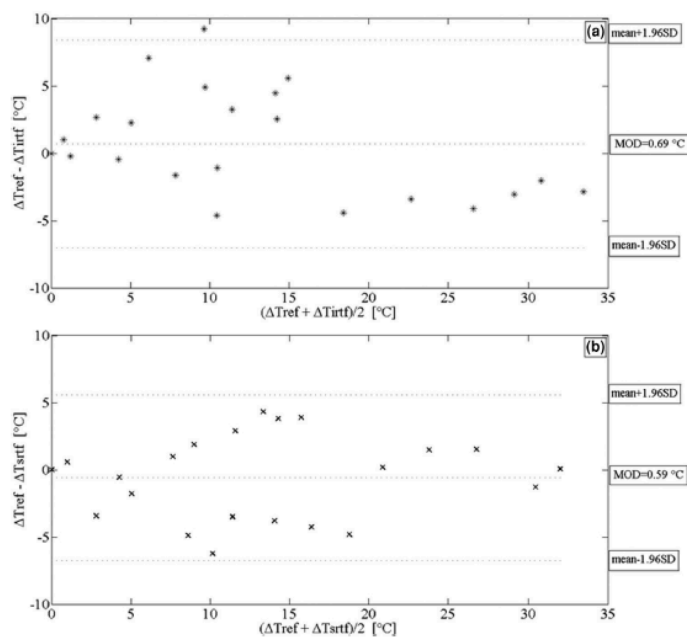

Fig. 5.11.Bland-Altman plot for measurement performed on livers with: (a) IRTF and (b) SRTF sequences. The limits of agreement and the mean of difference are reported with dotted lines.

Table 5.4. Mean of difference (MOD) and limits of agreement (LOA) values for the two sequences used for MR thermometry in liver.

	MOD [°C]	LOA [°C]
IRFT	−0.7	8.3/−7.0
SRFT	−0.6	5.5/−6.8

In this study, the Bland–Altman method is used to evaluate the accuracy and the precision of the MR-based thermometric approach. Table 5.4 lists the values of the mean of difference (MOD) and limits of agreement (LOA) values for the two sequences. MOD can be employed as index of the accuracy of the investigated method (MR-based temperature measurements) with respect to the reference one (temperature measurements performed by FBGs). $LOA = MOD \pm 1.9 \cdot$ std, where std is the standard deviation of the difference between the two methods (reported on the y-axis of Fig. 5.11). LOA represents the limits including 95% of differences between the two measurement methods.

Fig. 5.12 shows the linear regression between ΔT measured by FBGs (ΔTref) and T estimated by the change of signal intensity in $T1$-weighted images considering the two sequences.

The good agreement between theoretical and experimental data is confirmed by the closeness of the best fitting line (continuous line) to the line of equality, since the slope of the best fitting line is close to 1 (i.e., 1.1 for the IRFT sequence and 0.9 for the SRFT). The uncertainty related to the best fitting line is estimated considering a level of confidence of 95%, and it represents the dispersion of data with respect to the mean value (i.e., the slope of the best

fitting line). In both cases shown in Fig. 5.12, the uncertainty is low (0.1 for IRFT and 0.2 for SRFT) considering the whole range of measurement. Nevertheless, not negligible dispersion of data is observed at low temperature change (0°C–20°C), probably because within this range the T1-weighted images are more sensitive to the tissue inhomogeneity than to the temperature increase.
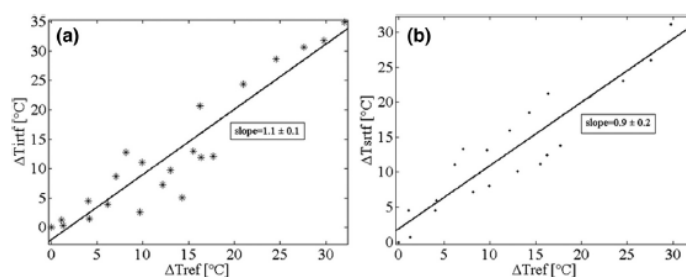

Fig. 5.12. Linear regression between ΔT measured by FBGs (ΔT ref) and T estimated by the change of signal intensity: best fitting line (continuous line) calculated using (a) IRTF and (b) SRTF.

V.2.3 Discussion and conclusion

This study assessed the temperature sensitivity, accuracy and precision of two different T1-weighted sequences (IRTF and SRTF) during LTA on healthy porcine liver. FBGs were used to measure the temperature throughout the treatment. FBGs are preferred because of their MR compatibility and the absence of measurement artifacts, due to radiation absorption, as in case of thermocouples; such artifacts can cause overestimation of up to 20 °C [12, 18].

The sequence parameters were chosen to obtain high image quality and signal to noise ratio within a reasonable acquisition time. They were set identical in the two

sequences in order to provide the acquisition consistency. The results obtained agree with those already reported in literature, in particular the IRTF sequence resulted more sensitive than the SRTF (-1.8 ± 0.2 °C^{-1} *vs* -1.4 ± 0.1 °C^{-1}). These data correspond, to some extent, with the results reported by Bazrafshan et al. [4] for a liver-mimicking gel phantom.

In terms of accuracy, represented by MOD, for both sequences adopted, a MOD value lower than 1 °C was obtained: $MOD_{SFRT} = 0.6$ °C and $MOD_{IFRT} = -0.7$ °C. These data are lower than those reported in previous studies [9] ($MOD_{SFRT} = 1.57$ °C and $MOD_{IFRT} = 1.65$ °C).

LOA gives information related to the data dispersion. For the IRTF sequence it was obtained a confidence interval greater than the SRTF sequence one, for both the liver and the pancreas, in agreement with Bazrafshan et al. [9].

MR-based thermometry was performed to test the reliability of the method, by comparing our results with already published data. Our results show that the IRTF sequence provides higher temperature sensitivity and a lower precision and accuracy.

Future works could be addressed to the investigation of influence of ROI size and FOV dimension on the precision of the measurement.

3D real time MR-based thermometry is presently under investigation of many groups, with interesting results [19]. This technique represents a valuable tool to lead the physician in the choice of optimal laser settings during thermal ablation procedure. Lastly, LTA monitoring by MR-thermometry is particularly attractive, because LTA is

amenable to MR-guidance of small, flexible fiber optics to
reach targets in deep-lying organs.

- V.3 Bibliography

1. V. Reike, K. Butts Pauly, MR thermometry, J. Magn. Reson. Imag. 27 (2008) 376–390.

2. N. Bloembergen, E.M. Purcell, R.V. Pound, Relaxation effects in nuclear magnetic resonance absorption, Phys. Rev. 73 (1948) 679–712.

3. F.A. Jolesz, A.R. Bleier, P. Jakab, et al., MR imaging of laser–tissue interactions, Radiology 168 (1988) 249–253.

4. B. Bazrafshan, F. Hubner, P. Farshid, et al., Temperature imaging of laser-induced thermotherapy (LITT) by MRI: evaluation of different sequences in phantom, Lasers Med. Sci. 29 (2014) 173–183.

5. N. Todd, M. Diakite, A. Payne, D.L. Parker, In-vivo evaluation of multi-echo hybrid PRF/T1 approach for temperature monitoring during breast MR-guided focused ultrasound surgery treatments, Magn. Reson. Med. 72 (2013) 793–799.

6. P. Saccomandi, C. Massaroni, S. Silvestri, F. Giurazza, G. Frauenfelder, B.B. Zobel, E. Schena. Feasibility assessment of magnetic resonance-thermometry on pancreas undergoing laser ablation: Sensitivity analysis of three sequences. Measurement 80 (2016) 21–28.

7. J.T. Bushberg et al., Magnetic resonance imaging (MRI), in: The Essential Physics of Medical Imaging, second ed., Lippincott Williams & Wilkins, 2002, pp. 415–468.

8. D.L. Parker, V. Smith, P. Sheldon, L.E. Crooks, L. Fussell, Temperature distribution measurements in two-dimensional NMR imaging, Med. Phys. 10 (1983) 321–325.

9. B. Bazrafshan, F. Hübner, P. Farshid, J. Paul, R. Hammerstingl, et al., Magnetic resonance temperature

imaging of laser-induced thermotherapy: assessment of fast sequences in ex vivo porcine liver, Future Oncol. 9 (2013) 1039–1050.

10. H.E. Cline, J.F. Schenck, R.D. Watkins, K. Hynynen, F. Jolesz, Magnetic resonance-guided thermal surgery, Magn. Reson. Med. 30 (1993) 98–106.

11. J.M. Bland, D. Altman, Statistical methods for assessing agreement between two methods of clinical measurement, Lancet 327 (1986) 307–310.

12. P. Saccomandi, E. Schena, S. Silvestri, Techniques for temperature monitoring during laser induced thermotherapy: an overview, Int. J. Hyperther. 29 (2013) 609–619.

13. G. Allegretti, P. Saccomandi, Giurazza F et al. Magnetic Resonance based thermometry during laser ablation on ex vivo swine liver and pancreas. Medical Engineering and Physics. 2015 Jul;37(7):631-41

14. E. Schena, P. Saccomandi, F. Giurazza, M.A. Caponero, L. Mortato, F.M. Di Matteo et al. Experimental assessment of CT-based thermometry during laser ablation of porcine pancreas. Phys Med Biol 2013;58:5705–16.

15. T.J. Vogl, F. Hübner, N.N. Naguib, R.W. Bauer, M.G. Mack,N.E.A. Nour-Eldin, et al. MR-based thermometry of laser induced thermotherapy: temperature accuracy and temporal resolution in vitro at 0.2 and 1.5 t magnetic field strengths. Lasers Surg Med 2012;44:257–65.

16. P. Colin, P. Nevoux, M. Marqa, F. Auger, X. Leroy,A. Villers, et al. Focal laser interstitial thermotherapy (LITT) at 980 nm for prostate cancer: treatment feasibility in Dunning R3327-AT2 rat prostate tumour. BJU Int 2012;109:452–8.

17. D.G. Altman, J.M. Bland. Measurement in medicine: the analysis of method comparison studies. Statistician 1983;32:307–17.

18. F. Manns, P.J. Milne, X. Gonzalez-Cirre, D.B. Denham, J.M. Parel, D.S. Robinson. In situ temperature measurement with thermocouple probes during laser interstitial thermotherapy (LA): quantification and correction of a measurement artifact. Laser Surg Med 1998;23:94–103.

19. M Ries, B.D. De Senneville, S. Roujol, Y. Berber, B. Quesson, C. Moonen. Real-time 3D target tracking in MRI guided focused ultrasound ablations in moving tissues. Magn Reson Med 2010;64:1704–12.

Chapter VI

Temperature monitoring based on Ultrasound imaging

As assessed in previous sections, the most used non invasive methods for monitoring temperatures during thermal ablation treatments are based on MR, CT and US images [1, 2], according to the effects of temperature on factors that influence the feature of diagnostic images.

Although some concerns are reported in literature and only a few studies have focused on US-thermometry, this technique can be the solution to tackle some issues related to the use of MR and CT thermometry, such as the use of expensive and MR-compatible tools and the X-ray dose to the patients, respectively.

Now, in order to complete the evaluation of all the available techniques, clinically adopted to perform image based thermometry, I report this preliminary experience of US thermometry in course of LTA on *ex vivo* swine liver

- VI.1 Preliminary analysis of ultrasound thermometry during laser-therapy ablation on *ex vivo* swine liver

The aim of this experimental session is to assess the feasibility of US-thermometry during laser thermal ablation (LTA) of biological tissue using a specific US imaging techniques based on elastography and especially

acoustic radiation force imaging (ARFI). The treatment was performed on *ex vivo* pig liver. The thermal sensitivity was investigated considering the changes of the propagation velocity of shear waves as a function of tissue temperature.

VI.1.1 Background

This technique is one approach that uses brief, high-intensity, focused ultrasound pulses to generate 'radiation force' in tissue. This radiation force generates tissue displacements that are tracked using conventional correlation-based ultrasound methods. Thermometry based on this technique uses the sensitivity of shear waves velocity to temperature changes, as reported in [3, 4].

Acoustic Radiation Force Impulse (ARFI) Imaging
Acoustic radiation force based elasticity imaging methods utilize focused acoustic beams to intra-convert acoustic compressional waves to shear waves through the absorption of acoustic energy, and the tissue response to this acoustic radiation force is monitored to derive information about the underlying tissue structure and stiffness.

Elasticity imaging methods involving acoustic radiation force have been under investigation for several years, e.g., [5-14].

These methods offer some advantages over those requiring external excitation: the force is applied directly to the region of interest, thus smaller stresses are used, and challenges associated with coupling the excitation to the desired tissue region are diminished.

In a medium such as soft tissue, in which the primary cause of attenuation is absorption and the contribution to attenuation from scattering can reasonably be neglected [15], the magnitude of radiation force (F) from a focused ultrasound pulse in a specific spatial location is dictated by the absorption (α) and speed of sound (c) of the tissue, and the local temporal average intensity (I) of the acoustic beam [16]:

$$F = \frac{2\alpha I}{c}$$

(1)

This force is in the form of a body force. The geometry of a typical focused radiation force field is directly related to the image shown in Figure 6.1. This figure portrays the simulated tissue displacement response to a typical impulsive (i.e. < 1 ms) acoustic radiation force excitation; immediately after force application, the displacement response reflects the distribution of the applied force. The volume and geometry of the tissue that is excited (i.e. the region of excitation, or ROE) is spatially distributed throughout the geometric shadow of the active transducer aperture and varies considerably with tissue attenuation.
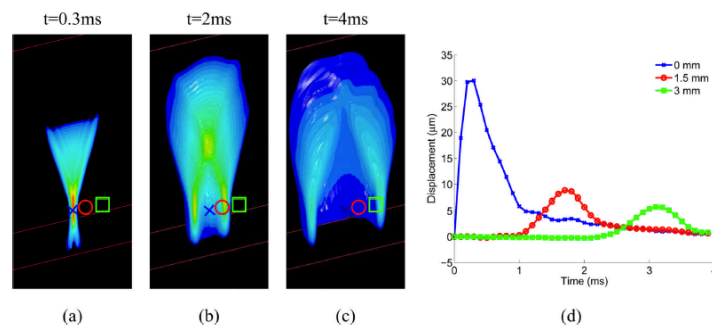

Figure 6.1. Images (a)–(c) portray the simulated axial displacement response in a 3D, homogeneous, isotropic, elastic tissue (E, the elastic Young's modulus, = 4kPa) to a focused (F/1.3 focal configuration,

frequency= 6.7 MHz), impulsive (pulse duration = 50 μs), radiation force excitation, at three snapshots in time after the excitation (0.3ms, 2 ms, and 4ms). The transducer is located at the top of the images, focused in the center of the plane, at 20 mm in depth (marked by the blue X in the images). The red circle is located at 1.5 mm laterally, and the green square at 3 mm laterally in the images. The 3D tissue volume has been bisected so that the central axial/lateral plane is visible. The displacement response at each symbol (x, circle, square) as a function of time after excitation is shown in (d). Positive displacement indicates displacement in the direction of acoustic wave propagation, or down in the images. Initially, (image (a)), the axial displacement response is spatially distributed in the geometry of the applied radiation force, confined within the ROE, with the largest displacement near the focus; the peak focal displacement of 30 μm occurs at 0.4 ms after excitation (blue line in (d)). With increasing time after excitation, a shear wave propagates away from the ROE, decreasing in amplitude with propagation distance due to geometric spreading. In viscoelastic media such as tissue, shear wave attenuation would further decrease the shear wave amplitude with increasing propagation distance. The peak displacement amplitude is inversely proportional to the tissue elastic (shear) modulus, and the speed of the shear wave propagation is quadratically related to the shear modulus [14].

For the generation of images portraying relative differences in tissue stiffness, Acoustic Radiation Force Impulse (ARFI) imaging has been developed [17], in which the tissue displacement response is monitored within the ROE, and image data are generated by sequentially interrogating different lateral positions, as is done in conventional 2D ultrasound imaging. Images are then synthesized of tissue displacement at a given time after radiation force excitation at each interrogation location. Monitoring the displacement response within the ROE has the advantage of higher displacement magnitude and signal to noise ration (SNR) (as compared to outside

of the ROE), but quantification of tissue elasticity within this region is challenging due to inertial effects and the excitation source term within the ROE.

Acoustic radiation force impulse (ARFI) image generation
ARFI images are formed using commercial diagnostic ultrasound scanners to both generate localized, impulsive acoustic radiation forces in tissues, and to monitor the transient, dynamic displacement tissue response within the ROE using correlation based methods. An ARFI pulse sequence consists of tracking beams and pushing beams. The tracking beams are conventional B-mode ultrasound beams (A-lines), and the pushing beams are transmitted along the same A-line and have higher intensity, with typical parameters as specified in Table 6.1.

Table 6.1. Typical parameters used for an ARFI push pulse in different clinical scenarios [17].

Frequency	2–7 MHz
F-number	F-2
Intensity($I_{sppa.5}$) *	1400 W/cm^2
Intensity($I_{spta.3}$)	0.7 W/cm^2
Mechanical Index	1.5–3.0
Pulse Duration	0.1–0.5 ms
Temperature Rise	0.02–0.2°C
Displacement (peak)	10–20 μm

A typical sequence involves transmitting a series of pre-push reference A-lines, which are used to monitor underlying physiologic motion, followed by a pushing pulse along the same A-line, and then a series of tracking A-lines that are utilized to monitor the tissue displacement

response within the ROE of the pushing beam (typically for 3–5 ms at pulse repetition frequencies between 5 and 10 kHz).

VI.1.2 Experimental setup

Experiments were carried out by using a Nd:YAG laser (wavelength of 1064 nm, Smart 1064, DEKA M.E.L.A s.r.l, Florence, Italy) in three *ex vivo* pig liver.

The laser light was conveyed within an optical applicator (the diameter of the core is 300 μm) at a power of 5W. In each organ was placed a thermocouple close to the applicator tip (the distance ranges from 1.5 cm to 2.5 cm) used to record a reference temperature. A picture of the experimental set-up is shown in Fig. 6.2.B. The positioning of the applicator and the thermocouple was eco-guided (Fig. 6.2.A). The organ was scanned by an US system (Siemens ACUSON S3000, Fig. 6.2.C) and the propagation velocity was measured in a region of interest (ROI) of 1 x 0.5 cm. The ROI is close to the thermocouple. In this way it was possible to investigate the influence of tissue temperature (measured by the thermocouple) on the shear waves velocity (provided by the echography system).
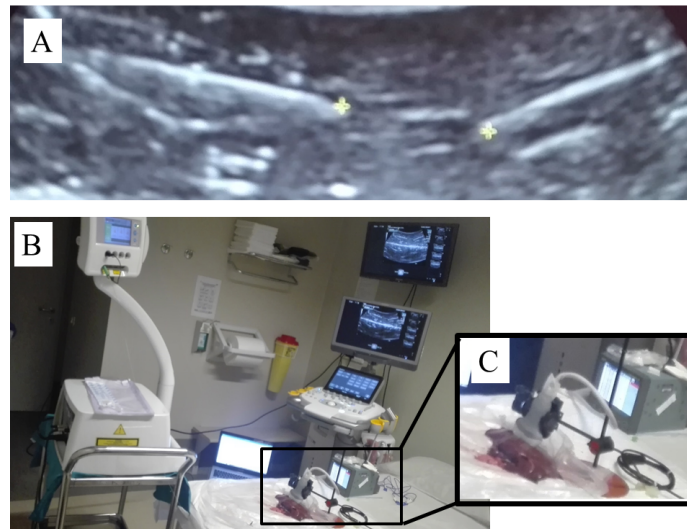
Fig. 6.2. A) Ultrasound image used to position the applicator and the thermocouple within the organ; B) experimental set-up: the laser, the echography, the liver and the system used to record the thermocouple output are shown; C) a particular of the liver and the echographic probe is shown.

VI.1.3 Results

Experimental data (Fig. 6.3) show that the shear wave velocity has a very low sensitivity to temperature up to approximately 55-60 °C, and in all cases the velocity is lower than 5 m·s^{-1}; while for temperature higher than this value the velocity shows a steep increment. In fact in the large part of the cases the system measured a value "over limit" that means a velocity higher than 10 m·s^{-1}, that is the full scale. These results are comparable to the one reported in literature [4].
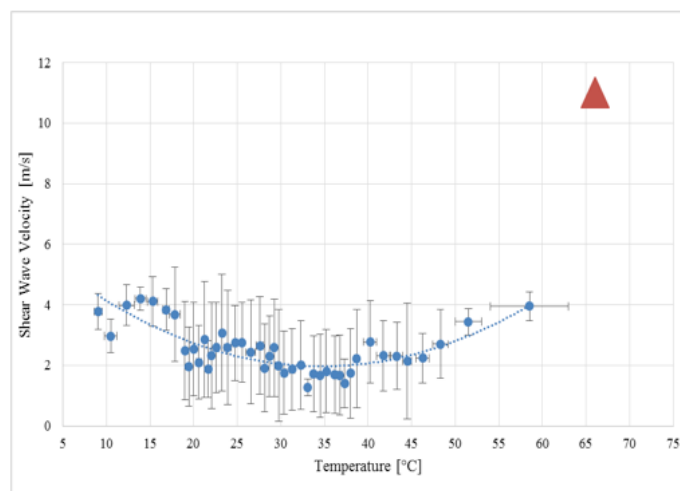
Fig. 6.3. Shear waves velocity as a function of temperature considering the three experiments.

In addition, Fig. 6.3 shows that the trend of the shear wave velocity *vs* temperature can be described by a quadratic model, which shows a minimum value around 30°C - 35°C. This quadratic model agrees with the experimental data in a wide range of values (from ≈10°C to ≈55°C).

VI.1.4 Conclusions

We performed a preliminary feasibility assessment of US thermometry for temperature monitoring during LTA. Although results show a very low sensitivity up to 55-60°C, the method shows an abrupt output change at temperatures higher than these values. This is the main finding of our work and can have a significant clinical impact. The development of a method able to discriminate the volume of the tissue that reaches temperature higher than 55°C can be used to define the boundary of the damaged volume; indeed temperature close to 60 °C

causes an irreversible damage of the biological tissue in few seconds.

Future works are required to clarify the eventual role of this cost-effective and radiation free technique that could lead safely percutaneous ablation procedures.

- VI.2 Bibliography

1. F. Fani, E. Schena, P. Saccomandi, S. Silvestri, "CT-based thermometry: An overview," Int J Hyperthermia, vol. 30, no. 4, pp. 219-227, 2014.

2. V. Rieke, K. Butts Pauly, "MR thermometry. J Magn Reson Im," vol. 27, no. 2, pp. 376-390, 2008.

3. B. Arnal, M. Pernot, M. Tanter," Monitoring of thermal therapy based on shear modulus changes: II. Shear wave imaging of thermal lesions," IEEE T Ultrason Ferr, vol. 58, no. 8, pp. 1603-1611, 2011.

4. E. Sapin-de Brosses, J.L. Gennisson, M. Pernot, M. Fink, M. Tanter, "Temperature dependence of the shear modulus of soft tissues assessed by ultrasound," Phys Med Biol, vol. 55, no. 6, pp. 1701, 2010.

5. A. Sarvazyan, O. Rudenko, S. Swanson, J. Fowlkes, S. Emelianov. Shear Wave Elasticity Imaging: A New Ultrasonic Technology of Medical Diagnostics. Ultrasound Med Biol. 1998; 24(9):1419–1435.

6. M. Fatemi, J. Greenleaf. Ultrasound-Stimulated Vibro Acoustic Spectrography. Science. 1998; 280:82–85.

7. K.R. Nightingale, M.S. Soo, R.W. Nightingale, G.E. Trahey. Acoustic Radiation Force Impulse Imaging: In vivo Demonstration of Clinical Feasibility. Ultrasound Med Biol. 2002; 28(2):227–235.

8. J Bercoff, M. Tanter, M. Fink. Supersonic shear imaging: a new technique for soft tissue elasticity mapping. IEEE Trans Ultrason, Ferroelec, Freq Contr. 2004; 51(4):396–409.

9. F. Viola, W.F. Walker. Radiation force imaging of viscoelastic properties with reduced artifacts. IEEE Trans Ultrason Ferroelectr Freq Control. 2003 Jun; 50(6):736–742.

10. F.L. Lizzi, R. Muratore, C. Deng, J. Ketterling, K. Alam, S. Mikaelian, et al. Radiation-Force Technique to Monitor Lesions During Ultrasonic Therapy. Ultrasound Med Biol. 2003; 29(11):1593–1605.

11. E. Konofagou, J. Thierman, K. Hynynen. A focused ultrasound method for simultaneous diagnostic and therapeutic applications–a simulation study. Phys Med Biol. 2001 Nov; 46(11):2967–2984.

12. M. Fink, M. Tanter. A multiwave imaging approach for elastography. Current Med Imaging Rev. 2011 Elasticity Imaging Hot Topic Issue.

13. E. Konofagou, C. Maleke. Harmonic Motion Imaging (HMI) for tumor imaging and treatment monitoring A review. Current Med Imaging Rev. 2011 Elasticity Imaging Hot Topic Issue.

14. M. Urban, S. Chen, M. Fatemi. A review of Shearwave Dispersion Ultrasound Vibrometry (SDUV) and its applications. Current Med Imaging Rev. 2011 Elasticity Imaging Hot Topic Issue.

15. K. Parker. Ultrasonic Attenuation and Absorption in Liver Tissue. Ultrasound Med Biol. 1983; 9(4):363–369.

16. W.L.M. Nyborg. Acoustic Streaming. In: Mason, WP., editor. Physical Acoustics. Vol. vol. IIB. New York: Academic Press Inc; 1965. p. 265-331.

17. K. Nightingale, R. Bentley, G.E. Trahey. Observations of Tissue Response to Acoustic Radiation Force: Opportunities for Imaging. Ultrasonic Imaging. 2002; 24:100–108.

Chapter VII

Conclusions

In this research project, it has been investigated first the role of invasive technique based on fiber Bragg grating sensors for temperature monitoring in *ex vivo* and *in vivo* biological tissues.

Based on this technology, different models have been developed to predict temperature distribution and damaged volume around antenna during MWA and around optic fiber during LTA performed on *ex vivo* biological tissues.

Furthermore, a needle-like probe based on FBGs array has been designed and tested in *in vivo* animal model undergoing RFA. This measurement system allows monitoring, in real time, the tissue temperature at three different locations from the RFA electrode, in order to obtain information about the temperature distribution, as sensors are placed in correspondence of different isothermal lines.

Concerning non-invasive imaging based thermometry on *ex vivo* biological tissues during ablation procedures, CT, MR and US have been investigated. This approach entails strict requirements in order to be clinically feasible, among others: spatial resolution of 1-2 mm, acquisition time shorter than 10-30 s; and temperature accuracy of 1-2 °C.

According to the results provided, imaging based thermometry seems to be a safe and feasible biomedical methodology which could significantly improve the actual

ablation settings and furthermore could lead extend the boundaries of percutanous ablation to treat a wider spectrum of malignant lesions sparing healthy tissues.

The results obtained have demonstrated that all these imaging techniques can be adopted for temperature monitoring, each with peculiar pros and cons.

CT, which is the most studied radiological technique, offers good levels of thermal-spatial detail but it entails X-rays exposition and shows high sensitivity to motion; because of this, even if multiple *ex vivo* studies have reported encouraging results, for ethical reasons *in vivo* are lacking.

Radiation free imaging techniques involve MR and US.

The first presents high thermal sensitivity, low sensitivity to motion and good linearity; T1-weighted sequences especially have demonstrated to be practically adoptable on MWA and LTA. Actually, because of magnetic artifacts, MR thermometry can be performed only with amagnetic devices and this exclude RFA and entails higher costs. However, nowadays MR thermometry remains the more adopted imaging based thermometry technique.

Among US, focusing on elastography and ARFI, this approach seems to be the solution to tackle some issues related to the use of MR and CT thermometry, such as the use of expensive and MR-compatible tools and the X-ray dose to the patients, respectively. Main drawbacks are motion artifacts and low sensitivity up to 55-60°C.

In the future, experimental sessions on humans have to be encouraged, especially using US and MR, in order evaluate the concrete value of this techniques and assess the deriving improvements in the oncological healthcare.